

Abstract

Title of Dissertation: Three-Body Capture of Jupiter's Irregular Satellites
and Resonant History of the Galilean Satellites

Catherine M. Philpott, Doctor of Philosophy, 2010

Dissertation directed by: Professor Douglas P. Hamilton
Department of Astronomy

We examine the capture of small, irregular satellites, which, with their distant, eccentric, and inclined paths, must have originated in heliocentric orbits. We investigate a new theory: capture of one member of a pair of ~ 100 -km asteroids after tidal disruption. The energy loss from disruption is sufficient for capture, but it cannot deliver the bodies directly to the currently observed orbits. Instead, the long-lived capture orbits must evolve inward after capture, perhaps due to interactions with a tenuous circumplanetary gas disk.

We find that at Jupiter, binaries offer an increase of a factor of ~ 10 in the capture rate of 100-km objects as compared to single bodies, for objects separated by tens of radii that approach the planet on relatively low-energy trajectories. These bodies are at risk of collision with Callisto, but may be preserved by gas drag if their pericenters are raised quickly enough. We conclude that our mechanism is as capable of producing large irregular satellites as previous suggestions, and it avoids several problems faced by alternative models.

To investigate possible source populations for these captured satellites, we simulated escaping asteroids from Jupiter's Trojan region and the outer main belt, calculating the Jacobi constant during close approaches and comparing with three-body capture statistics. We found that Trojans' high approach speeds make them

unlikely source bodies, but asteroids from the outer main belt, especially those interior to Jupiter's 4:3 resonance, approach with low speeds that favor capture.

Unlike irregular satellites, regular satellites formed with their planets. Gravitational resonances are important for these bodies, and we study the most famous of them. Io, Europa, and Ganymede are in the Laplace resonance, meaning that they have orbital periods in the ratio of 1:2:4. We focused our work on Io and Europa's orbital lock and modeled passage through the 2:1 resonances. We discovered cases where damping from satellite tides led to stable equilibria prior to capturing into the resonances. The mean-motion ratio at which this occurs matches that of Io and Europa. We conclude that the moons never captured into resonance, and that their resonant angles librate because of long-range resonant forcing.

Three-Body Capture of Jupiter's Irregular Satellites and Resonant History of the Galilean Satellites

by

Catherine M. Philpott

Dissertation submitted to the Faculty of the Graduate School of the
University of Maryland at College Park in partial fulfillment
of the requirements for the degree of
Doctor of Philosophy
2010

Advisory Committee:

Professor Douglas P. Hamilton, chair

Professor Craig B. Agnor

Professor Michael F. A'Hearn

Professor M. Coleman Miller

Professor Derek C. Richardson

Professor James A. Yorke

© Catherine M. Philpott 2010

Preface

This dissertation is divided into two main parts. Chapters 1- 3 are focused on determining the capture mechanism and source population of the irregular satellites at Jupiter. We begin with an introduction to the irregular satellites, after which we detail our capture model, and finally, in Chapter 3, we explore various source populations for captured bodies. Part of this study is currently in press in *Icarus*, entitled “Three-body capture of irregular satellites: Application to Jupiter” and authored by myself, Douglas P. Hamilton, and Craig B. Agnor. Chapter 3 is an extension of my second-year research project at the University of Maryland.

In the second section, we study the orbital evolution of Jupiter’s Galilean satellites; in particular, that of Io and Europa. Chapter 4 gives background on the Galilean satellites and orbital dynamics, and in Chapter 5, we discuss our exploration of the origin of the Laplace resonance. Finally, we offer our conclusions and some future directions.

Katie Philpott

June 15, 2010

To Justin.

Acknowledgements

Above all, I am eternally grateful to God for all things, including leading me to Maryland and giving me the strength and perseverance to succeed in graduate school. As astronomers, we strive to uncover the incredible mysteries of the universe He created, and I believe these endeavors please Him.

I am also grateful for all the wonderful people who have helped me in so many ways over these past seven years. First, many thanks to my amazing advisor, Doug Hamilton, for his ever-present guidance, wisdom (in science and in life), and mentorship. Besides being a stellar advisor, Doug is also a delightful person. I will miss our meetings over tea, each peppered with humorous, non-research-related tangents.

Thanks are also owed to my thesis committee. I was very lucky to have also had Mike A'Hearn as an advisor here at UMD; I learned so much from him and am thankful for his support throughout this process. I am also extremely appreciative of Cole Miller and Derek Richardson,

for their research advice as well as their friendship. In addition, I have greatly enjoyed working with Craig Agnor, and I am thankful for his insightfulness and good humor. Finally, thank you to Jim Yorke for serving as Dean's Representative on my committee; I appreciated his desire to learn more about my research.

My career aspirations are centered on my love of teaching, which was well-nourished by Grace Deming, Cole Miller, and Melissa Hayes-Gehrke. Thank you to each of them for their mentoring and advice as well as for being examples of excellent teachers.

My classmates here have made this experience infinitely more enjoyable. Our incoming class of 2003 consisted of Ashley Zauderer, Elyse Casper (now Rhodin), Lisa Winter, Dara Zeehandelaar, Alan Gersch, Meredith McCarthy, Marcus Woo, and myself. We became fast friends, both in the department and out. I have great memories of our time together, whether it was struggling through homework or, much more fun, our various outings and parties. I recall several great birthday dinners, including an accidental trip to Waldorf (instead of Rockville). When it was my turn, I was (gently) kidnapped and taken to Uno's for a slice of home. We also enjoyed exploring DC together. I am grateful to these classmates and wish them the best in the future.

One of the best things about UMD is that nice, friendly people are not an anomaly. I am thankful to all of the other graduate students for their camaraderie and friendship (including but by no means limited to the above classmates, Stacy Teng, Matthew Knight, Vanessa Lauburg, Megan DeCesar, Lisa Wei, Mia Bovill, and Shaye Storm), the post-docs and researchers (especially Chul Gwon), all of the professors, and the

computer and office staff. The pleasant, supportive environment here is unique and very special.

A few of the above people deserve extra-special mention. Except for a few days, Ashley was my officemate for the entirety of graduate school. She has been a source of constant support and encouragement as well as one of my closest friends. On good days and bad, Ashley and I have celebrated successes and commiserated about difficulties. I will remember with fondness our many breakfasts at the Barnside Diner, Catholic Student Center dinners (with Elyse and Lisa!), running at Lake Artemesia, yoga/pilates classes (with Mia!), crêpe making, and all of our other shenanigans. I am greatly indebted to Ashley for her friendship.

Two other dear friends, Elyse and Lisa, were also my roommates for the beginning of grad school. It was great to have them there in those early years for studying as well as having fun, and we have stayed close since moving apart. While roommates, we survived a few hurricanes (including one during our first week in Maryland) and pursued perhaps the most valuable research study of our grad school years: the famous toast vs. ice cream conundrum. While Elyse, Lisa, and I made it through hurricanes, my later roommates, Sarah Gerson and Christine Forbes, and I survived an apartment fire! Many thanks to Lisa, Elyse, Sarah, and Christine for being delightful people and good friends.

A short but special thanks to friends from my extra-curricular outlets, Meals on Wheels and the National Philharmonic Chorale. These people (and organizations) made for refreshing, enjoyable changes of pace from the day-to-day grad school grind.

I also cannot forget my (almost) lifelong friends from the Downers Grove area, very descriptively known as “The Group.” I am grateful to them for their familiar, ever-present friendship.

Finally, thank you to my amazing family. I am especially grateful to my parents for giving me the confidence and support to pursue my aspirations. They have encouraged me to do my best since I was a child, and they have given me the most important education of all with their life lessons and their love. Thank you also to my fabulous brother and sister, John and Liz. I love that we’ve grown up to be not just siblings, but great friends. I am also thankful to my new(er) family: Rita and Mickey, Stacey and Matt, and Jess, Brent, and Jack. One could not ask for better in-laws.

Last but most certainly not least, thank you to my incredible husband, Justin, for his neverending love and encouragement. He has been so patient and supportive, providing both an interested ear when I wanted to talk science and a respite from all-things-research when I didn’t. I am extremely lucky to have him by my side throughout this and every other experience life brings us.

Contents

List of Tables	x
List of Figures	xi
1 Irregular Satellites: Introduction	1
1.1 Definition and discovery	1
1.2 Orbital and physical properties	5
1.3 Theories of origin	13
2 Three-Body Capture of Irregular Satellites	17
2.1 Capture from 100-km binaries	17
2.2 Three-body capture process	20
2.3 Numerical model	28
2.4 Relationship between inclination and C_J	31
2.5 Modes of capture	35
2.6 Effects of binary mass and orbital separation	37
2.7 Effects of starting distance	41
2.7.1 Contamination from bound retrograde orbits	41
2.7.2 Scaling to different starting distances	42
2.7.3 Starting from 1.1 r_H vs. 1.0 r_H	46
2.8 Scaling to unequal binary masses	48
2.9 Jupiter's eccentricity	50
2.10 Survivability of captured objects	51
2.11 Discussion and conclusions	57
3 Assessing Asteroids as Potential Satellite Sources	60
3.1 Introduction	60
3.2 Numerical methods	66
3.3 Trojans with an eccentric Jupiter	69
3.4 Trojans with a non-eccentric Jupiter	74
3.5 Escape from the outer asteroid belt	77
3.6 Conclusions	82

4 Galilean Satellites: Background	85
4.1 Physical properties	85
4.2 Orbital properties and resonances	89
5 Resonant History of the Galilean Satellites	98
5.1 Orbital evolution models	98
5.2 Numerical model	100
5.3 Simulations of Io and Europa	101
5.4 Findings and future directions	119
6 Conclusions	120
6.1 Irregular satellites	120
6.2 Galilean satellites	122
Bibliography	123

List of Tables

1.1	Satellite counts per planet	5
1.2	Giant planet Hill spheres	6
2.1	Mass ratio tests for binaries with $C_J=3.03$	49
3.1	Integration parameter tests for Trojan asteroids	68
3.2	Jacobi constants of escaped Trojan asteroids	76
4.1	Galilean satellites: physical data	86
4.2	Galilean satellites: orbital data	90
5.1	Integrations of Io and Europa's 2:1 resonance passage: non-zero initial inclinations	108

List of Figures

1.1	Number of known irregular satellites	4
1.2	Semi-major axis vs. inclination	7
1.3	Semi-major axis vs. eccentricity	8
1.4	Semi-major axis, eccentricity, and inclination	10
2.1	Speeds of unequal-mass binary components	21
2.2	Jupiter’s Hill sphere	24
2.3	Example capture: Jacobi constant	25
2.4	Example capture: orbit	27
2.5	Inclination vs. Jacobi constant	32
2.6	Modes of capture vs. separation	36
2.7	Capture percentage vs. C_J for various masses	39
2.8	Capture percentages for two launch distances	43
2.9	Scaling of capture rates from two starting distances	45
2.10	Modes of capture vs. Jacobi constant	47
2.11	Percent of captures not crossing Callisto’s orbit	52
2.12	Gas drag applied to captures	55
3.1	Trojan and Hilda asteroids	61
3.2	Trojan swarms	63
3.3	Example Trojan escape	65
3.4	Trojan close-approach distances vs. initial inclination	70
3.5	Approach geometry for three-dimensional simulations	73
3.6	Jacobi constants of escaped Trojans	75
3.7	Initial semi-major axes of escaped outer-main belt asteroids	79
3.8	C_J and v_{L_1} for escapes from the outer asteroid belt	80
3.9	Distribution of close-approach distances for outer main belt asteroids	83
4.1	Galileo spacecraft images of the Galilean satellites	87
4.2	Resonant splitting	95
5.1	Capture into the i_2^2 resonance	103
5.2	Trapping into the i_1^2 resonance	106

5.3	Third-order 2:1 resonances between Io and Europa	107
5.4	Capture into $e_2 i_2 i_1$ and $i_1 i_2$	109
5.5	Io and Europa, no satellite tides	113
5.6	Io and Europa, weak satellite tides	114
5.7	Io and Europa, stronger satellite tides	116
5.8	Resonant angles for Io and Europa, stronger satellite tides	117

Chapter 1

Irregular Satellites: Introduction

1.1 Definition and discovery

With discoveries accelerating in the last decade, we now know of over 150 satellites orbiting the giant planets. About one-third of these are classified as regular, with nearly circular and planar orbits. It is thought that these satellites are formed by accretion in circumplanetary disks. The majority of the satellites, however, are irregular and follow very different paths from their regular counterparts. It is widely believed that irregular satellites originated in heliocentric orbits and were later captured by their planets, but the details of how this occurred are still uncertain. This question is a main focus of this thesis. In Section 1.3, we discuss possible capture theories, and in Chapter 2, we describe our capture model involving three-body interactions between a planet and small binary pairs.

One important reason to study the irregular satellites is because they probe conditions of the Solar System at early times. Capturing the irregular satellites from heliocentric orbit requires energy loss from a dissipative process such as dynamical friction from gas or other bodies. Currently, the Solar System has no such process that could remove enough energy for capture to their present orbits. Thus, the

irregular satellites must have been captured before the Solar System settled into its current state; for example, during planet formation and/or migration, when numerous small bodies still roamed the Solar System. As the orbits of irregular satellites were shaped by one or more of these processes, they provide insight into the early Solar System environment.

Before proceeding, we discuss the common qualities of irregular satellites, defined as moons that were captured from heliocentric orbit to their current locations around the planet. Irregular satellites usually have orbits that are distant, highly eccentric, and significantly inclined. From observations, we see that the giant planets' irregular satellites generally orbit far enough from their host planet that solar perturbations (and not planetary oblateness) dominate long-term dynamics. Setting the precession from oblateness equal to the precession due to solar tides, we calculate the distance (r_{tr}) at which orbits' precession transitions from being dominated by oblateness to dominated by solar tides:

$$r_{tr} = \left(2J_2 \frac{M_P}{M_S} R_P^2 a_P^3 \right)^{1/5}, \quad (1.1)$$

where M_P and R_P are the mass and radius of the planet, M_S is the mass of the Sun, J_2 is the planet's oblateness coefficient, and a_P is the mean planet-Sun distance (Burns 1986a). The distance, r_{tr} , is 2.3, 2.5, 1.4, and 1.8 million km for Jupiter, Saturn, Uranus, and Neptune, respectively. In reality, it is somewhat larger, as the planets' large, regular satellites effectively add to J_2 for more-distant bodies (Ćuk 2005). This measure by itself, however, is still not enough to differentiate between irregular and regular moons. Neptune's Triton has a semi-major axis smaller than r_{tr} even though its retrograde orbit points toward an origin by capture. However, Triton is believed to have been pulled close to Neptune by tidal forces. We can use r_{tr} as a general criterion for satellite classification and add to it our intuition about

which satellites were likely captured.

Two great advances in observational technology were instrumental in the discoveries of the irregular satellites. The first was the use of photographic plates, which began in the late 1800s. Long-exposure photographic plates allowed observers to see faint objects, and in 1898, this resulted in the discovery of Phoebe, the ninth known satellite of Saturn. Phoebe was seen orbiting the planet in the opposite direction of Saturn's eight other known satellites and at a much larger semi-major axis. A few years later, in 1904, Himalia was discovered on a large, prograde orbit at Jupiter. In the decades that followed, seven more irregular satellites (three more prograde, four retrograde) were discovered at Jupiter, and Nereid was found on a highly eccentric orbit at Neptune. The last satellite found with photographic plates, Jupiter's Leda, was discovered in 1974.

The advent of sophisticated, wide-field CCDs in the late 20th century led to a flood of irregular satellite discoveries. After almost a quarter-century drought in discoveries, Gladman *et al.* (1998) found two new irregular satellites at Uranus while looking for Kuiper Belt objects. In 1999, Gladman's team found three more Uranians (Gladman *et al.* 2000) and the Spacewatch team found one new irregular moon at Jupiter (Scotti *et al.* 2000). In 2000, the discoveries accelerated, with 11 new satellites found at Jupiter (Sheppard and Jewitt 2003) and 12 at Saturn (Gladman *et al.* 2001). In total since 1997, 47 Jovians, 37 Saturnians, 9 Uranians, and 5 Neptunians have been found (Gladman *et al.* 2000, 2001, 1998; Holman *et al.* 2004; Kavelaars *et al.* 2004; Scotti *et al.* 2000; Sheppard *et al.* 2005, 2006; Sheppard and Jewitt 2003; Sheppard *et al.* 2007). As of June 2010, there are 109 known irregular satellites. Figure 1.1 shows the growing number of known irregulars since the beginning of the 20th century.

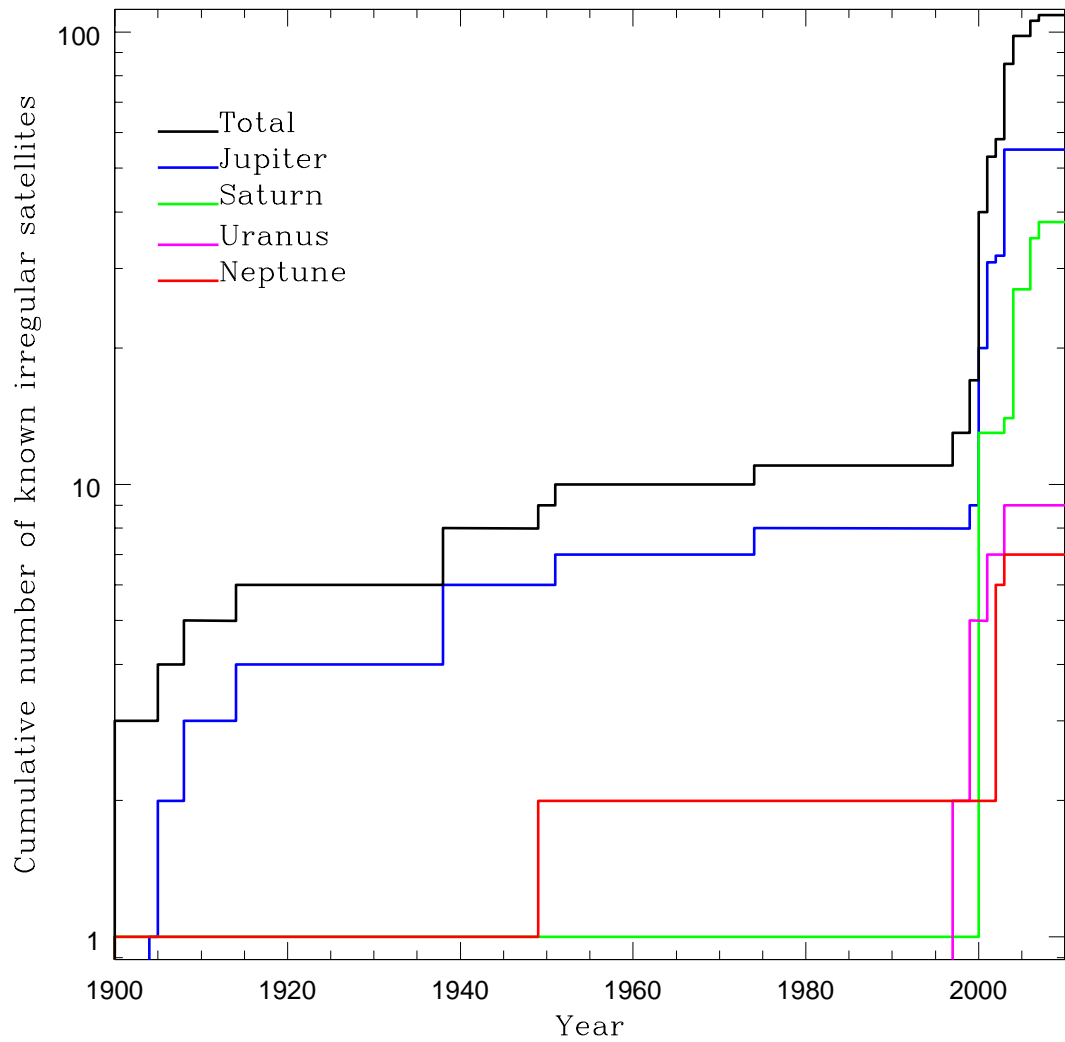


Figure 1.1 The cumulative number of known irregular satellites of the giant planets, with the total irregular satellite count represented by the black line. The spike just prior to the year 2000 represents the transition from the photographic era to the use of wide-field CCDs.

Table 1.1. Satellite counts per planet

Planet	N_{tot}	N_{reg}	N_{irreg}	$N_{i,pro}$	$N_{i,retr}$
Jupiter	63	8	55	7	48
Saturn	62	24	38	9	29
Uranus	27	18	9	1	8
Neptune	13	6	7	3	4
Total	165	56	109	20	89

Note. — Satellite counts per planet: the total number of satellites (N_{tot}) and the numbers of regular satellites (N_{reg}), irregular satellites (N_{irreg}), prograde irregular satellites ($N_{i,pro}$), and retrograde irregular satellites ($N_{i,retr}$).

1.2 Orbital and physical properties

Table 1.1 gives the current number of regular and irregular satellites per planet, dividing the irregular satellites into those on prograde (with inclination $i < 90^\circ$) and retrograde ($i > 90^\circ$) orbits. While many more satellites have been discovered around Jupiter and Saturn than Uranus and Neptune, the number differences are primarily a result of observational bias. In fact, it is estimated that the satellite counts at the four giant planets are roughly equal (Jewitt and Sheppard 2005). A simple way to demonstrate this is to count the number of satellites at each planet larger than the minimum detectable size at Neptune (~ 15 km in radius); the result is that the four planets each have ~ 5 satellites at this size or larger. One interesting fact from this table is that the number of known irregular retrograde satellites outnumbers the number of known irregular progrades at every planet. In all, the ratio of retrogrades to progrades is $89/20 \approx 4.5$. The reason for this lopsidedness is unknown; possibilities include differences in capture efficiency, collision rate, or long-term stability.

Table 1.2. Giant planet Hill spheres

Planet	M_P (10^{25} kg)	a_P (AU)	r_H (AU)	Angular size of r_H (deg)	N_{irreg}
Jupiter	190	5.2	0.36	4.8	55
Saturn	57	9.5	0.44	3.0	38
Uranus	8.7	19.2	0.47	1.5	9
Neptune	10.2	30.1	0.78	1.5	7

Note. — Characteristics of giant planets and their Hill spheres: mass (M_P), semi-major axis (a_P), Hill radius (r_H) in AU, projected angular r_H as seen from Earth at opposition, and number of irregular satellites (N_{irreg}).

Table 1.2 gives the characteristics of the Hill spheres of the giant planets. The radius of the Hill sphere (r_H) is the distance at which the Sun’s tidal acceleration roughly balances the planet’s gravity, and is given by

$$r_H = \left(\frac{M_P}{3M_S} \right)^{1/3} a_P. \quad (1.2)$$

While all of the actual satellites orbit within their planet’s Hill sphere, not all orbits within the Hill sphere are stable. In general, prograde orbits are stable out to about half the Hill radius, and retrograde orbits are stable to slightly beyond the Hill radius (Hamilton and Burns 1991). A simple way to understand this prograde/retrograde asymmetry is that the Coriolis force in the rotating reference frame points in toward the planet for retrograde orbits, giving an additional source of stability and allowing for larger orbits. Figure 1.2, a plot of the satellites’ mean semi-major axes and inclinations, shows that the actual satellites orbit well within their stability boundaries: progrades are found out to about a third of the Hill radius, and retrogrades orbit no further than half the Hill radius, with the exception of S/2003 J2.

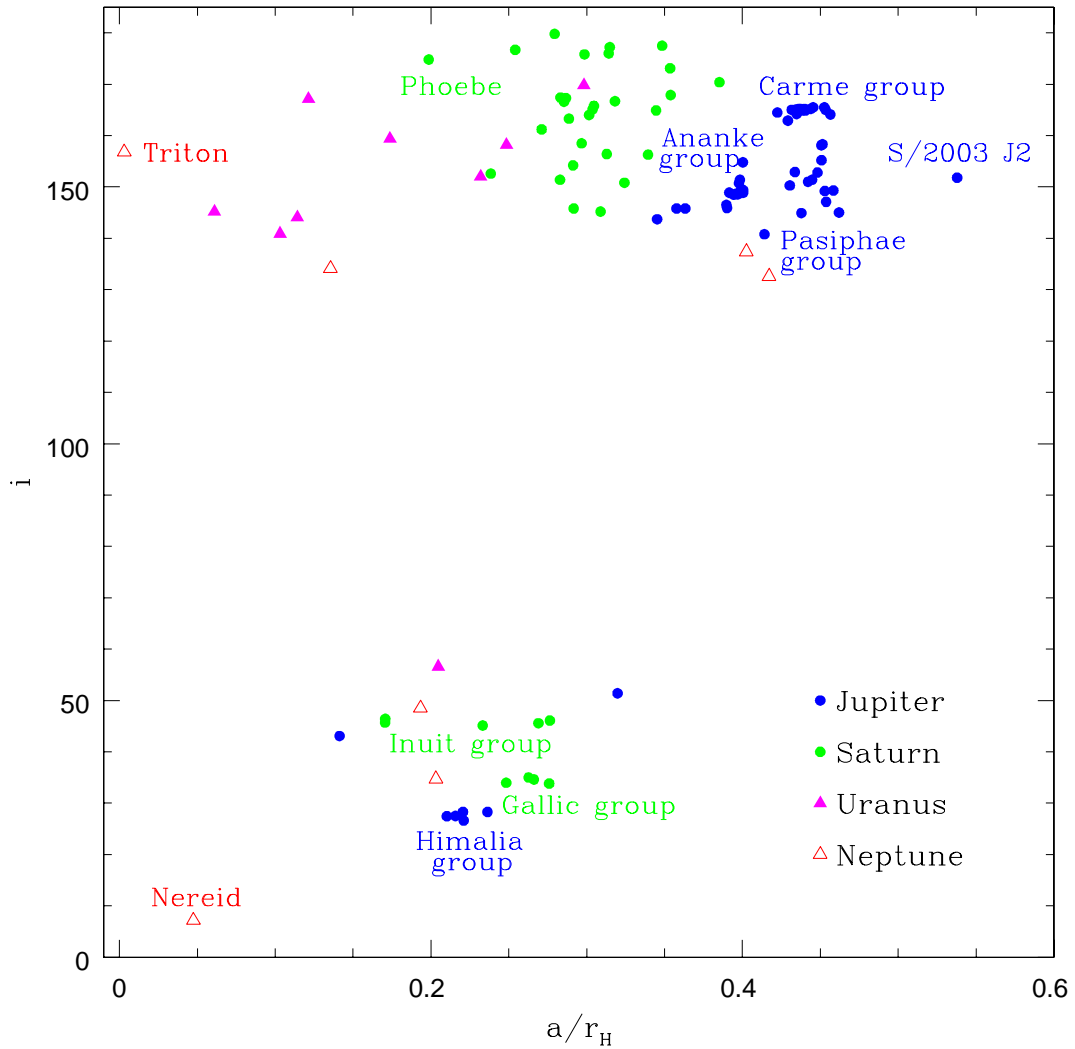


Figure 1.2 Semi-major axis scaled by the Hill radius vs. inclination for the known irregular satellites. Mean orbital elements for this figure and Figs. 1.3 and 1.4 are taken from S. Sheppard's irregular satellite website, <http://www.dtm.ciw.edu/users/sheppard/satellites/> and the JPL Solar System Dynamics website, http://ssd.jpl.nasa.gov/?sat_elem.

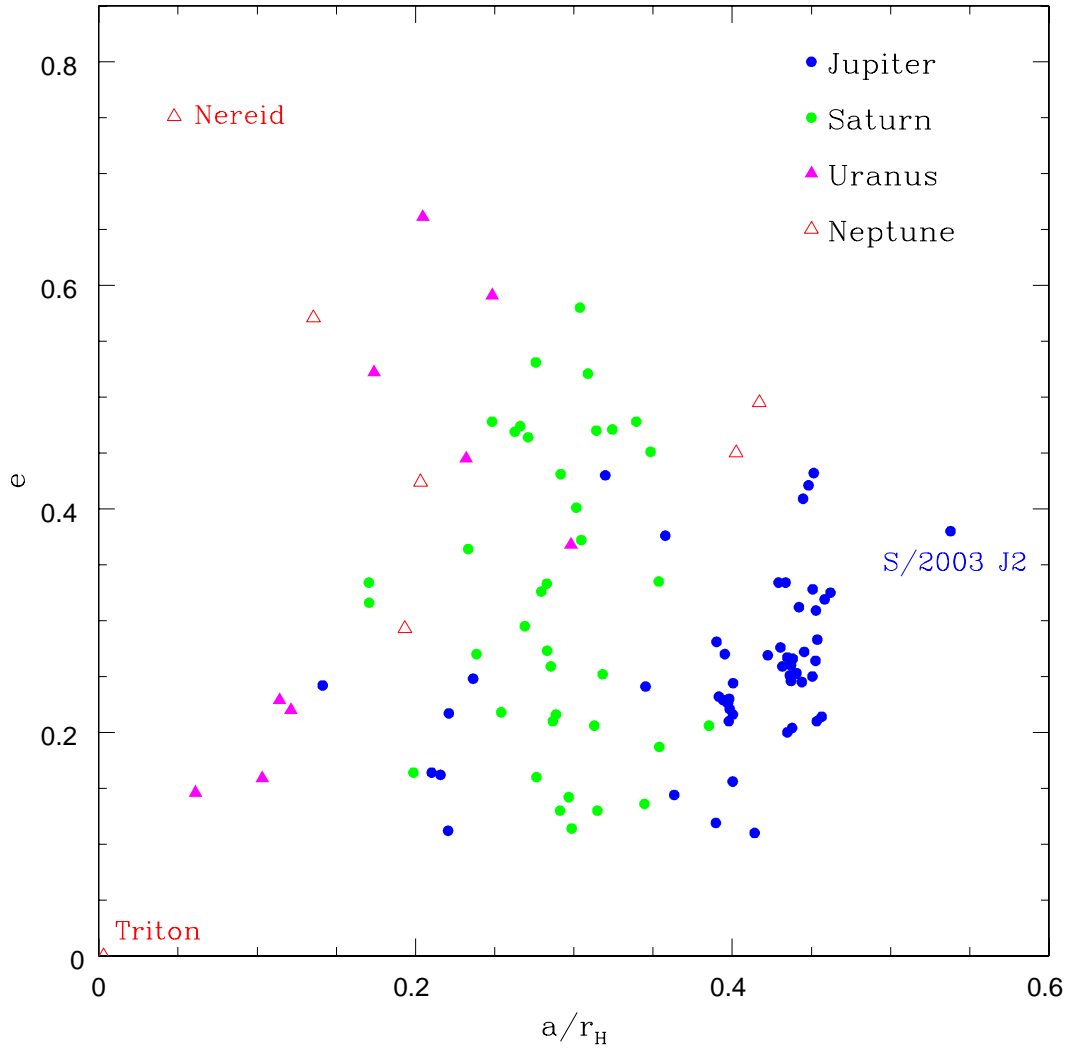


Figure 1.3 Semi-major axis scaled by the Hill radius vs. eccentricity for the known irregular satellites.

Another striking feature in Fig. 1.2 is the lack of satellites from $i = 60-130^\circ$. This is not due to limitations of surveys but instead is because of the Kozai effect. The Kozai effect causes eccentricity and inclination to oscillate, conserving the dimensionless $K = \sqrt{1 - e^2} \cos(i)$. Satellites with inclinations in this range eventually cycle to high eccentricities and subsequently collide with the planet or its regular satellites.

Figure 1.3 gives the distribution in semi-major axis/eccentricity space. From Figs. 1.2 and 1.3, we see that the semi-major axes of irregular satellites (measured in r_H) generally decrease for planets further from the Sun. The median semi-major axes (in r_H) are 0.43, 0.29, 0.17, and 0.19 for Jupiter, Saturn, Uranus, and Neptune, respectively. However, measured in kilometers, the trend disappears and the median a values are almost identical: 2.3×10^7 (Jupiter), 1.9×10^7 (Saturn), 1.2×10^7 (Uranus), and 2.2×10^7 (Neptune). The exception is at Uranus, where the irregular satellites orbit closer to the planet on average.

Figure 1.4 shows the semi-major axes, eccentricities, and inclinations of the irregular satellites all at once (Gladman *et al.* 2001). The distance from the origin to a point gives the satellite's semi-major axis, the angle from the positive x-axis gives the inclination, and the radial extent (distance from pericenter to apocenter) is displayed as the length of the line through the point. From this figure, we can see that not only do the retrograde satellites have larger semi-major axes than progrades, but they also have systematically larger eccentricities. This again can be traced to the increased stability of retrograde orbits over prograde orbits.

Figures 1.2, 1.3, and 1.4 all show groupings of satellites with similar orbital elements. These clusters are most apparent in Fig. 1.2, and several are labeled on this plot. Satellite families are thought to arise from collisional disruption of a single progenitor satellite (Burns 1986b; Colombo and Franklin 1971; Gladman *et al.* 2001; Pollack *et al.* 1979). We now briefly discuss the clusters existing at each planet. We will also summarize the naming conventions for the satellites (referencing Nicholson *et al.* (2008)), both because these are often dictated by the satellite orbits as well as for general interest.

At Jupiter, prior to 1997, it was thought that the eight known irregular satellites split evenly into two families: one tightly clustered prograde group (with Himalia

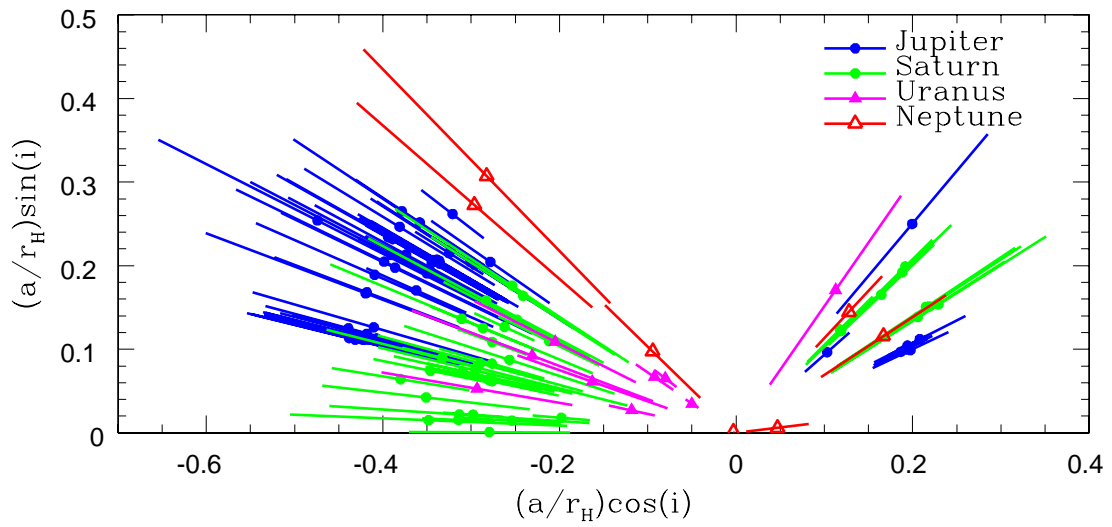


Figure 1.4 Semi-major axis, eccentricity, and inclination for the known irregular satellites. The distance from the origin gives the semi-major axis, the angle from the positive x-axis gives the inclination, and the length of the line through each point shows the radial extent (and thus eccentricity) of the satellites.

as its dominant member) and one more-loosely clustered retrograde group (consisting of Pasiphae, Carme, Ananke, and Sinope). As more satellites were discovered, the prograde group gained an additional member (S/2000 J11, which has not been recovered since discovery and is considered lost). For the retrograde satellites, however, three new groupings have been proposed (Nesvorný *et al.* 2003; Sheppard and Jewitt 2003), with three of the pre-1997 retrograde satellites as principal members: the Carme group, the Ananke group, and the more diffuse Pasiphae group (with Sinope a member of the Pasiphae group). Additionally, Themisto and Carpo, both prograde satellites, appear to be isolated. Jupiter’s irregular satellites are named for characters in Roman or Greek mythology that have connections to Jupiter (the Roman name for Zeus). The prograde satellites in the Himalia group have names ending in ‘a,’ and the progrades with higher inclinations have names that end in ‘o.’ Retrograde satellites have names ending in ‘e.’

Saturn’s prograde satellites are divided into two relatively tight groups; four with $i \approx 34^\circ$ (named after giants from Gallic mythology) and five with $i \approx 46^\circ$ (with names from Inuit mythology). The three retrograde groups each have similar inclinations (about 153° , 168° , or 175°), but vary widely in a and e . All of the retrogrades, except for Phoebe, are named after giants from Norse mythology.

With only nine irregular satellites at Uranus and seven at Neptune, it is more difficult to observe clear clusters. Uranus has only one prograde irregular satellite, so no prograde groupings are possible. Within the eight Uranian retrogrades, there are loose families centered on both Sycorax and Caliban; Kavelaars *et al.* (2004) and Sheppard *et al.* (2005) concluded that the clusters are statistically similar in semi-major axis and eccentricity but not inclination. The Uranian moons are all named after Shakespearean characters, irrespective of their orbits. Neptune’s single grouping is comprised of three of the four retrograde satellites (all but Triton), which

have inclinations near 135° . The Neptunian irregular satellites other than Triton and Nereid are named for Nereids, sea nymphs in Greek mythology. Progrades have names ending in ‘a’ or ‘o’ and retrogrades end in ‘e’ or ‘o.’ As more irregular satellites are discovered at the ice giants, their families will likely become more distinct and numerous.

The colors of the irregular satellites fall between neutral (with spectra similar to the Sun’s) and moderately red (Grav and Bauer 2007; Grav *et al.* 2004, 2003; Luu 1991; Maris *et al.* 2001; Rettig *et al.* 2001; Tholen and Zellner 1984). Though colors are not identical among dynamically clustered satellites, Grav *et al.* (2003) noted that colors within families are generally more similar to each other than to colors of satellites in other groups. The colors as well as low albedos (~ 0.04 – 0.05) of the irregular satellites are similar to those of C-, P-, and D-type asteroids (Cruikshank 1977; Degewij *et al.* 1980), Trojan asteroids at Jupiter (Fernández *et al.* 2003; Fornasier *et al.* 2004) and Neptune (Sheppard and Trujillo 2006), and comet nuclei (Jewitt 2005, 2002). However, they are systematically bluer overall than Kuiper belt objects (KBOs) (Jewitt and Haghighipour 2007). Scattered-disk KBOs, though, are somewhat less red than cold, classical KBOs (Tegler and Romanishin 2000; Trujillo and Brown 2002) and not as different in color from the irregular satellites. Sheppard and Trujillo (2006) postulate that because of color similarities, the small-body populations that may have been trapped or captured into their current locations (including irregular satellites, Jovian and Neptunian Trojans, and dynamically-excited KBOs) originated from a similar place in the Solar System. If true, this conclusion might also imply that bodies comprising these populations were transported and trapped at the same time in Solar System history.

1.3 Theories of origin

At least eight different models have been proposed to explain the capture of the irregular satellites, involving dissipative forces, collisions, resonances, and three-body effects. Each model has its own strengths and weaknesses.

In one long-standing theory, planetesimals are slowed as they punch through the gas disk surrounding a young, growing planet (Pollack *et al.* 1979). For this mechanism to be efficient, the gas must be sufficiently dense to capture the planetesimals in one pass. This is problematic, however, because if the gas disk does not rarefy substantially in ~ 100 - 1000 years, the orbits of the new satellites will decay inward, leading to collisions with the planet or its regular satellites. Furthermore, the atmospheres of Uranus and Neptune have only a few Earth-masses of hydrogen and helium at present, so their gas disks could not have been as extensive or long-lived as those of Jupiter and Saturn. A likely outcome of this model, then, is that satellite capture should have been different at Jupiter and Saturn than at Uranus and Neptune; however, current observational estimates suggest roughly equal efficiencies (Jewitt and Sheppard 2005). With a model similar to that of Pollack *et al.* (1979), Čuk and Burns (2004a) found that Jupiter’s largest irregular satellite, Himalia, would evolve inward to its current orbit in $10^4 - 10^6$ years. This gas disk, however, may make capture difficult.

In another model, planetesimals are captured when the mass of the planet increases (Heppenheimer and Porco 1977; Vieira Neto *et al.* 2004). This mass growth causes the planet’s escape speed to increase, rendering a previously free planetesimal bound to the planet. For this method to be effective, the planet’s mass must increase substantially during the time that planetesimals linger near the planet, ~ 100 - 1000 years. However, in most planet formation models (e.g., Pollack *et al.* 1996), giant

planet growth is hypothesized to take place on timescales many orders of magnitude longer than required by this capture scenario. Furthermore, Uranus and Neptune’s gas deficiency implies that their growth was of very short duration. Thus, our current understanding of planetary formation makes this model improbable.

The observation that the four giant planets contain approximately the same number of irregular satellites (accounting for observational biases; Jewitt and Sheppard (2005)) has led to a renewal of interest in capture theories that do not depend strongly on the planet’s formation process. In one such scenario, a planetesimal collides with a current satellite or another planetesimal in the vicinity of the planet, resulting in its capture (Colombo and Franklin 1971). Though collisions were certainly more common in the early Solar System than they are today, if they resulted in enough energy loss to permit capture, they would likely also have catastrophically disrupted the bodies. Nevertheless, the fragments might then have become independent satellites.

Astakhov *et al.* (2003) studied low-energy orbits that linger near Jupiter and Saturn. While these bodies are not permanently captured, the authors found that some of them were stable for thousands of years, long enough to allow a weak dissipative force such as gas drag to complete the capture process. However, the overall percentage of temporary captures that do not escape is small, and many of these bodies are threatened by collision with the planets’ large outer regular satellites (e.g., Callisto and Titan).

Agnor and Hamilton (2006a) examined the capture of Triton from an exchange reaction between a binary pair and Neptune. Their motivation stemmed from the newly discovered abundance of binaries in small-body populations. Currently, it is estimated that binaries account for $\sim 30\%$ of Kuiper belt objects (KBOs) with inclinations $< 5^\circ$, $\sim 5\%$ of the rest of the KBOs (Noll *et al.* 2008), and $\sim 2\%$ of large

main belt asteroids (diameters > 20 km; this percentage increases for smaller objects; Merline *et al.* (2007)). In Agnor & Hamilton’s capture model, a binary is tidally disrupted and one of its members, Triton, is captured as a satellite. This process is most effective for large satellites like Triton, with radius 1350 km. However, the largest of the other irregular satellites are more than 10 times smaller than Triton: Himalia at Jupiter is ~ 85 km in radius, Saturn’s largest irregular, Phoebe, is ~ 110 km, Uranus’s Sycorax is ~ 80 km, and Neptune’s Halimede and Neso are only ~ 30 km each. Capturing these satellites via binary exchange reactions would be significantly more difficult unless they were originally satellites of a much more massive primary, as we will discuss further.

Another suggestion involves the possible instability in the orbits of the outer planets early in the Solar System (e.g., by a 2:1 resonance crossing between Jupiter and Saturn). Outlining the theory of the Nice model of Solar System evolution, Tsiganis *et al.* (2005) have shown that such an event could cause Uranus and Neptune to have many close approaches with each other and with Jupiter and Saturn. During these encounters, the influence of the massive interloping planet can cause planetesimals to be stabilized as satellites (Nesvorný *et al.* 2007). This method is promising but has an important disadvantage in that Jupiter sustains very few close encounters relative to the other planets. Thus Jupiter is inefficient at capturing satellites in this way (Nesvorný *et al.* 2007).

Vokrouhlický *et al.* (2008) examined binary exchange reactions during the first 100 Myr after a Jupiter/Saturn 2:1 resonance crossing, using results of the Nice model to guide their initial conditions. Because planetesimal speeds relative to the planets are high after the scattering phase of the Nice model, they found that captures from binaries during that time do not match current orbital parameters and occur too infrequently to account for today’s populations. They also offer the

model-independent conclusion that binary capture requires low encounter speeds to be efficient.

Finally, Gaspar *et al.* (2010) studied binary capture in the prograde planar case. They placed binaries on low-speed trajectories and examined the direction of capture. As expected, tidal disruption preferentially occurred when the two components were aligned with the planet. In addition, they found that permanent capture occurred most often when the binary was disrupted after it passed between the Sun and Jupiter in its orbit.

In the next chapter, we introduce our model for irregular satellite capture and discuss our numerical simulations thereof.

Chapter 2

Three-Body Capture of Irregular Satellites

2.1 Capture from 100-km binaries

All of the models outlined in Chapter 1 have promising aspects coupled with important limitations. In this work, we seek to combine the best features of several models into a viable capture scenario. In particular, we examine binaries (as in Agnor and Hamilton (2006a); Vokrouhlický *et al.* (2008); and Gaspar *et al.* (2010)) as a way to augment capture from low-speed orbits resulting from three-body interactions like those studied by Astakhov *et al.* (2003). While Vokrouhlický *et al.* (2008) studied exchange reactions in the context of an assumed initial planetesimal population, we focus on assessing the viability of the mechanism itself. Our goal is to determine how various parameters of the model affect its plausibility. We examine the process at Jupiter, as a number of the above models suggest that capturing at the largest gas giant is especially difficult.

As the largest of the existing irregular satellites are $\sim 80\text{--}110$ km in radius, cap-

ture of objects in this size range is particularly interesting. Since it is likely that the irregular satellite population contains collisional families (Nesvorný *et al.* 2003; Sheppard and Jewitt 2003), it may be the case that only the largest objects were captured, while the smaller satellites formed later, via collisions. For this reason, we focus our investigation on capturing the ~ 100 -km progenitors.

In order to stabilize and shrink the resulting capture orbits, a dissipation source is required; we suggest a tenuous version of the gas drag originally proposed by Pollack *et al.* (1979). Two of Jupiter’s irregular satellites, Pasiphae and Sinope, as well as Saturn’s satellites, Siarnaq and Narvi, and Uranus’ Stephano are found in resonances or near-resonances that may require just such a weak dissipative force (Beaugé and Nesvorný 2007; Čuk and Burns 2004b; Čuk *et al.* 2002; Nesvorný *et al.* 2003; Saha and Tremaine 1993; Whipple and Shelus 1993).

Furthermore, a tenuous circumplanetary disk is consistent with current theories of late-stage planetary formation. Jupiter’s massive gaseous envelope of hydrogen and helium necessitates that it formed in the Solar System’s circumstellar gas disk. Before the end of its accretion, Jupiter was likely able to open a gap in the local density distribution of the gas (for a review, see, e.g., Papaloizou *et al.* (2007)). After gap opening, gas continues to leak into the planet’s Hill sphere through the L_1 and L_2 points, but at a rate much reduced in comparison to the previous epochs. A tenuous circumplanetary gas disk results (e.g., Bate *et al.* 2003; D’Angelo *et al.* 2003; Lubow *et al.* 1999), from which material may condense and regular satellites may accrete near the planet (e.g., Canup and Ward 2002; Mosqueira and Estrada 2003).

In Čuk and Burns’ study (2004a) of the Himalia progenitor’s orbital evolution, they considered circumjovian nebular conditions consistent with hydrodynamical simulations of Jupiter’s gap opening in a circumstellar gas disk (e.g., Lubow *et al.*

1999) and found the post-capture timescale for evolving this progenitor from its initial location to its present orbit to be roughly in the range of $10^4 - 10^6$ years. This is similar to the timescale in which extrasolar circumstellar disks transition from optically thick to thin ($\sim 10^5$ years; Cieza *et al.* (2007); Silverstone *et al.* (2006); Skrutskie *et al.* (1990)). The similarity of timescales suggests that satellites captured at the onset of disk dispersal have a good chance of experiencing stabilizing orbital evolution while also avoiding collision with the planet.

The timescale for binary capture is very short compared to evolution timescales from a tenuous gas disk. Therefore, we focus our study first on characterizing the effectiveness of binary capture in the absence of gas. Further, we assume that irregular satellites captured during late-stage planetary formation are able to survive any post-formation planetary migration. This may not be the case if the host planet has close encounters with other planets (as in the Nice model; e.g., Tsiganis *et al.* (2005)). As evidence for planet-planet scattering is inconclusive, especially for Jupiter, we focus here on examining the binary capture mechanism apart from migration models.

In the following sections, we critically evaluate our model for capturing irregular satellites from low-mass (~ 100 -km) binaries. We begin with a closer examination of the three-body capture process and then explore parameter space with a large suite of numerical simulations. While the details of post-capture orbital evolution are not the focus of this work, we briefly discuss the ability of gas drag to stabilize orbits in Section 2.10.

2.2 Three-body capture process

Binary capture first requires a close approach between a binary pair and a planet. As the pair approaches the planet on a hyperbolic trajectory, its two components also orbit their mutual center of mass (CM). Hence, each member’s speed with respect to the planet is a vector sum of its CM speed (v_{CM}) and its orbital speed around the CM. If the binary passes close enough to the planet, it will be tidally disrupted. Following Agnor and Hamilton (2006a), we make an ‘impulse approximation’ and assume that disruption is instantaneous, so that the distance at which tidal disruption occurs (r_{td}) can be estimated as:

$$r_{td} \approx a_B \left(\frac{3M_P}{m_1 + m_2} \right)^{1/3}, \quad (2.1)$$

where a_B is the semi-major axis of the binary, M_P is the mass of the planet, and m_1 and m_2 are the masses of the binary pair. This tidal disruption radius is the distance to the planet at which the binary’s mutual Hill sphere r_H is no longer larger than the binary semi-major axis a_B .

As a result of the impulse approximation, we also assume that the orbits of the now-separated components are dictated by their speeds upon disruption. The maximum speed change of one component (Δv_1) is approximately equal to its orbital speed around the CM:

$$\Delta v_1 \approx \pm \frac{m_2}{m_1 + m_2} \left(\frac{G(m_1 + m_2)}{a_B} \right)^{1/2}, \quad (2.2)$$

where G is the gravitational constant. If the speed of either component (relative to the planet) is below the planet’s escape speed (v_{esc}) when the binary is split, that component will be captured. This is most efficient if the incoming v_{CM} is only slightly faster than the value needed for escape (see Fig. 2.1).

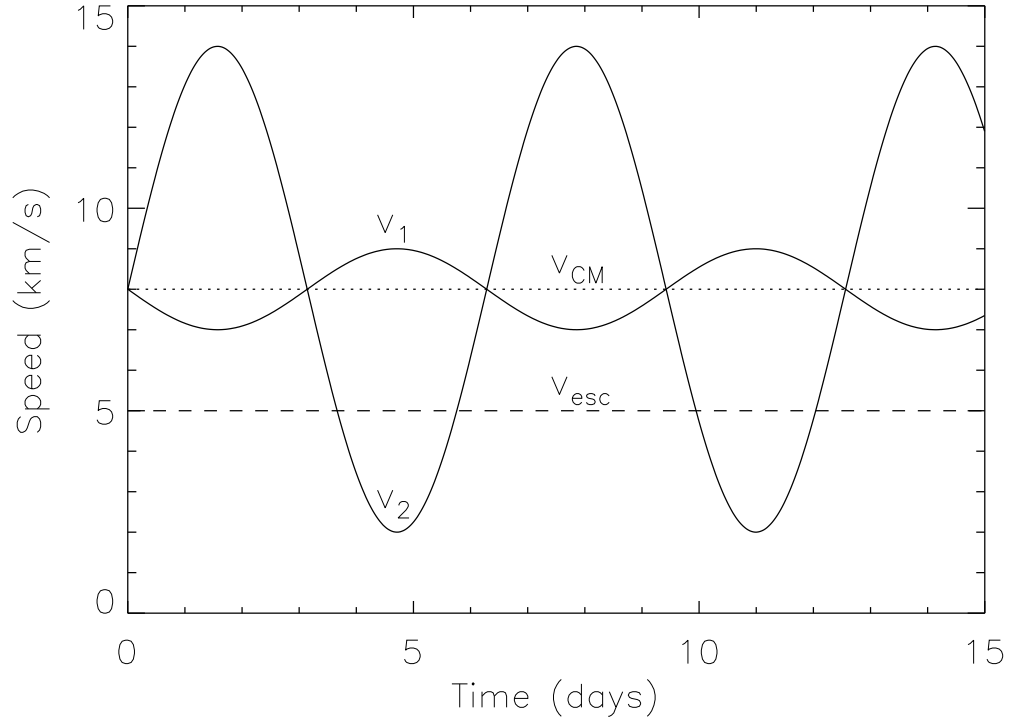


Figure 2.1 The speeds of unequal-mass binary components (v_1 and v_2) and the center-of-mass speed (v_{CM}) relative to Jupiter, where $m_1 > m_2$. Since the binary center of mass approaches the planet along a hyperbolic trajectory, it is always traveling faster than the local escape speed (v_{esc}). In this example, the smaller component's speed dips below the escape speed for a portion of its orbit. If the binary is disrupted during this interval, the smaller component will be captured by the planet. Though this is a purely illustrative example, the orbital speeds correspond roughly to binary components with the masses of Earth and Mars. Note that the smaller object's speed drops to about $v_{esc}/\sqrt{2}$, which is sufficient to place it on a circular orbit at the semi-major axis of Himalia, Jupiter's largest irregular satellite. A pair of objects closer to Himalia's mass, however, would orbit each other at speeds of only tens of meters per second, allowing capture only to orbits that are much more eccentric and distant than the actual orbits of the known irregulars.

The separation of the binary ($r_B = 2a_B$, for equal-mass pairs on circular orbits) plays a key role in determining whether a given encounter will result in capture. From Eq. 2.2, we can see that a smaller separation imparts a higher speed change upon disruption, increasing the probability of capture. However, the separation must be large enough that the binary can actually be disrupted. Equation 2.1 indicates that, not surprisingly, a large separation makes the binary easier to split. The separation that optimizes capture, then, is one just wide enough that the binary is disrupted. In addition, the tidal radius is important: the speed change needed for capture ($v_{CM} - v_{esc}$, the difference between the two horizontal lines in Fig. 2.1) decreases for closer approaches. Thus deeper encounters are more likely to lead to captures.

In much of the current work, we consider the simplified case where Jupiter orbits the Sun along a circle. In this case, the Jacobi constant (C_J) for the planet-Sun-interloper three-body problem is a very useful predictor of the interloper's potential for capture, taking on the role of v_∞ from the two-body approximation. In a frame rotating with Jupiter's orbit around the Sun,

$$C_J = n^2(x^2 + y^2) + 2 \left(\frac{1 - \mu}{r_\odot} + \frac{\mu}{r_P} \right) - \dot{x}^2 - \dot{y}^2 - \dot{z}^2, \quad (2.3)$$

where n is the planet's orbital mean motion, x and y are coordinates of the interloper's position and \dot{x} , \dot{y} , and \dot{z} are coordinates of its velocity. In addition, $\mu = \frac{M_P}{M_\odot + M_P}$ (with M_\odot the mass of the Sun and M_P the mass of the planet), and r_\odot and r_P are distances from the interloper to the Sun and planet, respectively. The Jacobi constant is given here in dimensionless units in which G , the Jupiter-Sun distance, and the sum of the solar and jovian masses are equal to 1.

Although our model contains four bodies, and the Jacobi constant is a three-body construct, it is an excellent approximation to consider the CM of the binary

as one body moving in the Sun-Jupiter system up until the point of disruption. The gravitational energy between the binary components is negligible after they separate. Thus after disruption, we essentially have two separate three-body problems, one for each binary component, and we can make use of the Jacobi constant throughout the entire simulation.

If $C_J \geq C_{J,crit}$, the critical value for capture, bodies in the vicinity of the planet are bound by so-called zero-velocity curves (ZVCs) that enclose Jupiter and constrain particle motions (Fig. 2.2). For Jacobi constants lower than $C_{J,crit}$ (i.e., higher energies), one large zero-velocity curve surrounds both Jupiter and the Sun and bodies can enter and exit Jupiter’s Hill sphere freely. The critical Jacobi constant represents the boundary between these possibilities. Murray and Dermott (1999) give its value: $C_{J,crit} \approx 3 + 3^{4/3}\mu^{2/3} - 10\mu/3$. For the Jupiter-Sun system, which is the focus of the current work, $\mu = 9.53 \times 10^{-4}$ and $C_{J,crit} \approx 3.0387$. At the L_1 Lagrange point, an orbit with $C_J = C_{J,crit}$ would have speed $v_{L_1} = 0$, while orbits with smaller C_J would have $v_{L_1} = \sqrt{C_{J,crit} - C_J}$. This speed, v_{L_1} , can be considered an analog to v_∞ from the two-body case.

Figure 2.3 illustrates a typical capture involving Jupiter. In the bottom panel, the Jacobi constant of the binary pair prior to its split is lower than the critical value, meaning that initially, the binary has too much energy to be bound. The small oscillations in the bodies’ pre-disruption C_J are due to gravitational interactions between the binary components. At the time of disruption ($t \approx 8$ yr), one component sharply gains energy (C_J decreases), while the other component experiences a corresponding energy loss (C_J increases). In this example, one component’s final C_J is higher than the critical value, signifying that it is permanently bound to Jupiter. Though the Jacobi constant is very valuable when considering a circularly orbiting Jupiter, a disadvantage is that it cannot be extended to cases with non-

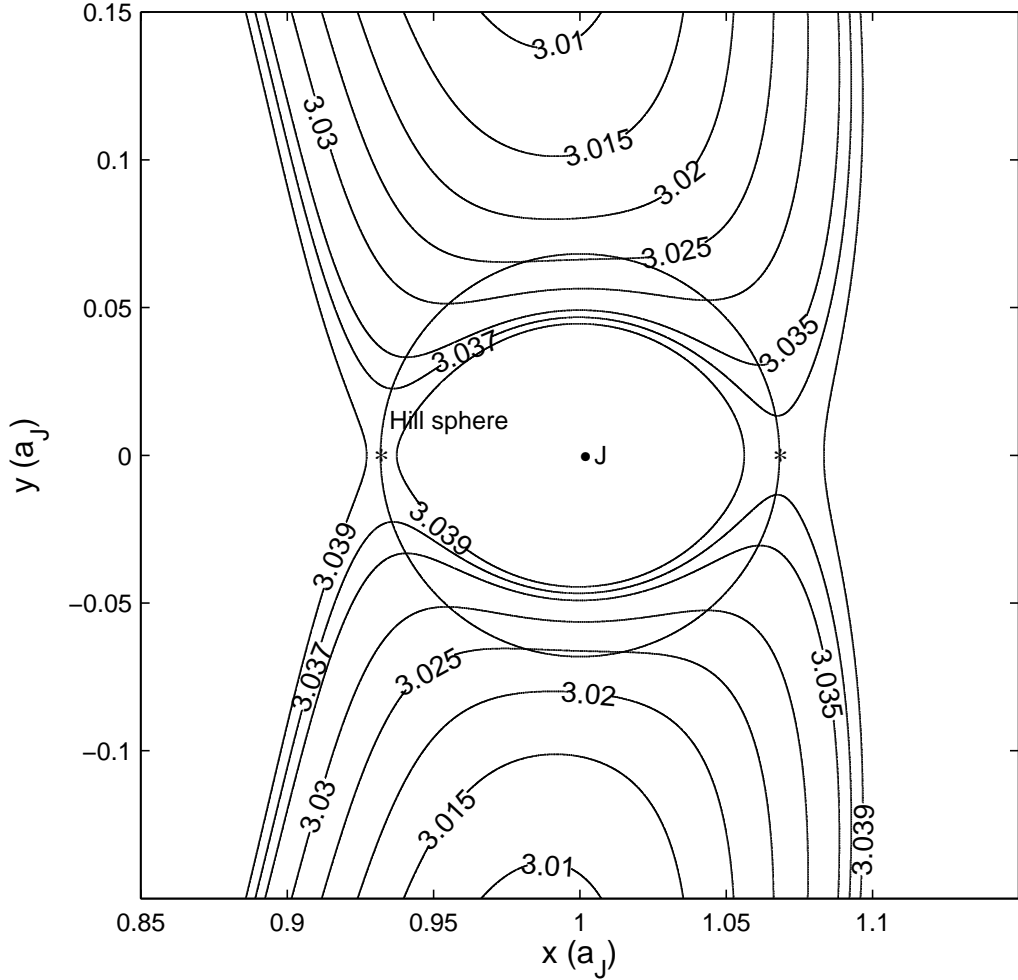


Figure 2.2 The Hill sphere of Jupiter (central dot marked ‘J’) with zero-velocity curves (ZVCs) corresponding to the labeled Jacobi constant (C_J) values. The Sun is to the left at (0,0) and the Jupiter-Sun separation (a_J) is used as the unit of distance. The two asterisks are located at the planet’s L_1 (0.933, 0) and L_2 (1.070, 0) Lagrange points. The critical Jacobi constant ($C_{J,crit} \approx 3.0387$) separates orbits bound to Jupiter ($C_J > C_{J,crit}$) from those free to escape ($C_J < C_{J,crit}$).

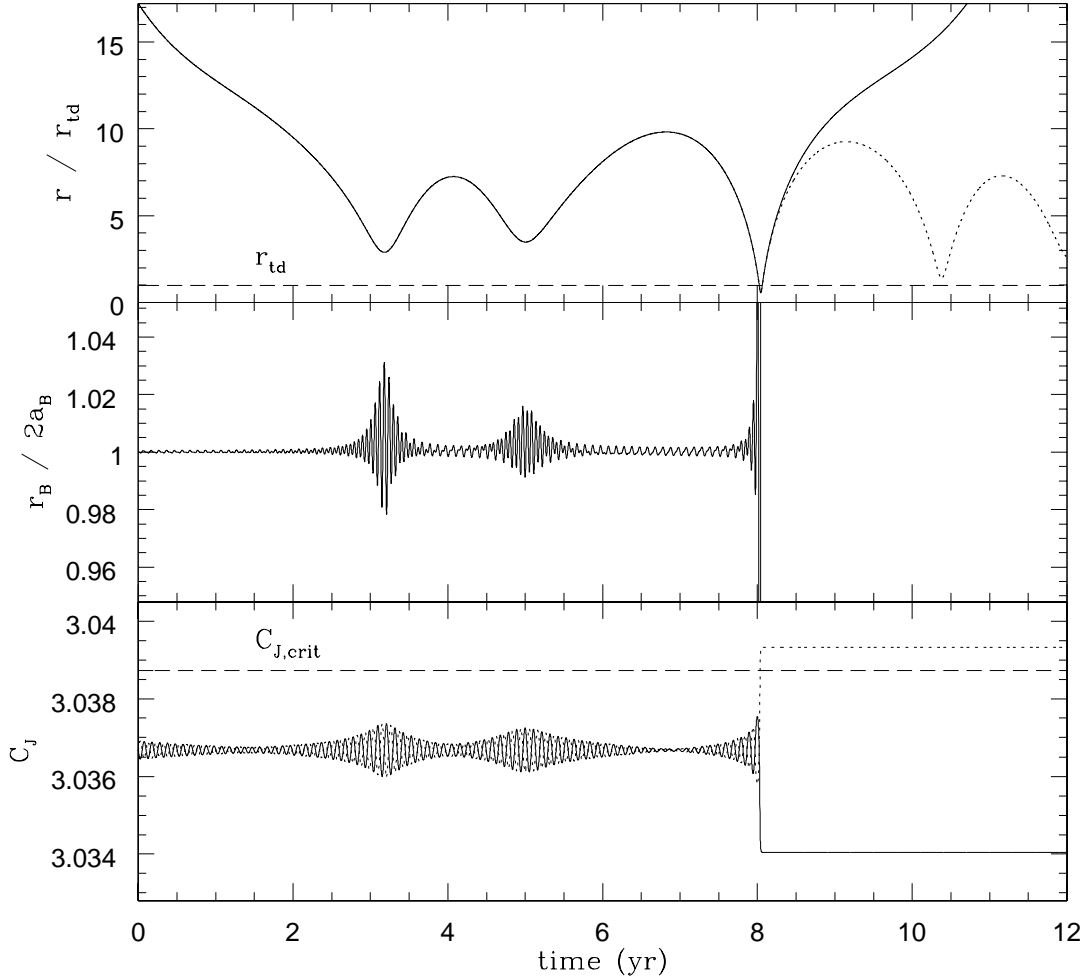


Figure 2.3 Distance from the binary components (each 225 km in radius) to Jupiter (r) is plotted in units of the tidal disruption radius ($r_{td} \approx 65 R_J$) in the top panel; the middle panel shows the binary's separation (r_B) over time, in units of its initial separation ($2a_B \approx 65 R_B$); and the bottom panel displays the Jacobi constant of each component. The binary's initial C_J corresponds to $v_{L1} = 0.6$ km/s. The speed change upon disruption is approximately equal to the binary's mutual orbital speed (≈ 23 m/s). One component is plotted with a solid line and the other with a dotted line throughout the figure. Dashed lines indicate the tidal disruption radius (top panel) and critical Jacobi constant (bottom panel).

zero planetary eccentricity. In this work, we make the simplifying assumption that $e_J = 0$ (rather than the true value of ~ 0.048) in order to better elucidate important physics of the problem.

In Fig. 2.4, we plot the orbits of the binary components shown in Fig. 2.3. Low-speed orbits like these are characterized by multiple close passes by the planet (cf. Hamilton and Burns 1991). The separation is disturbed by the strong tidal force during each of these passes, but the binary splits only after it comes within the tidal disruption radius (see top and middle panels of Fig. 2.3).

The binary capture mechanism is most effective at producing permanent or long-lived captures if i) the mutual orbital speed of the binary is high, and/or ii) the encounter speed is low. Agnor and Hamilton’s (2006a) work examined Neptune’s moon Triton, which is somewhat of a special case because it fulfills both of these criteria – its size means that its orbital speed around a close companion would be high, and typical encounter speeds at Neptune in the early stages of planet formation are relatively low.

The direct three-body capture mechanism is much less effective for most other irregular satellites which are ~ 100 km or smaller in radius. Furthermore, due to Jupiter’s size and proximity to the Sun, encounter speeds at the semi-major axes of its irregular satellites are relatively fast, $v_{CM} \approx 3$ km/s. To produce a large enough energy change for capturing directly to the current satellites’ locations, binary components must be orbiting each other at speeds comparable to their encounter speeds. This would require binary companions of order Mars- or Earth-sized (Agnor and Hamilton (2006b); see Fig. 2.1) – an uncommon occurrence even in the early Solar System.

Accordingly, in this work, we relax the requirement that moons are captured directly to their present orbits. In the example discussed above (Fig. 2.4), which

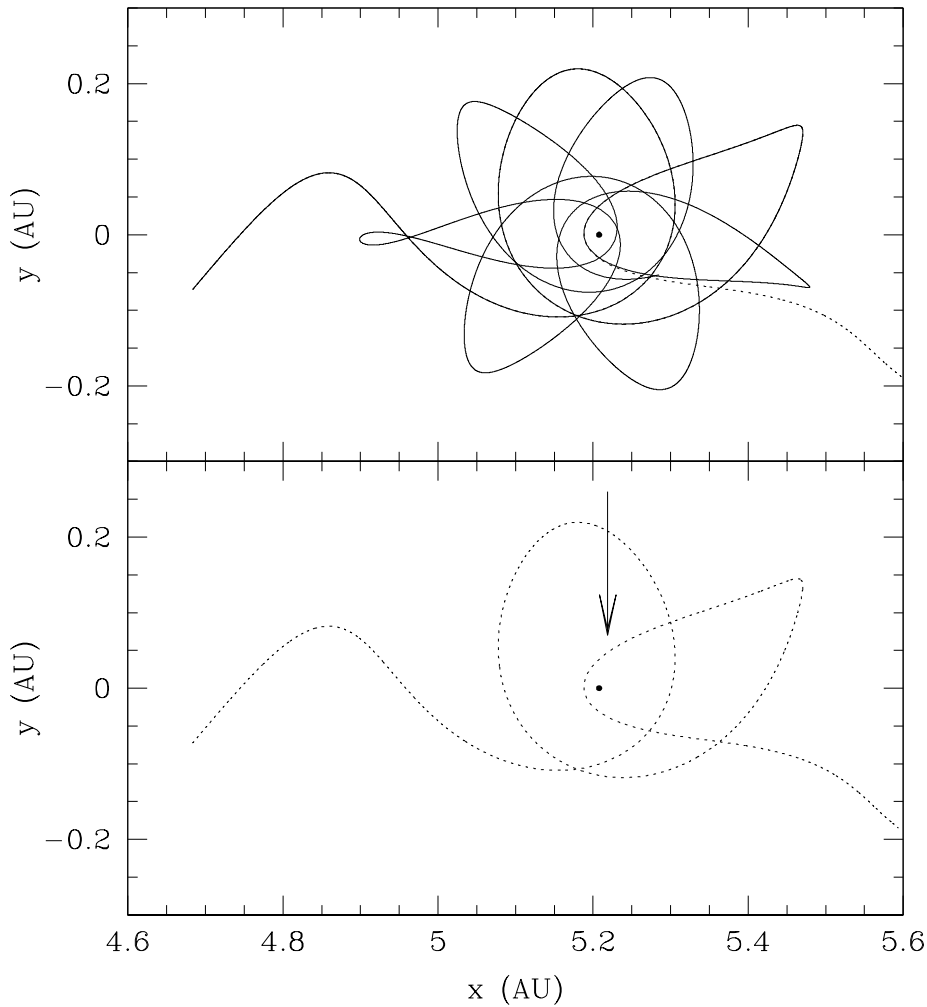


Figure 2.4 The orbits of the binary components discussed in Fig. 2.3, in a frame co-rotating with Jupiter's orbit around the Sun. Jupiter is the dot near the center of each panel, and the Sun is located to the left at (0,0). The components are plotted together in the top panel, with solid/dotted lines corresponding to those in Fig. 2.3. The objects are bound to each other as they approach Jupiter from the left side of each panel. A close approach to the planet tidally disrupts the binary, sending one component (dotted line) out of the system and causing the other component (solid line) to be permanently captured by the planet. The bottom panel contains only the orbit of the component that escapes, with an arrow marking the location where the binary's separation first exceeds 102% of its original value. About equidistant on the other side of the planet, the binary's separation is more than twice its initial value.

is typical, the final orbit of the captured satellite extends almost to Jupiter’s Hill radius (r_H), whereas the actual satellites at Jupiter are significantly more tightly bound. We investigate the idea that the objects were first captured to these distant orbits and a subsequent period of orbital evolution (e.g., by weak gas drag) led them to their current configurations.

The post-capture evolution is a key component in our model because it allows for capture from small binary pairs, even though they deliver satellites to very distant orbits. Binaries with primaries of order 100 km were certainly much more numerous than those with planet-sized primaries, even in the early Solar System. Models that rely on gas drag for capture (e.g., Pollack *et al.* 1979) require both i) dense gas (to enable capture) and ii) rapid dispersal (to prevent satellite loss to the planet). By contrast, our model requires no gas for capture and puts only weak constraints on gas required for orbital evolution. In particular, we require only that the product of the gas density and its residence time around Jupiter be large enough that the requisite amount of evolution can occur.

2.3 Numerical model

The goal of this work is to characterize the overall effect of binaries on the probability of capturing bodies on planet-crossing paths. We focus primarily on captures at Jupiter, which has the most irregular satellites and has many sources of small bodies nearby. Also, as discussed above, three-body capture at Jupiter has been shown to be difficult because of the planet’s large size and the fast encounter speeds for approaching bodies. Thus these simulations provide a stringent test of our model.

Our integrations include the Sun, Jupiter, and a binary or single object, in a planet-centered frame. In order to examine binaries’ effectiveness at producing

long-lived captures, we compare them to captures of single-body interlopers. While only tidally disrupted binaries can be captured permanently, unbound single bodies can remain near the planet for long periods of time (e.g., Astakhov *et al.* 2003). We define a ‘capture’ to be a body that remains near Jupiter for 1000 years, the duration of each simulation. This choice of duration is long compared to the crossing time of Jupiter’s Hill sphere. Furthermore, we define ‘binary capture’ to mean capture of one or both of the bodies that originated together as binary components. Note that these definitions encompass both permanent (energetically bound) and long-lived temporary captures. With captures of single bodies as a baseline, we are able to measure the enhancement due to binaries.

Our simulations are performed with *HNBody*, a hierarchical N -body integration package, and *HNDrag*, a companion code for applying non-gravitational forces to the particles and for detecting close approaches (Rauch and Hamilton 2002). For most of this work, we use only the close-approach detecting capabilities of *HNDrag* and include only gravitational forces. *HNBody* contains three types of integrators: symplectic, Bulirsch-Stoer, and Runge-Kutta. Bulirsch-Stoer and Runge-Kutta are adaptive-stepsize integrators for which unperturbed trajectories are straight lines and all relevant forces (i.e., gravity from Jupiter and the Sun, and all other perturbations) are applied to bend the orbit to its true path. The symplectic integrator begins with the assumption of an elliptical trajectory and corrects for the particle’s true path by applying only the perturbation forces. For this reason, the symplectic integrator is generally much more efficient than the other two when integrating lightly perturbed orbits. However, in our tests, we determined that the adaptive-stepsize Bulirsch-Stoer integrator is much more efficient than the fixed-stepsize symplectic integrator here because while a small stepsize is needed initially to resolve the orbital motion around the binary CM, it can be greatly increased after disruption.

Thus we use *HNBody*'s Bulirsch-Stoer integrator, with a specified accuracy of one part in 10^{14} .

We ran about 200 sets of three- or four-body simulations examining a range of Jacobi constants for each interloper (2.95–3.037, corresponding to a range of v_{L_1} from 3.9 to 0.5 km/s), as well as varying the binary components' radii (65-, 100-, and 125-km) and separations (1–1000 body radii). Initially, all of the binaries were given equal-sized components. For each set of parameters, we generated 10,000 binaries or single objects, for a total of $\sim 2 \times 10^6$ simulations, each following the bodies for 1000 years. We started all of the interlopers of a given set at the same distance from the planet, ranging from 1.0 to 1.4 r_H . (Section 2.7 contains a discussion of the effects of starting distances on capture statistics.) The choice of Jacobi constant and starting distance constrains the possible initial positions of the binary CM. Figure 2.2 shows Jupiter's Hill sphere overplotted with ZVCs corresponding to the Jacobi constants that we studied. Bodies are energetically unable to cross their zero-velocity surfaces, and thus starting with, say, $C_J = 3.037$ at 1.0 r_H from the planet restricts the body's initial position to the two small 'endcaps' of the Hill sphere along the Jupiter-Sun line. For smaller C_J , these allowed areas are larger, and they finally encompass the entire Hill sphere for $C_J \lesssim 3.025$. The bodies' initial speeds are also constrained by the specified Jacobi constant, and we chose the velocities to point in random inward directions.

For simplicity, we set the binary components to orbit each other on circles. Elliptical binary orbits would give a smeared-out distribution of energy changes from disruption of a given trajectory; although we have not tested this carefully, we suspect that binary eccentricities would have only a minor effect on our results. We have also chosen the binary angular momentum to be perpendicular to Jupiter's equatorial plane. Though this choice of angular momentum influences the final dis-

tribution of capture rate vs. inclination, we will see later (Section 2.7) that other effects have a greater impact on the final inclination distribution and that we cannot compare rates across inclinations for multiple reasons. We ran each initial condition with five different binary orbital phases (equally spaced mean anomalies) and averaged all capture statistics over the five phases. Throughout the simulations, we monitored the bodies, weeding out very close approaches between any two objects and noting each body’s close approaches to Jupiter. (Collisions between binary members do occur, but these are rare and of limited interest, since the merged object simply behaves as a single interloper with the same CM speed.) To shorten the computational time required, we stopped integrations in which all of the incoming objects traveled further than 2–5 Hill radii from Jupiter, depending on the bodies’ starting distance from the planet.

2.4 Relationship between inclination and C_J

In our simulations, we find that the inclination of the approach trajectory is correlated with the initial Jacobi constant, which is helpful in providing physical intuition for the meaning of C_J . This correlation was first noticed numerically by Astakhov *et al.* (2003); here we confirm their finding numerically and provide an analytical explanation. Fig. 2.5 displays this C_J -inclination relationship. We see a clear correlation of C_J with mean inclination: lower Jacobi constants are indicative of retrograde orbits, while prograde orbits have larger C_J . For clarity, the plot shows only a representative population of bodies: 100-km binary members that result in a capture, with inclinations calculated at the closest approach of each body’s first pass by Jupiter. However, the relationship holds for all close approaches of binaries or single objects, captured or not. This plot provokes two main questions: what is

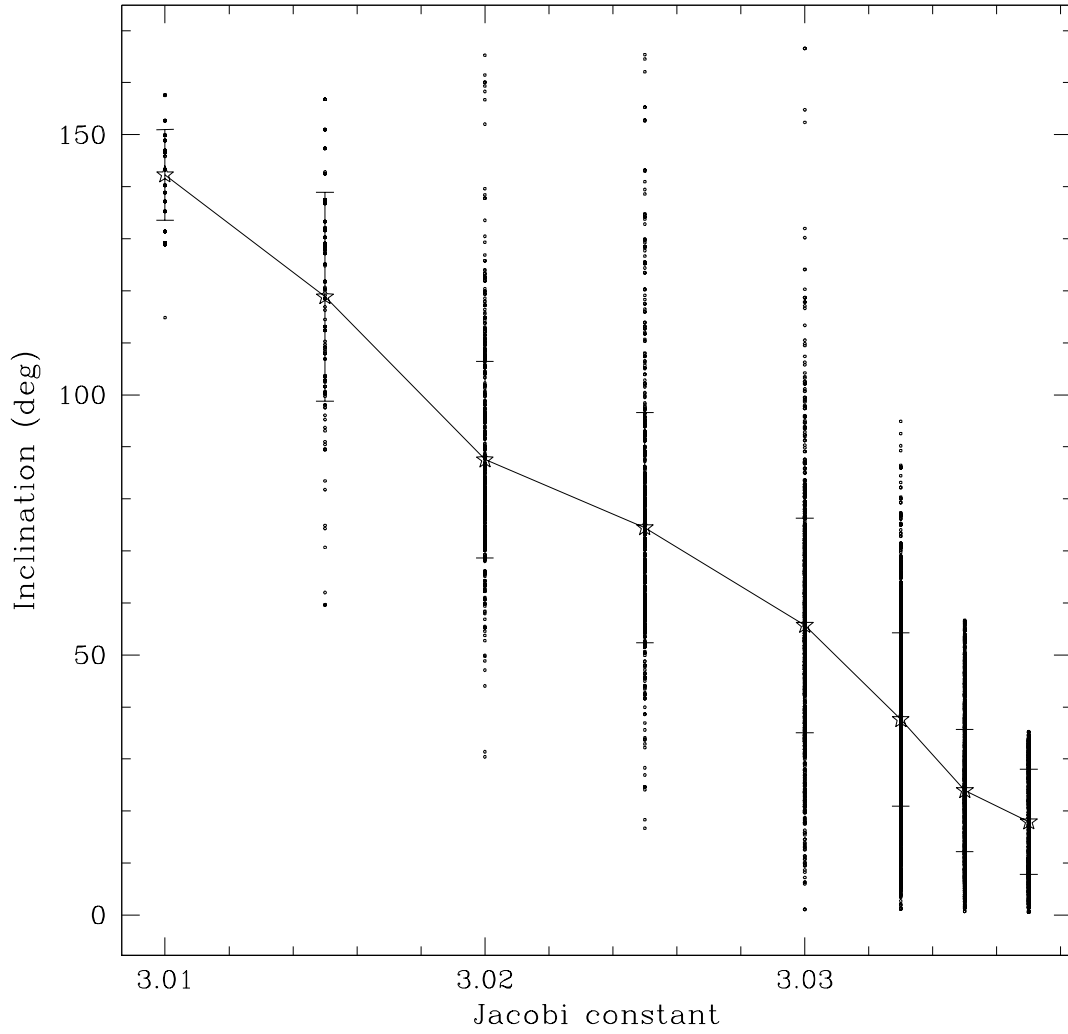


Figure 2.5 Inclination of 100-km captured binary components as a function of initial Jacobi constant, plotted for the bodies' first close approaches. Similar plots show that the relationship holds for all close approaches of binaries or single bodies, captured or not. Also plotted is a line connecting the mean at each Jacobi constant (marked by the stars) as well as 1- σ error bars.

the physical cause of this trend and why is there such high scatter in inclination at a given Jacobi constant? We address the question of scatter first.

One complexity in making this plot is that all orbital elements, including inclination, are poorly defined at large distances from Jupiter, as solar tides are comparable to Jupiter’s gravity at the Hill sphere. Accordingly, we were careful to calculate the inclinations only at orbital pericenter where solar tides are weakest so that inclination is always well-defined. Poorly-defined orbital elements, therefore, are not the source of the scatter in Fig. 2.5. Furthermore, the variations look nearly the same when we plot single objects rather than binaries, which is expected since disrupting the binary results in an energy change that only slightly alters C_J (e.g., Fig. 2.3). Finally, the scatter is present even when we consider one individual object’s multiple pericenter passages rather than those of an ensemble of objects. Thus the spread in inclination is real, and it is due to the response of a single captured object to the solar tidal force.

The scatter in inclination as well as the inclination- C_J trend can be understood analytically by writing the Jacobi constant in terms of planetocentric orbital elements rather than the heliocentric orbital elements used in deriving the standard Tisserand constant (Murray and Dermott 1999). We begin with the planet-centered ‘generalized Tisserand constant’ derived in Hamilton and Krivov (1997) (their Eq. 4) and neglect the solar tidal term since it is complicated and unimportant at pericenter where we measure inclination. We then non-dimensionalize the equation as in Section 2.2 (setting G , the Jupiter-Sun distance, and M_S+M_J equal to 1), and finally, to conform to standard usage (Murray and Dermott 1999), we add the constant 3 to the final result and find:

$$C_{J'} = 3 + \frac{3^{1/3}\mu^{2/3}}{\bar{a}} \left[1 + 2 \left(\frac{\bar{a}^3(1-e^2)}{3} \right)^{1/2} \cos(i) \right], \quad (2.4)$$

where μ is the mass ratio as defined above; $\bar{a} = a/r_H$; and a , e , and i are the captured satellite's semi-major axis, eccentricity, and inclination, respectively. Because we have neglected the solar tidal term and used planetocentric orbital elements, this expression is valid only near the planet where solar perturbations are weak.

For close orbits of the planet ($\bar{a} \ll 1$), orbit-averaging the effects of the tidal force shows that the semi-major axis \bar{a} remains constant. Accordingly, Eq. 2.4 leads directly to the Kozai constant, $K = \sqrt{1 - e^2} \cos(i)$. This constant explains the coupled oscillations in eccentricity and inclination that characterize the Kozai resonance. If K were precisely conserved, orbits would not be able to switch between $i < 90^\circ$ (which have $K > 0$) and $i > 90^\circ$ (which have $K < 0$). We do, however, see such prograde-to-retrograde transfers, which indicates that, as expected, neither \bar{a} nor K is constant for our distant orbits (see, e.g., Hamilton and Burns 1991). In addition, at apocenter where the solar tidal force is strongest, the orbital elements themselves are poorly defined and Eq. 2.4 is only approximate. Thus between each pericenter passage, the orbital elements (including inclination) are scrambled by the solar tidal force leading to dispersion like that seen in Fig. 2.5.

The trend observed in Fig. 2.5, decreasing inclination for increasing Jacobi constant, is neatly explained by Eq. 2.4. Testing the equation quantitatively, we estimate $\bar{a} = 0.5$ and $e = 0.7$ for a typical orbit of a body captured at Jupiter (e.g., Fig. 2.4). A purely prograde orbit ($i = 0$) gives $C_J' = 3.036$, while a purely retrograde orbit ($i = 180^\circ$) gives $C_J' = 3.020$. These values roughly correspond to the range of Jacobi constants seen in Fig. 2.5, despite the major approximations that we have made. The inclination- C_J correlation is strong enough that we will often use the term prograde to refer to orbits with $C_J \sim 3.03$, and retrograde to mean $C_J \sim 3.01$.

2.5 Modes of capture

For each binary-planet encounter, there are four possible outcomes: 1) neither component captures (hereafter known as ‘0C’), 2) one component captures (‘1C’), 3) both components capture together as an intact binary without splitting apart (‘2C-BIN’), or 4) the binary is disrupted and both components capture individually (‘2C-IND’). Recall our operational definition of ‘capture’ to mean bodies remaining near Jupiter for 1000 years. The frequency of each type of outcome depends on the characteristics of the binary. Fig. 2.6 shows the outcomes that result in a capture (i.e., 1C, 2C-BIN, and 2C-IND) for 65-km binary pairs with initial $C_J = 3.037$, as a function of the initial separation, r_B , of the binary. (We later generalize to examine other masses and Jacobi constants.) The separation can be altered significantly prior to disruption during close approaches to the planet (e.g., Fig. 2.3). The number of captures for a set of single objects is also plotted for comparison; these must be temporary captures since there is no energy loss.

The rate of 2C-BIN captures is largest when the separation is small (and thus the components are tightly bound to each other). For small-enough separations, the tidal disruption radius is so close to the planet that very few binary orbits cross it (see Eq. 2.1). Here, most of the binaries remain intact, and the 2C-BIN rate nearly matches that of the single objects. When we increase the binary separation, more binaries are split, and the 2C-BIN capture percentage monotonically drops to zero, as expected.

Disrupting binaries leads to more possibilities for capture of individual objects. Accordingly, as the separation increases, the 1C and 2C-IND capture rates rise from zero. For the 1C population of 65-km objects with $C_J = 3.037$, there is a peak in capture efficiency of ~ 5 times that of a single body at a separation of ~ 20 body

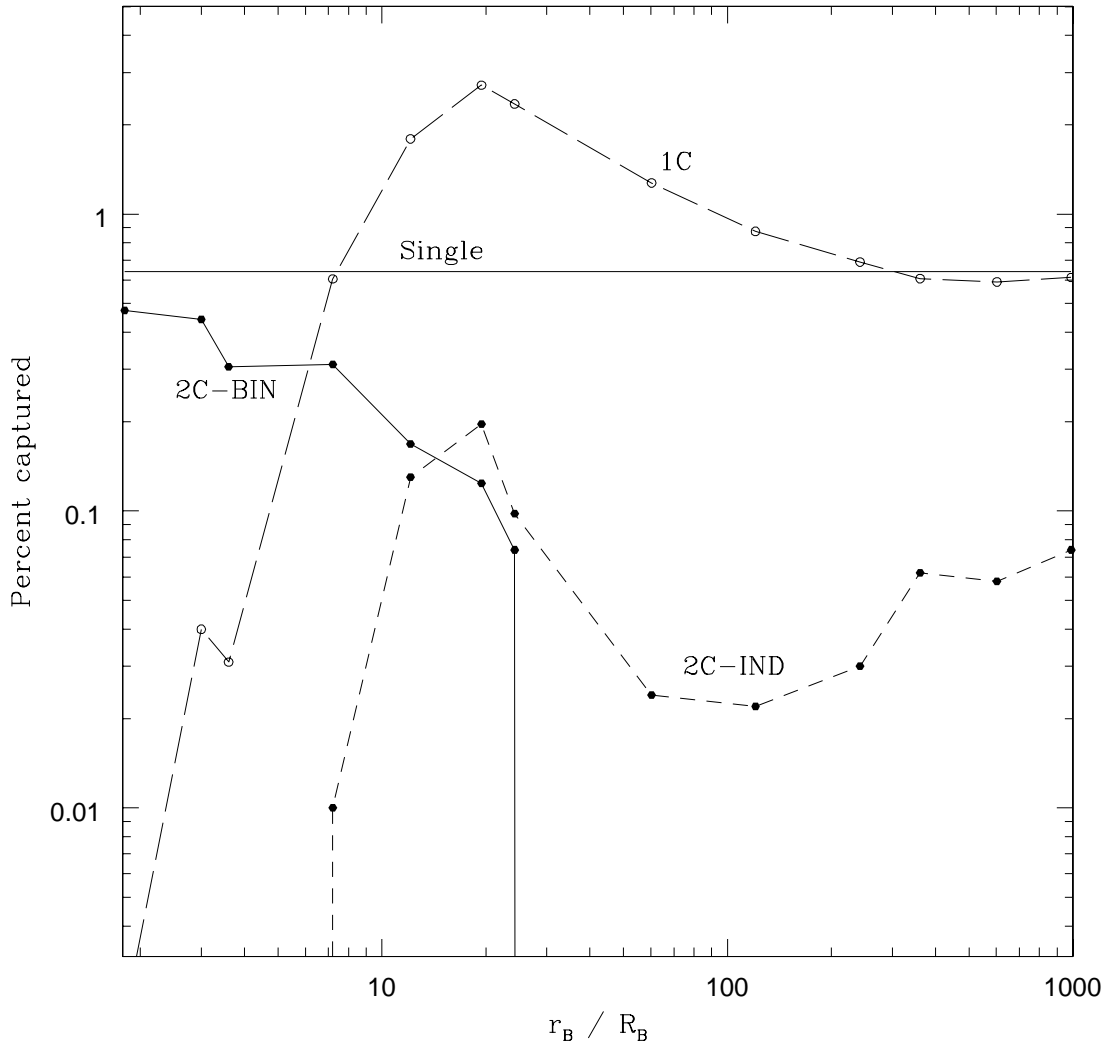


Figure 2.6 Three modes of capture for integrations of $R_B = 65$ -km binary pairs with $C_J = 3.037$, as a function of the separation of the binary (r_B): one component captures ('1C'), the binary splits and both capture independently ('2C-IND'), or the binary remains bound and captures as a pair ('2C-BIN'). We plot the capture percentage for objects (rather than binaries) to facilitate comparison with single bodies (upper solid line). Recall our working definition of capture to mean bodies still orbiting the planet after 1000 years. Note that the 2C-BIN curve approaches the value for singles at small separations while the sum of the 1C and 2C-IND captures rates approaches the same value for large separations.

radii (R_B). This separation represents the optimal balance between disrupting a high percentage of the binaries and delivering the most energy upon disruption. The optimum separation varies depending on the mass of the binary. At larger separations, the binding energy decreases, leading to smaller energy kicks and a diminished capture rate.

The 2C-IND percentage has a peak at the same separation as the 1C group. These binaries likely split during orbital phases where the energy is distributed almost equally between the components, with $v_1 \approx v_2 \approx v_{CM}$ (see Fig. 2.1). The number of 2C-IND captures is never more than a few percent of the 1C captures, but the two populations peak at $r_B \sim 20 R_B$ for the same reasons. Binaries with still wider separations are disrupted with a smaller energy change. Because of this, the two components are more likely to have similar energies and post-disruption fates, causing an increase in 2C-IND captures at larger separations.

Unlike the case for 1C and 2C-IND capture where energy is lost and capture can be long-lived or even permanent (as in Fig. 2.3; note only one member of a 2C-IND binary can be permanently captured), capture of singles or intact binaries (2C-BIN) is necessarily temporary. This could be an advantage for 1C captures, which have more stable, lower-energy initial capture orbits. The details of the final comparative satellite yields depend on the subsequent orbital evolution, which is determined by the gas present at the time of capture and its dissipation timescale.

2.6 Effects of binary mass and orbital separation

Having explored the physical meaning of C_J and the possible types of captures, we now discuss the results of the numerical simulations. In this section, we consider cases of equal-mass binaries encountering Jupiter with the planet on a circular or-

bit, and we examine the effects of the bodies' masses, binary separations, and initial Jacobi constants. We performed integrations over a range of Jacobi constants: $2.95 \leq C_J \leq 3.037$, where $C_J \approx 3.0387$ is the critical value above which transfer orbits between Jupiter and the Sun are impossible (see Fig. 2.2). For $C_J \leq 2.99$ (corresponding to a v_{L_1} of 2.9 km/s), no captures resulted for any of the parameters we tested, although capture at these low Jacobi constants could certainly occur for larger-mass binaries. For now, we consider the fate of bodies started from the Hill sphere (following Astakhov *et al.* (2003)); in Section 2.7, we discuss the importance of alternative starting distances.

In discussing our results, we refrain from using orbital elements and instead describe the capture orbits in terms of their initial Jacobi constants. We do this because the energy change imparted upon disruption is very small and leads to highly extended orbits with poorly defined orbital elements (see, e.g., Fig. 2.4).

We examined masses corresponding to pairs of objects each with radii 65-km, 100-km, and 125-km (assuming a density of ~ 2 g/cm³). Fig. 2.7 displays the results of these mass studies. We see that capture rates increase for higher masses: the 125-km capture rate is slightly higher than the 100-km rate throughout the range of Jacobi constants, and they differ most significantly from 65-km binary pairs for $C_J > 3.03$.

For single objects, mass has no effect on capture probability, but for binaries, larger total mass leads to more rapid orbital speeds and a higher speed change upon breakup. This can be seen by eliminating a_B from Eqs. 2.1 and 2.2, with mass ratio ($\frac{m_2}{m_1+m_2}$) and tidal disruption distance (r_{td}) held constant; the result is $\Delta v_1 \sim (m_1 + m_2)^{1/3}$. Accordingly, larger masses generally lead to increased capture rates.

Another important result is that capture rates from binaries are extremely sen-

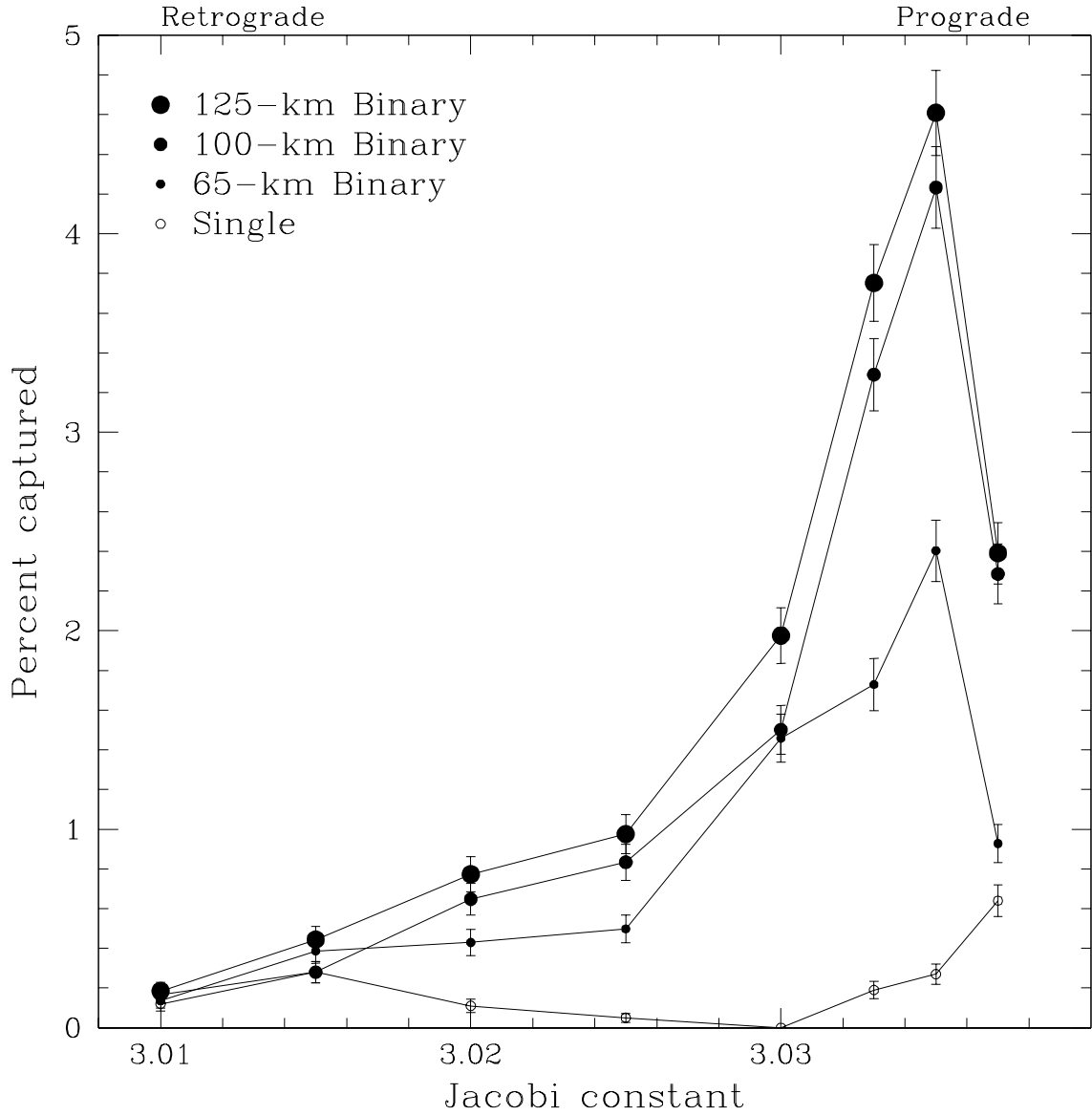


Figure 2.7 Capture percentages for binaries of different masses compared to single objects. All bodies were started on Jupiter’s Hill sphere. For each binary mass, a single separation was used over the range of initial Jacobi constants: 471 km = 7.25 binary radii (R_B) for the 65-km binaries, 1225 km = 12.25 R_B for the 100-km set, and 1512 km = 12.10 R_B for 125-km binaries. These separations give near maximum capture rates for the majority of the Jacobi constants tested, with the exception of the highest C_J , where the optimum separation is closer to 20 binary radii for all tested sizes.

sitive to the binary’s separation, $r_B = 2a_B$. For each of the masses we examined, we determined the optimum separation of the binary required to achieve the maximum capture probability. We used Eqs. 2.1 and 2.2 to guide our separation selection, and we integrated each point on Fig. 2.7 with several different binary separations to determine the optimal value.

In Fig. 2.7, we have plotted statistics using a single separation for each mass over the range of Jacobi constants. For most of the Jacobi constants studied for a given mass, the optimal separations are very similar, $\sim 10 R_B$. An important exception is for the highest C_J value tested, 3.037 (recall that this corresponds to mostly low-speed prograde encounters – see Fig. 2.5), which had maximum captures at a larger separation ($\sim 20 R_B$) than the typical optimal value. Because we have not plotted this optimal value in Fig. 2.7, the curves decline sharply at $C_J = 3.037$. As is clear from Section 2.5, optimizing the separation makes a significant difference in capture rate, especially for binaries whose C_J values are close to the capture threshold. Changing from $\sim 10 R_B$ to the optimal $20 R_B$ for $C_J = 3.037$ increases the capture percentage from $\sim 2\%$ to $\sim 10\%$ (100-125 km objects) and $\sim 1\%$ to $\sim 3\%$ (65-km, see Fig. 2.6).

Binary capture rates also appear to depend strongly on initial Jacobi constant. It is tempting to compare capture efficiencies for low and high Jacobi constants (retrograde and prograde orbits). A direct comparison of these rates, however, cannot be made for reasons that will become apparent in the next section. We can, however, compare the binary statistics to those of single objects. The bodies that originate in binaries capture with similar rates as the single objects below $C_J \approx 3.015$ (Fig. 2.7), but as C_J increases, the effects of the binaries become more visible, rising by an order of magnitude in efficiency at delivering objects to Jupiter. One reason for this is probably that the retrograde binaries are harder to split than

progrades because of their orientation to the planet (Hamilton and Burns 1991). Another explanation, particularly for the highest initial Jacobi constants, is that these encounters are close to the critical energy barrier for capture, and so the energy change from disruption of the binary is more likely to result in capture.

2.7 Effects of starting distance

2.7.1 Contamination from bound retrograde orbits

Thus far we have discussed results from initial conditions that launch objects from the Hill sphere. In the course of this study, we discovered that the choice of starting distance can significantly affect the capture statistics. While the Hill sphere is defined as a rough stability boundary beyond which the Sun’s tidal influence is stronger than the planet’s gravity, in practice, stable retrograde orbits can extend out to distances slightly beyond the Hill radius (see, e.g., Hamilton and Burns 1991). In contrast, stable prograde orbits (e.g., Fig. 2.4) are always well within the Hill sphere. Starting the integrations with bodies on the Hill sphere, then, risks starting on an already-stable retrograde orbit. This causes ambiguity in the capture statistics—which orbits were always near Jupiter and which truly came in from infinity?

We demand that true captures originate in heliocentric orbit and transition to planet-centered orbits, remaining for at least 1000 years. To differentiate between these and misleading ‘captures’ from bodies that are already orbiting the planet at the beginning of our integration, we took the single-body capture orbits and integrated the initial conditions backwards in time for 1000 years. We then separated the captures that came in from infinity and those that were always present near the planet. We found that when starting on the Hill sphere, most of the resulting

retrograde captures of single objects at low C_J had always been orbiting the planet and were in fact not true captures.

We examined several other launch distances and determined that starting from 1.1 Hill radii (r_H) and beyond eliminates nearly all contamination from already-stable retrograde orbits. Figure 2.8 compares the capture rates for single objects beginning from 1.0 r_H and 1.1 r_H . We see that while the high- C_J captures are uncontaminated, launching from 1.0 r_H for $C_J < 3.03$ leads to many false captures. In fact, over one-third of all 1.0 r_H captures are contaminations. (This fraction is much smaller for binaries, where there are many more prograde captures than retrograde.) When the objects are launched from 1.1 r_H , we see no artificial captures at all. Similar tests at 1.2 r_H and 1.4 r_H also show no false captures. Although stable orbits do exist to these and larger distances (Hénon 1969), they are apparently extremely rare.

2.7.2 Scaling to different starting distances

So, is it safe to compare prograde and retrograde capture statistics for starting distances beyond 1.1 r_H ? Starting outside the Hill sphere results in a decrease in true captures over the full range of C_J (as seen in Fig. 2.8). This is expected, because fewer of these bodies experience close approaches with the planet. However, prograde captures are more drastically reduced than retrogrades. Determining the reason for this is critical to answering our question.

At high Jacobi constants ($\gtrsim 3.03$, which correspond to mostly prograde orbits), the binary's ZVCs are closed around the planet except for only a small neck on either side of Jupiter, toward and away from the Sun (see Fig. 2.2). In contrast, lower Jacobi constants (and thus retrograde orbits) allow for more freedom of movement in the region between the Sun and Jupiter. Retrograde orbits can approach the

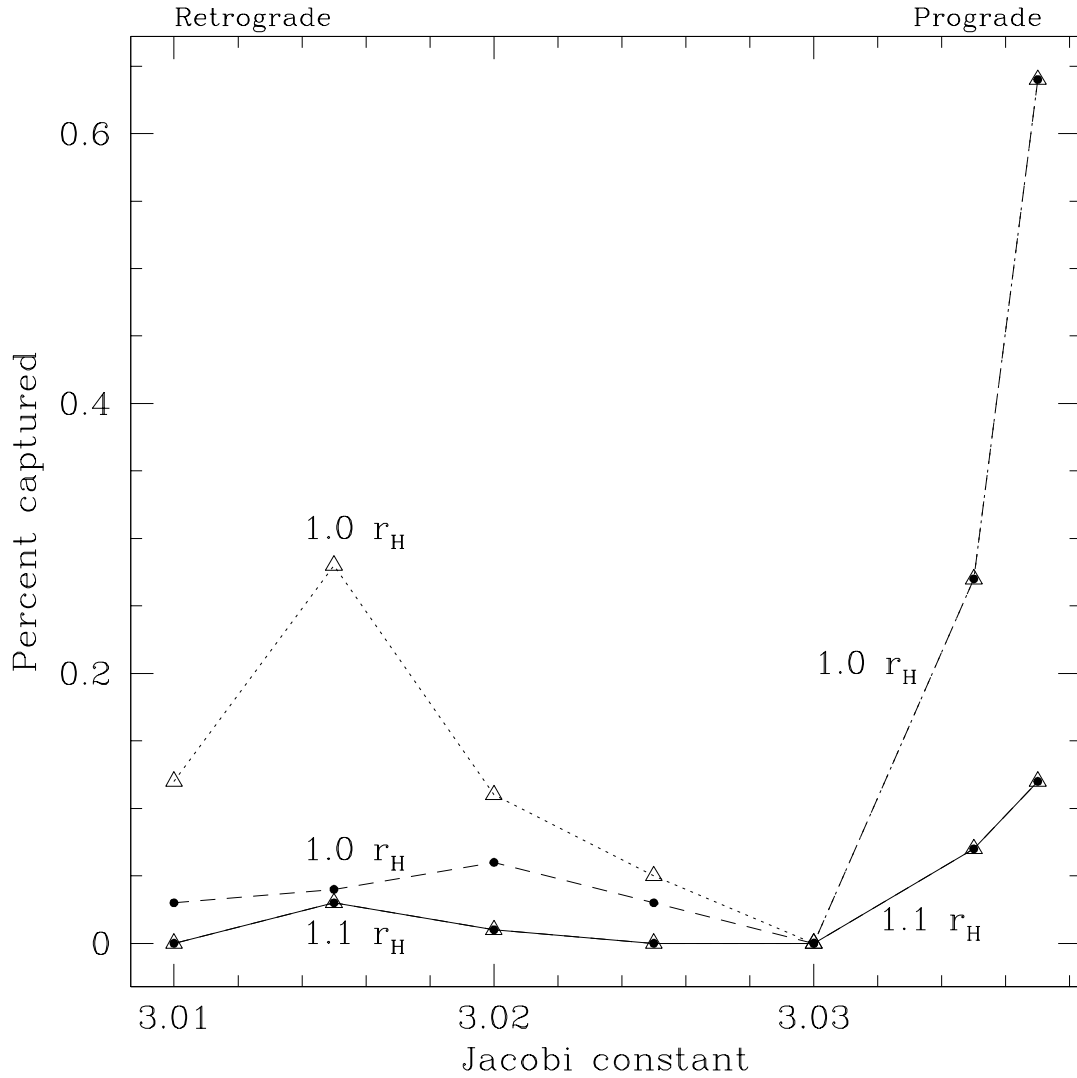


Figure 2.8 Single objects integrated from two launch distances. True-capture curves (with points that are solid circles) show only those captures that originated far from Jupiter, while curves that show true plus contaminated captures (with open triangles) also include objects that were stably orbiting the planet at the beginning of the integrations. For launch on the Hill sphere ($1.0 r_H$), we see that the prograde orbits (high C_J) are not affected at all, while most of the retrograde orbits (low C_J) are discovered to be false. For launches at $1.1 r_H$, the true and true-plus-contaminated curves overlap completely, showing that contamination by false captures is effectively zero.

planet from all directions, while progrades are limited to the entering via the narrow ZVC necks. Starting further than the Hill sphere means that a smaller fraction of the initial prograde trajectories pass through the zero-velocity necks and approach Jupiter, resulting in a decrease in captures. We tested the hypothesis that the shape of the prograde ZVCs is the primary reason for the decrease in prograde captures with the following procedure:

- 1) Determine the capture rates starting from $1.1 r_H$ and $1.2 r_H$.
- 2) Determine the crossing rate of $1.2 r_H$ orbits inside $1.1 r_H$.
- 3) Scale the $1.1 r_H$ capture rate by the crossing rate from step (2).

We use the statistics for $1.1 r_H$ and $1.2 r_H$ because they are free from any contamination from the false retrograde captures discussed above. The result of step (3) is what we expect the $1.2 r_H$ capture percentages would be if the ZVC shapes are the reason for the decline in prograde captures from $1.1 r_H$ to $1.2 r_H$. Comparing these scaled capture rates with the actual $1.2 r_H$ percentages (as shown in Fig. 2.9), we see that this scaling accounts for most of the difference between the two capture rates, to within 20%. This indicates that our prediction is valid.

In principle, these results also account for the reduction in true retrograde captures, but the number statistics are so low for retrogrades at these launch distances that the actual and scaled capture percentages are equivalent to within the error.

We find, then, that because of the differing geometries of their ZVCs, we cannot directly compare prograde and retrograde statistics. This is true even when starting beyond the limit for already-stable retrograde orbits, chiefly because prograde orbits are so sensitive to their initial distance. To circumvent this effect, we would have to start far enough away from the planet that further increasing the starting distance would result in an equal fractional decrease in captures for retrogrades and progrades – in other words, where the geometry of the prograde ZVCs is no longer the dominant

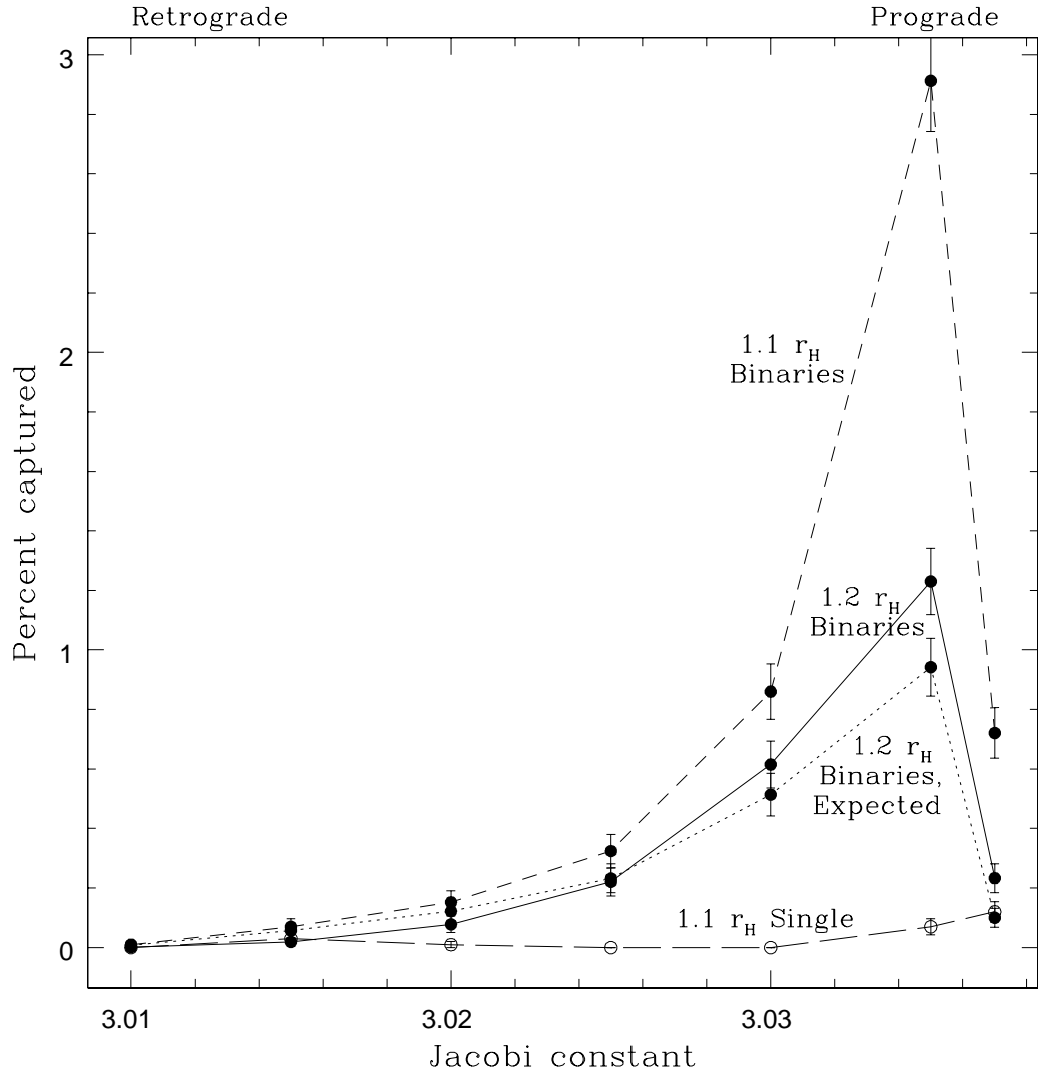


Figure 2.9 Capture rates of 100-km binaries that were launched from $1.1 r_H$ (upper dashed line), $1.2 r_H$ (solid line), and expected capture rates for $1.2 r_H$ (dotted line) calculated by scaling the $1.1 r_H$ rates by the percent of $1.2 r_H$ trajectories crossing interior to the 1.1 Hill radii. All are shown with $1\text{-}\sigma$ error bars. This scaling equalizes the capture percentages between the two launch distances to within 20%. For reference, the capture rate for single bodies starting from $1.1 r_H$ is also plotted; compare with Fig. 2.7.

reason for the decrease. Our simulations, out to $1.4 r_H$, did not reach this threshold and were limited by number statistics. We anticipate that comparing prograde and retrograde captures would require starting still further from the planet than our trials, and would demand much larger initial populations.

2.7.3 Starting from $1.1 r_H$ vs. $1.0 r_H$

Launching binaries from $1.1 r_H$ rather than $1.0 r_H$ results in an overall decrease in captures for the reasons described above, but many of the characteristics of the capture orbits remain relatively unchanged. For example, the inclination distribution for the $1.1 r_H$ captures is almost identical to the $1.0 r_H$ population plotted in Fig. 2.5. Also, comparing Fig. 2.9 with Fig. 2.7, we see that the trend in the capture percentage with C_J of the 100-km binaries at $1.1 r_H$ and $1.0 r_H$ are generally similar.

Figure 2.10 displays the modes of capture vs. Jacobi constant for 100-km binaries and single objects starting from both $1.0 r_H$ and $1.1 r_H$. With a starting distance of $1.1 r_H$, the capture rate below $C_J = 3.02$ is close to zero for all curves. This is because the $1.0 r_H$ captures in this range were likely artificial retrogrades that are eliminated when starting from $1.1 r_H$. Above $C_J = 3.02$, the curves are all diminished by a roughly comparable amount on the $1.1 r_H$ plot as compared to the $1.0 r_H$ version.

We note that other groups (including Astakhov *et al.* (2003) and Astakhov and Farrelly (2004)) have initiated bodies from the Hill sphere without considering how this affects the resulting statistics, most notably that many of their retrograde encounters are started on already-stable orbits. For future studies of capture near Jupiter, we recommend the following procedure: 1) generate bodies starting from $1.0 r_H$, 2) integrate each body backwards in time, 3) eliminate those that remain near the planet when integrated backwards, and 4) integrate the remaining bodies

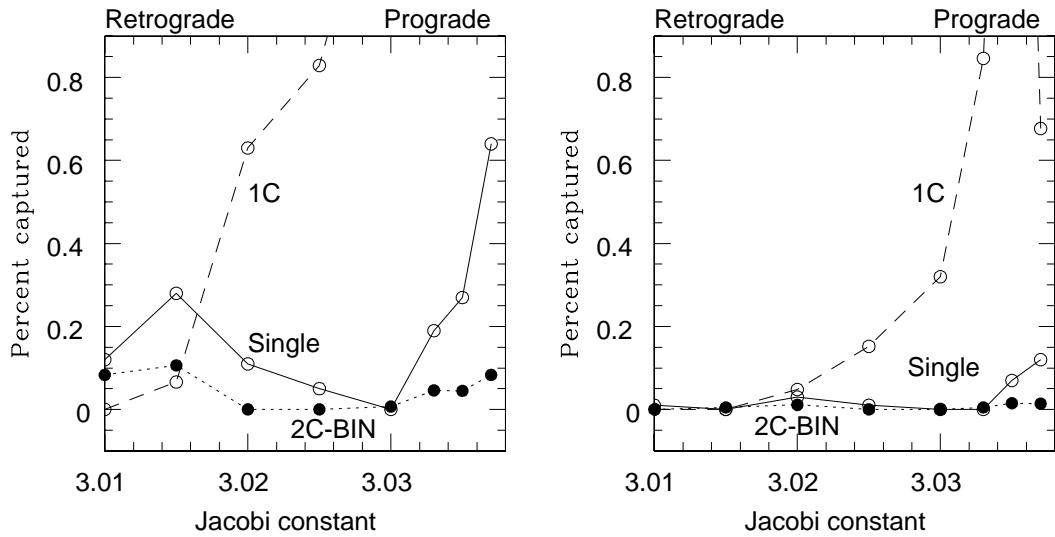


Figure 2.10 Modes of capture vs. Jacobi constant, for integrations of 100-km binaries starting at $1.0 r_H$ (left panel) and $1.1 r_H$ (right panel). The 1C-curve peaks (both at $C_J = 3.035$) are off the top of the plot at $\sim 4.2\%$ for the $1.0 r_H$ runs and $\sim 3.0\%$ for the $1.1 r_H$ group. The 2C-IND capture rates are extremely small for both starting distances (e.g., Fig. 2.6) and, for clarity, are not plotted here. The capture rates of single bodies are plotted for comparison.

in normal time direction. The benefits of this approach over simply starting from $1.1 r_H$ are that it eliminates all stable-retrograde contamination while preserving high number statistics. Note, however, that this procedure still does not allow a valid comparison between prograde and retrograde statistics. To obtain the true ratio of captured progrades and retrogrades, it would probably be best to start the interlopers on heliocentric orbits.

2.8 Scaling to unequal binary masses

The impulse approximation (Eqs. 2.1 and 2.2) implies that a binary component's likelihood of capture depends only on 1) the binary's tidal disruption radius and 2) the component's instantaneous speed, v , at the time of disruption. Accordingly, for any mass ratio $m_1 : m_2$ and semi-major axis a_B , we can find an equal-mass binary with the same r_{td} and the same component speeds as m_1 and another equal-mass binary that matches these values for m_2 . Setting r_{td} and v equal for the two mass ratios, we solve for the component mass, m' , and the semi-major axis, a_B' , of the equal-mass binary matching m_1 :

$$m' = \frac{4m_2^3}{(m_1 + m_2)^2} \quad (2.5)$$

and

$$a_B' = a_B \left(\frac{2m_2}{m_1 + m_2} \right). \quad (2.6)$$

The problem is symmetric, so for the equal-mass binary matching m_2 , we simply exchange m_1 and m_2 in the above equations.

We tested these predictions for 3:2 and 4:1 mass ratios and display the results in Table 2.1. Each of the equal-mass components captures with the same efficiency (to

Table 2.1. Mass ratio tests for binaries with $C_J=3.03$

Mass Ratio	Component Radii (km)	Total Binary Mass (10^{19} kg)	Separation (km)	m_1 Capture Percentage	m_2 Capture Percentage	Total 1C Capture Percentage
3:2	113-98	2.0	1350	0.54	<i>0.96</i>	1.50
1:1	85-85	1.0	1080	0.58	0.58	1.16
1:1	127-127	3.4	1620	<i>0.94</i>	<i>0.94</i>	1.88
4:1	124-78	2.0	1160	0.21	<i>1.17</i>	1.38
1:1	42-42	0.13	465	0.24	0.24	0.48
1:1	169-169	8.1	1860	<i>1.29</i>	<i>1.29</i>	2.58

Note. — Two experiments with binaries of unequal mass. The first four columns identify properties of the binary, while the final three columns list capture statistics (with $m_1 \geq m_2$). We used the impulse approximation (Eqs. 2.1 and 2.2) to determine the properties of equivalent equal-mass binaries that match the tidal disruption radius and speed of either m_1 (boldfaced) or m_2 (italicized). In all cases, our predicted percentages agree with the actual measurements to within about 10%.

within 10%) as either m_1 or m_2 . This is strong validation of the impulse approximation. This sort of scaling requires, of course, that the binary be split and therefore applies only to our 1C and 2C-IND results. By contrast, undisrupted binaries (2C-BIN) behave as single objects and have a capture efficiency that is independent of mass.

The impulse approximation allows us to make other predictions as well. For example, we can reverse the above scenario and predict the capture rates of two equal-mass binaries corresponding to one unequal-mass pair for which the capture rates of each component are known.

Further, given the capture rate for a single equal-mass binary, we can predict the capture efficiency of one component of an unequal-mass pair, if one parameter of the unequal-mass binary (m_1 , m_2 , $m_1 + m_2$, or a_B) is set. This means that each equal-mass pair matches to a whole family of unequal-mass binaries.

Finally, we can extend these techniques to guide large-scale simulations. Using the impulse approximation, and given equal-mass capture statistics for all combi-

nations of relevant masses and separations, we can predict the capture rates for *all* unequal-mass binaries – with any mass ratio, total mass, and separation. Similarly, knowledge of unequal-mass capture rates for one component of a binary with a fixed mass ratio allows us to estimate the capture efficiencies of *all* equal-mass binaries.

Scaling with the impulse approximation is a powerful way to predict capture rates. Practically speaking, it means that capture of any unequal-mass binaries can be predicted by studying just equal-mass cases, and accordingly, we have restricted our numerical studies to binaries with equal masses.

2.9 Jupiter’s eccentricity

Most scenarios, including our own, propose that irregular satellite capture occurred early in the Solar System’s history (Section 1.3). It is likely that Jupiter’s eccentricity was closer to zero at this time and its current value was acquired later. Thus we have chosen to use $e_J = 0$ in our simulations and believe that it is a reasonable assumption.

How would Jupiter’s current eccentricity affect capture? It is not straightforward to extend this study to a non-zero jovian eccentricity for the primary reason that the Jacobi constant is no longer a constant of the motion. Though Jupiter’s current eccentricity is small ($e_J \sim 0.048$), it causes the calculated C_J of an interloper to vary by ~ 0.2 over an orbit. This is a variation about ten times larger than our entire range of tested Jacobi constants. Thus we cannot simply assign an initial C_J to binaries or single objects approaching an eccentric Jupiter and compare the capture results with the equivalent circular case. Only for eccentricities less than a hundredth of Jupiter’s would the errors introduced in the Jacobi constant be acceptable.

The results of Astakhov and Farrelly (2004) suggest an order-of-magnitude lower capture probability for single objects in the eccentric case as compared to capture by a planet orbiting on a circle. However, their initial conditions were generated using the same Jacobi constant values in the eccentric and the non-eccentric cases. Because of the variation in C_J induced by eccentricity, their method actually produces a much larger range of Jacobi constants (and much higher approach speeds) for tests with an eccentric planet, and the results should not be directly compared with the circular case. We believe their capture rates for an eccentric Jupiter are artificially low for this reason.

We do not expect Jupiter's eccentricity to strongly affect capture. As the timescale for capture is much shorter than Jupiter's orbital period, the planet's instantaneous location is the most relevant factor. At pericenter, Jupiter's Hill sphere is slightly smaller than at its average distance from the Sun and encounter speeds are slightly higher, likely resulting in fewer captures. The opposite can be expected at apocenter, causing the effects of eccentricity to average out and probably produce little change in overall capture statistics. To truly know the effects of the planet's eccentricity would require large-scale integrations with the interlopers originating on heliocentric orbits. This is beyond the scope of our current work.

2.10 Survivability of captured objects

The post-capture orbits are initially very irregular and prone to collisions with Jupiter's Galilean satellites (particularly its outermost, Callisto) or the planet itself. Figure 2.11 displays the percent of captured bodies that are delivered onto orbits that do not cross Callisto, which currently orbits Jupiter at $26 R_J$. We begin by assuming that objects on Callisto-crossing orbits are lost and relax that assumption

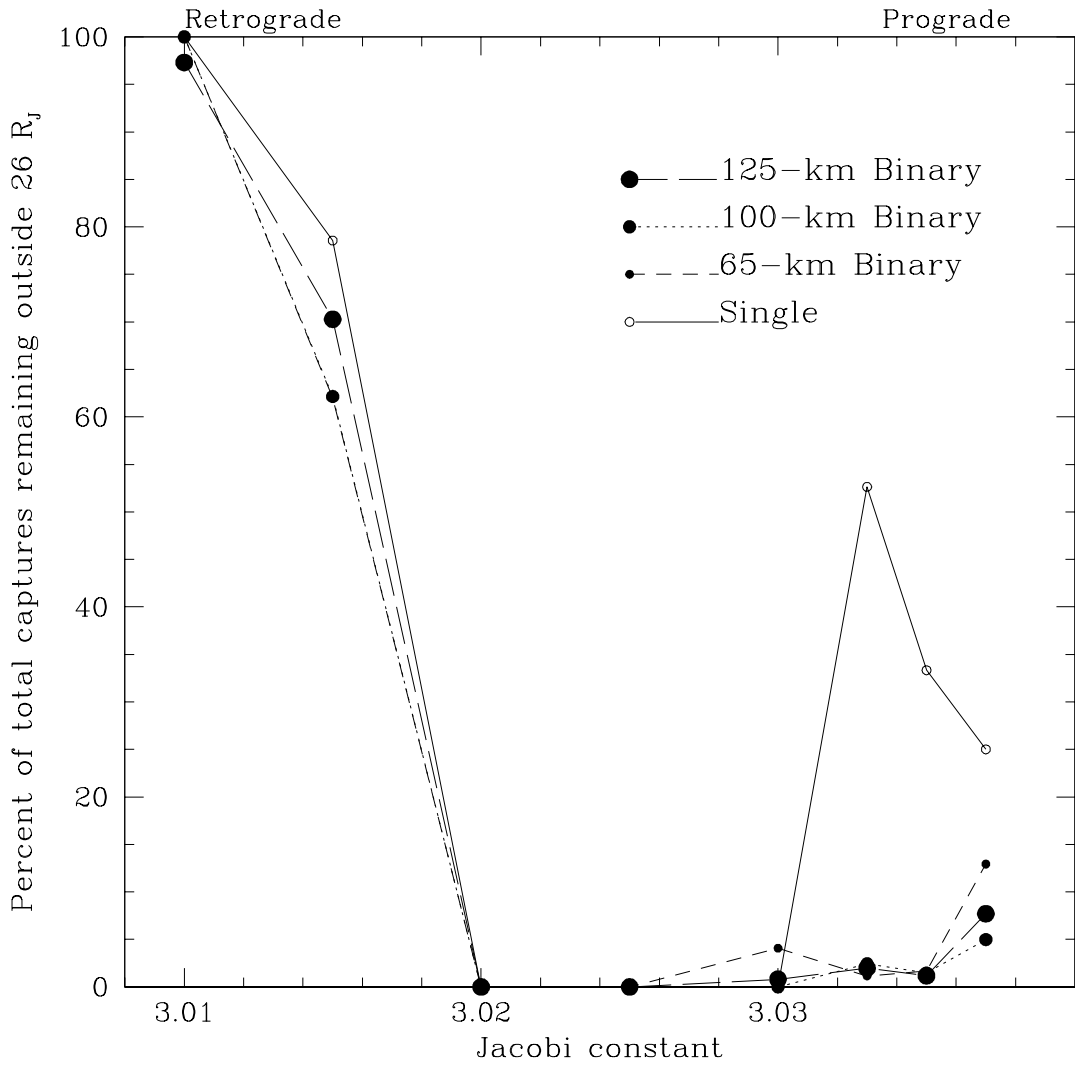


Figure 2.11 The percent of captured objects that do not cross interior to $26 R_J$ (Callisto’s semi-major axis) during the 1000-year integrations. The bodies were started on the Hill sphere. Compare with the entire set of captures seen in Fig. 2.7.

later in this section.

An interesting feature is the lack of any captures without close approaches for $C_J = 3.02$ and 3.025 . These Jacobi constants correspond to a distribution of orbital inclinations centered near 90° (see Section 2.4 and Fig. 2.5), where the Kozai effect is strongest. The Kozai mechanism causes the individual orbits to have large variations in both inclination and eccentricity, and thus they become subject to collision with

Jupiter or one of the Galilean satellites. This is the primary reason that no existing satellites in the Solar System have inclinations near 90° (see Figs. 1.2 and 1.4). The Kozai effect causes many of the captures in this C_J range to be lost.

All of the surviving binaries plotted here capture as 2C-BIN (though not all 2C-BIN captures are survivors), largely because of the separations we have studied. The separations of these binaries are optimized to give maximum capture percentages, leading to tidal disruption radii that are very close to Jupiter (Eq. 2.1). Thus these surviving binaries, which by definition have closest approaches outside Callisto, do not cross r_{td} and hence remain intact. The separations we have used, which are optimal for capture, are not optimal for survival. Somewhat larger separations would result in a higher percentage of surviving captures, with a lower percentage of overall captures.

The consequences of this are apparent in Fig. 2.11. For $C_J < 3.02$, the curves for single objects and all three binary masses are equivalent to within the error. This is because most of the binary captures in this C_J range are 2C-BIN. Since 2C-BIN captures act as a single entity with no alteration from tidal disruption, the captured population for $C_J < 3.02$ is similar to that of the single bodies and the fraction that avoid Callisto is also similar. While the surviving binaries for $C_J > 3.025$ are still all 2C-BIN, 1C captures dominate the 2C-BIN captures in this Jacobi constant range, but none of the 1C captures are safe from Callisto. Therefore, the percent of the total binary captures that survive at high Jacobi constants is very small.

Thus we find that while retrograde captures (low C_J) are rare (see Fig. 2.7), most of them are safe from collision with Callisto. On the contrary, prograde captures from binaries (high C_J) are numerous but prone to collision. This is bad news for binary capture—the largest enhancements occur for captures that are most likely to be removed by interactions with Callisto. As we have already discussed, examining

larger separations will lead to a larger percentage of capture orbits that are safe from collision. This may be a significant effect. How else can collisions be avoided?

One possible way out is if the captures occurred before Callisto was formed. At these early times, a dense accretion disk surrounded Jupiter, and the strong gas drag could have augmented capture rates (as in Pollack *et al.* 1979). However, this is not compelling, because satellites captured at this time would be prone to loss by orbital decay and later by collisions with forming proto-satellites.

The most likely mechanism for preventing captured bodies from colliding is gas drag from the remaining gas present outside Callisto's orbit at the time of capture. A small amount of gas is necessary for our mechanism in order to shrink capture orbits to their current sizes. In principle, this process can also increase the pericenters of the captured objects, causing them to avoid collision with Callisto. A typical collision timescale for a Callisto-crossing orbit with $a = 0.5r_H$ and $i = 10^\circ$ is on the order of 10^6 years, long enough for gas to evolve the satellites onto safe orbits (see Section 2.1). The timescale is longer for more-tilted orbits, but significantly shorter for retrograde orbits.

A tenuous gas around Jupiter and Saturn near the end of planet formation is consistent with our current understanding of planet formation (Section 2.1). If gas was present at the time of capture, its structure and density are not well constrained, and thus we do not focus on the orbital evolution process itself in this work. As a simple example, however, we simulated a drag force that acts against the velocity vector and show that it is able to both shrink the post-capture orbits and safeguard new satellites from collisions. This example is a worst-case scenario, as a drag of this form does not affect eccentricity, while a more realistic gas drag force will rapidly shrink eccentricities.

In Fig. 2.12, we plot the initial and final states for a prograde and retrograde

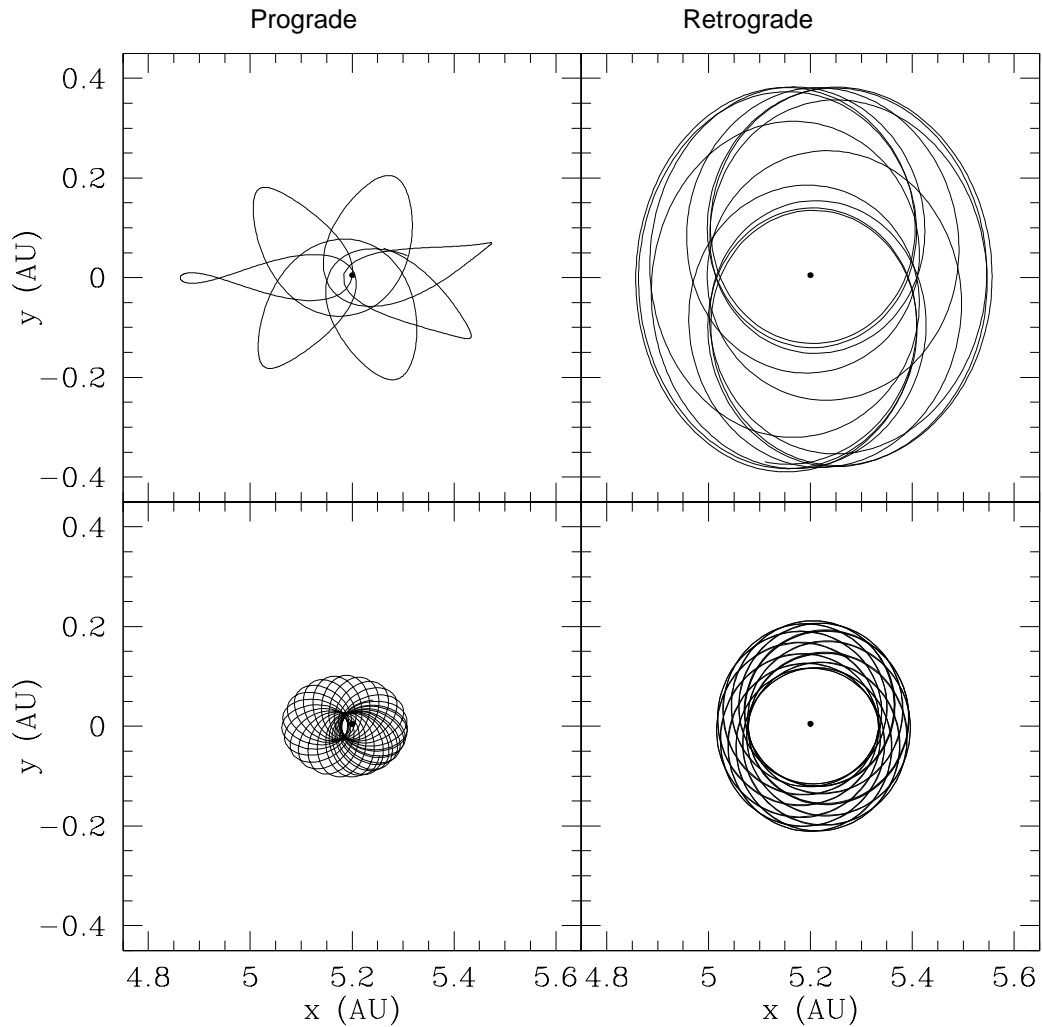


Figure 2.12 An example of a simple gas drag applied to a prograde (left panels; the same initial orbit as in Figs. 2.3 and 2.4) and a retrograde orbit (right panels). The orbits are shown immediately after capture in the upper panels, and the bottom panels show the orbits after 25,000 years of evolution. Jupiter is the dot in the center, and the Sun is to the left at (0,0). These orbits are the result of 1C capture from equal-mass binaries with 225-km components (prograde) and 65-km components (retrograde). Before disruption, the prograde binary had a separation of $65 R_B$ and a Jacobi constant of ~ 3.037 . The retrograde binary had an initial C_J of ~ 3.003 and was initially separated by $460 R_B$.

orbit in the presence of gas drag. The initial capture orbits are highly eccentric and extend out to or even beyond the Hill sphere. The gas drag is applied only after capture for simplicity; this is valid because the timescale for temporary capture is on the order of months, and the effects of the gas are negligible over such a short time. The final states are chosen so that the orbits lie approximately where the current progrades and retrogrades orbit at Jupiter (at $\sim \frac{1}{4}r_H$ and $\sim \frac{1}{2}r_H$, respectively), and they have pericenters outside Callisto's orbit, albeit just barely. The drag strengths were set so that the evolution for both orbits occurs over 25,000 years. However, with a more tenuous gas than in this example, the same evolution could take place on timescales 10–100 times longer. The binary capture mechanism discussed here constrains only the amount of orbital evolution, not the evolution rate, and hence avoids the satellite-loss problem of capture-by-gas-drag models.

In our simulations above (Fig. 2.12), we used an artificial drag force that does not raise pericenter. The amount by which true gas drag from a circumplanetary disk can raise pericenter depends on the details of two competing effects. First, since the gas is rotating at a near-Keplerian rate, eccentricities should damp significantly faster than semi-major axes, which tends to raise pericenter. But since the density of the disk should increase toward the planet, the effects of drag are more important near pericenter, which acts to oppose changes to the pericenter distance. How these two effects actually combine in the circumplanetary disk is complicated and very model-dependent. Accordingly, we restrict ourselves here to these qualitative arguments.

2.11 Discussion and conclusions

The new model discussed here, capture from low-mass binaries with subsequent orbital evolution, has both significant advantages as well as disadvantages in comparison to other suggested models.

One important advantage is that capture is viable at Jupiter, unlike three of the models discussed in Section 1.3. For example, Agnor and Hamilton's (2006b) direct three-body capture model works only for very large bodies in the gas giants' high-approach-speed environments. Also, the theory of Nesvorný *et al.* (2007) requires close approaches among the giant planets, of which Jupiter has very few in the Nice model scenario. In Vokrouhlický *et al.* (2008), the capture statistics from planet-binary encounters are low for all planets, but especially low for Jupiter and Saturn. This is primarily because of the high relative speeds assumed in their model. Though these latter two capture mechanisms in their current forms cannot explain the gas giants' irregular satellites, they are worth further study, perhaps in the context of altered versions of the Nice model or other early Solar System models.

Our model also has an important advantage over that of Pollack *et al.* (1979), in that our capture scenario allows for a much more tenuous gas disk, since the gas here is needed only for slowly shrinking the orbits, not for capturing satellites. Also, the gas in our model can persist for much longer than that in Pollack *et al.*, as a weaker gas does not have the problem of quickly destroying the captured bodies. Furthermore, various groups (e.g., Canup and Ward 2002) have proposed that the Galilean satellites formed from a tenuous gas; if true, the gas was most likely even thinner when the irregular satellites were captured. Thus it is important that our capture mechanism does not rely on a dense gas.

To directly compare our mechanism with that of Astakhov *et al.* (2003), we

need to consider both relative capture rates (and their survivability) and the prevalence of binaries vs. single bodies. In our simulations, we find that binary capture can provide a significant advantage over capturing from populations of single bodies for binaries with particular characteristics: high-enough masses ($\gtrsim 100$ km), optimal separations (~ 10 - $20 R_B$), and low incoming energies (corresponding to Jacobi constants $\gtrsim 3.02$ and mostly prograde encounters). However, like Astakhov *et al.* (2003), we also find that the probability that captured bodies (from either binaries or single bodies) avoid collisions with Callisto is low for readily captured progenitors. In Section 2.10, we discussed that this problem can be alleviated by altering the capture orbits with the surrounding gas or by capturing binaries with larger-than-optimal separations that do not lead to Callisto-crossing orbits.

So, how common were easily captured binaries early in Solar System history? This question is difficult to assess. Observational surveys of the current population of the cold, classical Kuiper belt (i.e., objects with modest inclinations and eccentricities) find a 30% binary fraction among bodies larger than 100 km (Noll *et al.* 2008), many with nearly equal-mass components. Also, recent studies of planetesimal formation have suggested that large, $\gtrsim 100$ -km bodies may form quickly in the gaseous proto-planetary disk, providing the building blocks of subsequent planet formation (Cuzzi *et al.* 2008; Johansen *et al.* 2007). Binary formation is likely to be contemporaneous with the formation of these bodies (Nesvorný 2008). Further, Morbidelli *et al.* (2009) have shown that the size-frequency distribution of asteroids in the main belt is consistent with large initial planetesimals, at least ~ 100 km in size. Together these results indicate that the ~ 100 -km binary objects considered here may have been quite common as the very last portions of the Solar System's gas disk were being depleted. In addition, perhaps the biggest boost to our model's production of viable satellites would come from considering 50- to 100-km satellites

of 200- to 500-km primaries. Such objects, while rarer, would capture far more frequently than those considered here.

Finally, the known irregular satellite population numbers ~ 100 , and many of these are probably members of families—thus, we need only produce at most a few dozen captures. While accounting for the origin of such a small population is difficult, our simulations show that it is likely binaries played a role. We conclude by offering our model as a new idea that alleviates many but not all of the problems faced by previous models, but acknowledge that without a detailed understanding of the initial planetesimal population, including binary statistics, a firm conclusion is not possible.

Chapter 3

Assessing Asteroids as Potential Satellite Sources

3.1 Introduction

In Chapter 2, we discussed capture from binaries approaching Jupiter on low-speed trajectories. Now we consider the source region of those bodies. While there are many possible source populations (e.g., Trojan asteroids, main belt asteroids, Jupiter-family comets, and Kuiper belt objects), this chapter is focused specifically on evaluating the Trojan asteroids and the asteroids of the outer main belt (including Hildas and Thules). Figure 3.1 shows the locations of these populations in today's Solar System. We begin by discussing our numerical studies of Trojan asteroids, and we consider Hildas and the outer asteroid belt in Section 3.5. We simulate the asteroids' escape from their orbits and examine the characteristics of their close approaches, comparing them to capture statistics from Chapter 2.

There are roughly as many Trojan asteroids as there are main belt asteroids (Yoshida and Nakamura 2005), and they librate around stable points in Jupiter's

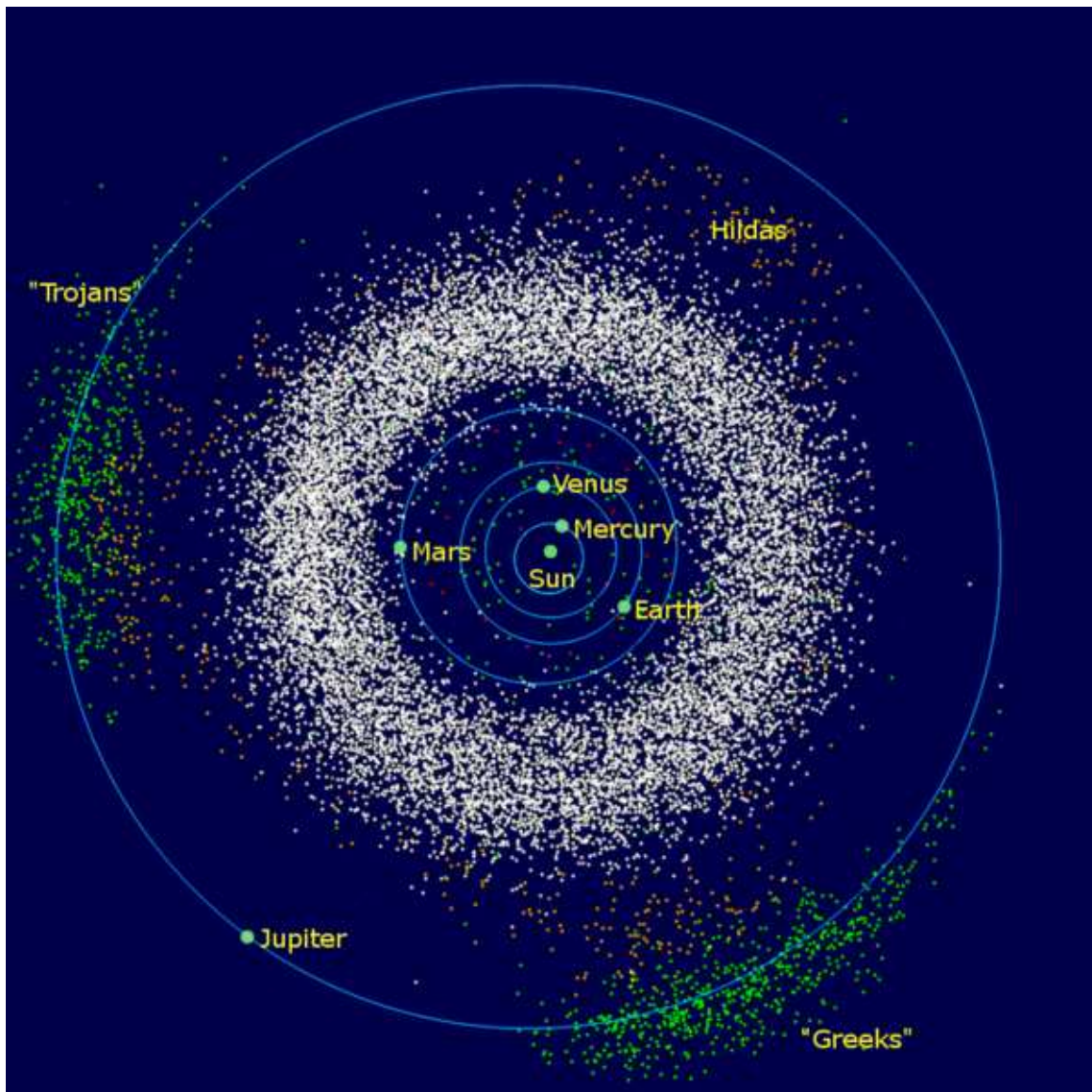


Figure 3.1 The inner Solar System, from the Sun to Jupiter. The white cloud of objects is the main asteroid belt, brown bodies are Hilda asteroids, and green dots represent the Trojan asteroids. The Trojan group ahead of Jupiter in its orbit are called Trojans, and the group trailing Jupiter are sometimes called Greeks; we call the entire group Trojans throughout this chapter. Data is from the Minor Planet Center (published on July 6, 2006), was plotted for Wikipedia, and represents the Solar System as it appeared on August 14, 2006.

orbit 60° ahead of and behind the planet. Although their orbits are extremely long-lived, it has been shown by Levison *et al.* (1997) that asteroids within the Trojan swarms have been leaking out over time. Currently, there are only two known binary Trojan asteroids (Marchis *et al.* 2006; Merline *et al.* 2001) (with two additional candidate contact Trojan binaries (Mann *et al.* 2007)), but it is estimated that binaries could account for up to 4% of the Trojans larger than 40 km (Marchis *et al.* 2003).

The Trojan asteroids we see today are in small-amplitude tadpole-shaped orbits around Jupiter's L_4 and L_5 Lagrange points (see Fig. 3.2). They orbit the Sun with the same period as Jupiter (about 12 years) and trace out their tadpole shapes relative to Jupiter over a period of about 150 years. The amplitude of their libration, D , is defined as the difference between the maximum and minimum angular separations of the Trojans from Jupiter. For the current Trojan population, values of D range between approximately 0° and 35° . The proper eccentricities (intrinsic eccentricity; i.e., the component not due to perturbations from Jupiter and the other planets), e_p , of today's Trojans range from about 0 to 0.15, and their orbital inclinations range from close to zero up to around 30° (Milani 1993).

When the Trojans have small libration amplitudes, keeping them close to the Lagrange points, their orbits are inherently stable over long timescales. However, very long-term effects, believed to be mainly secular perturbations from Saturn and the other giant planets (Marzari and Scholl 2002), can cause the Trojan orbits to become unstable. Levison *et al.* (1997) has shown that the timescale for instability depends on the Trojan's initial libration amplitude and proper eccentricity. The larger these two quantities, the sooner the orbit becomes unstable. In preparing for the current work, we have attempted to reproduce Levison *et al.*'s results, finding a) that the instability timescales we observed matched well overall with the values

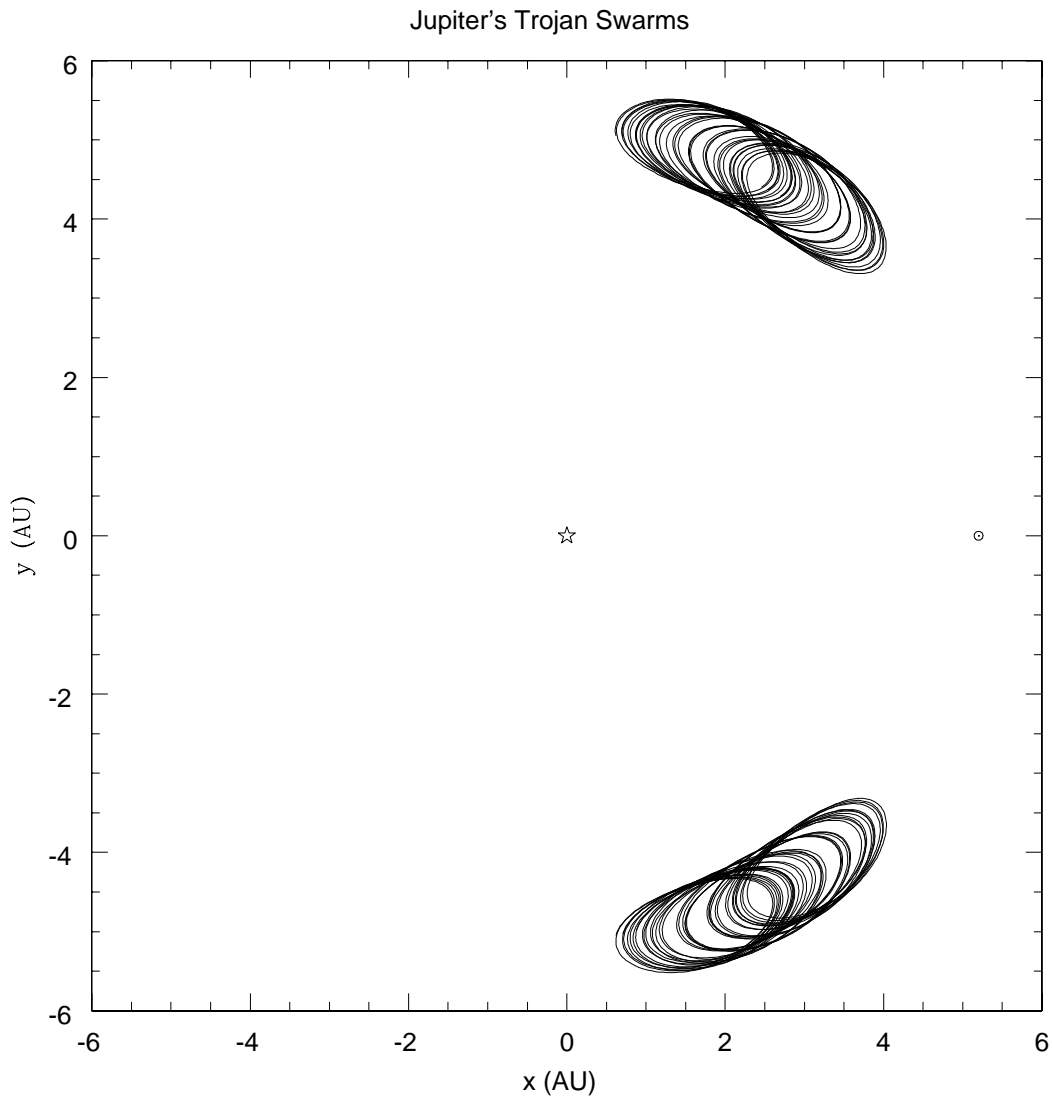


Figure 3.2 The Trojan asteroids librate around Jupiter's L_4 and L_5 Lagrange points. This plot shows tadpole-shaped orbits ($e = 0.1$, $D \approx 20^\circ$) in a frame rotating with Jupiter's angular velocity. The Sun is represented with a star, and Jupiter's location is marked with a circle. There are two observable Trojan periods here — 12 years (Jupiter's orbital period) to complete one small ellipse within its tadpole shape, and about 150 years to librate along its entire tadpole from its closest distance to Jupiter to its furthest and back again.

derived in Levison *et al.* (1997), b) that the inclusion of Saturn, Uranus, and Neptune in the simulations causes previously stable orbits to become unstable, and c) that the asteroids' inclinations, which were not included in the Levison *et al.* (1997) study, decrease their stability time. This last result is consistent with the findings of Marzari and Scholl (2002), who showed that the effects of the secular resonances with the giant planets become stronger with higher inclinations, more efficiently perturbing the Trojans toward instability.

When a Trojan becomes unstable, it typically undergoes a gradual increase in libration amplitude until its tadpole-shaped orbit grows into a horseshoe-shaped orbit. As the Trojan's larger range of motion causes it to come much closer to Jupiter, it receives stronger gravitational pulls from the giant planet. Eventually, the Trojan will leave its horseshoe orbit altogether. Figure 3.3 shows a typical escape trajectory.

Because the trajectories we are interested in involve multiple close approaches with Jupiter, they are very chaotic. Numerically, this means that any small error introduced in the particle's coordinates (e.g., round-off error) is magnified over time. If two simulations are identical except for a small change in the stepsize, for example, this can result in significantly different paths, especially later in the simulation. For this reason, it is necessary to interpret results statistically, with large populations of bodies (just as in Chapter 2).

Because all of the current Trojans are stable over $10^8 - 10^9$ year timescales, we cannot simply use their current orbital elements as our starting conditions, as following a large number of them until escape would be computationally expensive. Clearly, we do not know the distribution of initial conditions of the actual Trojans that had shorter lifetimes than the current bodies, as they have already escaped. However, we do have knowledge of the escape timescales for combinations of initial

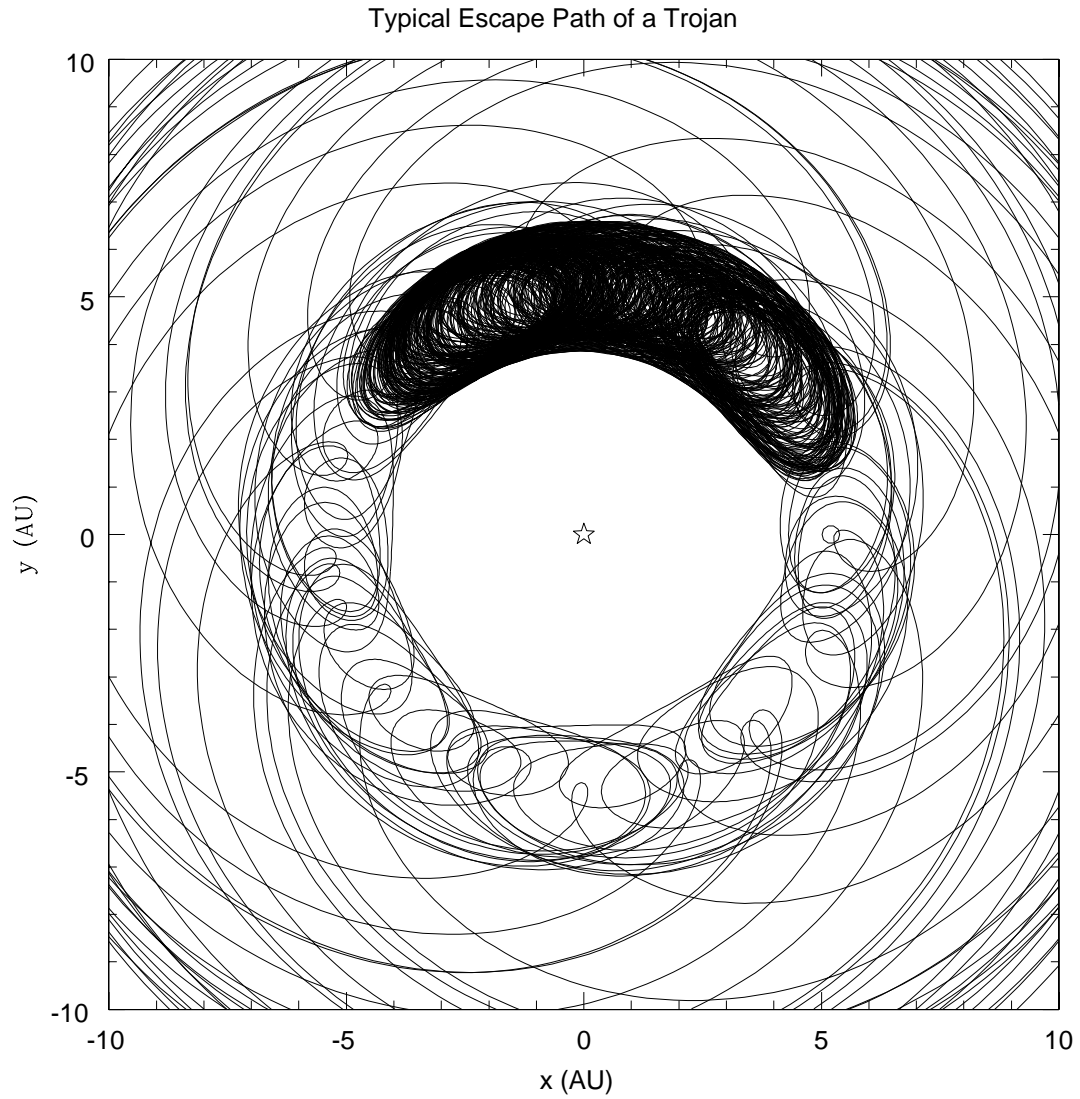


Figure 3.3 An example Trojan escape orbit plotted in a rotating reference frame. The initial tadpole (dark region) grows into a horseshoe orbit, until the asteroid suffers a fatal close approach to Jupiter, which kicks it out of the librating region. The central star is the Sun, and Jupiter is represented by the circle at (5.2, 0).

D and e_p (Levison *et al.* 1997), and thus we chose initial conditions that would produce a large number of escaping asteroids in a reasonable amount of simulation time. This effectively places the Trojans on large horseshoe orbits to begin with, so that their escape is imminent. We have performed many simulations of this type.

3.2 Numerical methods

For our numerical integrations, we used *HNBody*, a hierarchical N -body integration package (Rauch and Hamilton 2002), and *HNDrag*, used for applying non-gravitational forces to the particles and for detecting close approaches. In Sections 3.3 and 3.4, we used only the close approach detecting capabilities of *HNDrag*, with no application of drag forces. In Section 3.5, we explored simulations including a drag force to simulate the migration of Jupiter; the details are discussed therein.

As we discussed in Chapter 2, *HNBody* provides three main integrator options: symplectic, Bulirsch-Stoer, and Runge-Kutta. While symplectic integrators are generally more efficient for Solar System problems, they have two drawbacks for the current application. First, the symplectic integrator fails if a particle’s orbit becomes too highly perturbed, as when it suffers a close approach with Jupiter. To circumvent this problem, we can instruct *HNBody* to remove bodies for which $T + 2U > 0$, where T is the kinetic energy and U is the potential energy of the body with respect to the Sun. This corresponds to objects that attain more than two times Jupiter’s circular speed; i.e., greater than about 26 km/s (which happens interior to about $5 R_J$). Using this option prevents the symplectic integrations from failing during close approaches. Nonetheless, because the trajectory cannot be followed further, this is a shortcoming for the symplectic integrator.

The second drawback of the symplectic integrator is that unlike the Bulirsch-

Stoer and the Runge-Kutta methods, it has a fixed stepsize. For the other two integrators, a stepsize is determined internally at every timestep, so that large steps are taken when the trajectory is smoothly varying and smaller steps are taken elsewhere. These integrators automatically adapt their stepsizes to be as large as possible while still achieving the specified accuracy. (However, the Bulirsch-Stoer and Runge-Kutta integrators adjust the steps to be no larger than a user-specified stepsize so that data can be printed at the designated output interval.) To accurately resolve close approaches to Jupiter using the symplectic integrator, we found that we must specify a very small stepsize, which is used for the entire integration. This reduced stepsize offsets the natural speed advantage of the symplectic integrator for our application.

Table 3.1 presents the results of tests performed to determine the performance of different integrators on a typical simulation. For each run, we recorded the bodies' positions and velocities as a function of time. We compare the final coordinates for each integration. In Table 3.1, we see that the Bulirsch-Stoer results tend to converge to more decimal places than the other integrators for a given accuracy and stepsize. Also, increasing the specified accuracy improves convergence more than decreasing the maximum stepsize. A good compromise between integration speed and accuracy is the Bulirsch-Stoer accuracy 10^{-14} , stepsize 0.1 yr run; we chose these parameters for this work. From the last column of Table 3.1, it is clear that once close approaches occur, the resulting trajectories become quite different for different integrators or integration parameters. This illustrates the need for a large sample from which to draw statistics.

To obtain information about the close-approach distributions, we used *HNDrag*'s close-approach detector. This allowed us to record statistics for the closest approach of a given trajectory that came within a specified distance to Jupiter. *HNDrag*

Table 3.1. Integration parameter tests for Trojan asteroids

Integrator	Accuracy	Stepsize (yr)	CPU Integration Time (sec)	Object with No Close Approaches	Object with Many Close Approaches
Symplectic - 2nd order	-	0.03	79	5.184069046	-0.6398548077
Symplectic - 2nd order	-	0.01	212	5.665990796	-0.3566889686
Symplectic - 2nd order	-	0.005	446	5.791456085	121.3295024
Symplectic - 4th order	-	0.01	618	5.793823091	11.705359814
Runge-Kutta	10^{-13}	0.01	440	5.793855634	-13.15600778
Runge-Kutta	10^{-14}	0.01	792	5.793832615	-4.830651762
Bulirsch-Stoer	10^{-13}	0.05	207	5.793832353	-6.833081053
Bulirsch-Stoer	10^{-13}	0.01	663	5.793832532	102.7896755
Bulirsch-Stoer	10^{-14}	0.1	148	5.793832601	15.86355948
Bulirsch-Stoer	10^{-15}	0.01	879	5.793832794	1.925680765

Note. — The results of simulations comparing integrators. Each of these simulations was run with 100 Trojan asteroids, the Sun, and Jupiter for 20,000 years. The final y coordinate is given as an example of convergence; the other coordinates show similar convergence trends. Digits that agree with the most accurate simulation (Bulirsch-Stoer, accuracy 10^{-15}) are in boldface. The effects of chaos are clear in the last column (showing the final y coordinate of a different object), where the numbers vary widely after 20,000 years. The Runge-Kutta and Bulirsch-Stoer integrators, while adaptive-stepsize methods, will take steps that are no larger than a specified stepsize if one is given. This is for ease of comparison with the symplectic integrations.

monitored the bodies as they crossed the threshold; when they exited again, it noted position and velocity information for both the asteroid and Jupiter at the time of their closest encounter. This simplified our analysis by allowing us to select a large data output interval, thereby minimizing the size of our output files.

3.3 Trojans with an eccentric Jupiter

We begin by examining simulations including Trojan asteroids, the Sun, and Jupiter, including Jupiter’s actual eccentricity. Recall from Section 2.9 that the Jacobi constant is no longer valid in cases with an eccentric Jupiter. As we wished to use C_J to compare with binary capture statistics from Chapter 2, we performed additional simulations with Jupiter on a circular orbit; these are explored in Section 3.4. Nevertheless, the eccentric-Jupiter integrations led to several interesting results, and we discuss them here.

Each of these simulations follow 10,000 massless Trojan asteroids integrated for 20,000 years with initial e_p ’s between 0.160 and 0.169, and initial true longitudes (L) between 130° and 139° . The true longitude of Jupiter is set to zero, so the Trojan swarms in Fig. 3.2 have L near 60° (at L_4) and 300° (at L_5). Initial inclinations were set to a single value for all Trojans in a given simulation, the values varying from 0.1° to 10° for different simulations. Recall that these initial conditions were chosen because they allowed a large number of Trojans to escape in a short amount of time. Close approaches were defined as approaches within one Hill radius of Jupiter ($1 r_H \approx 0.36 \text{ AU} \approx 743 R_J$, where R_J , Jupiter’s radius, is about 0.0005 AU).

The top-left panel of Fig. 3.4 shows a differential distribution of close approach distance for a simulation with Trojan inclinations of 0.1° . The number per bin decreases linearly (though with a very gradual slope) from one Hill radius until

Close Approach Distances

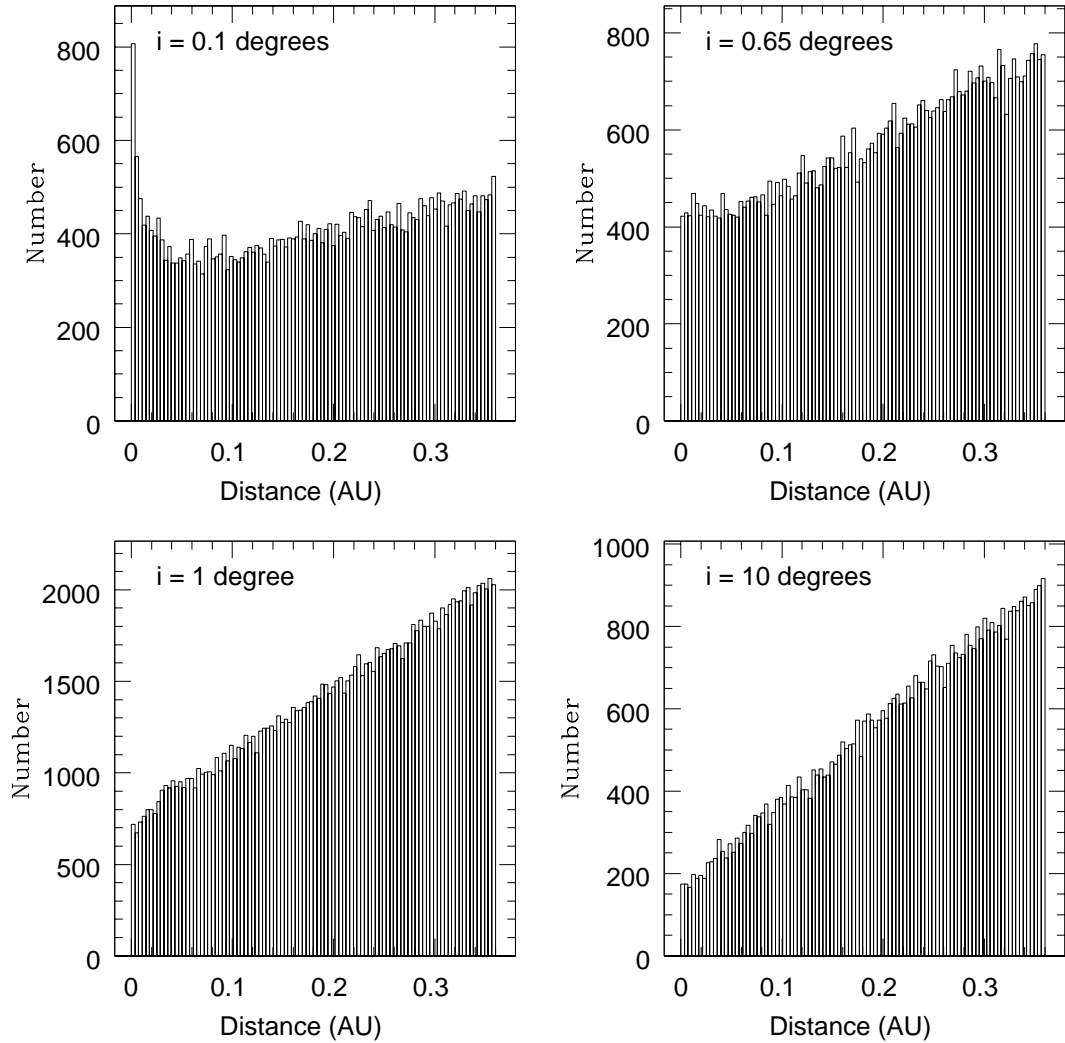


Figure 3.4 Differential distributions of close-approach distance to Jupiter for simulations of escaping Trojan asteroids. The four panels are labeled with the asteroids' initial inclinations. The total numbers of close approaches were $\sim 41,000$, $57,000$, $140,000$, and $54,000$ for $i = 0.1^\circ$, 0.65° , 1° , and 10° , respectively.

about 0.04 AU (near the orbit of Callisto), where it begins to rise again toward a sharp peak at very close distances.

We pursued several ideas for the cause of this peak. First, we performed multiple integrations with different initial conditions, keeping the inclinations constant at 0.1° . All of these showed the same sharp peak feature. Second, we examined the

possibility that these were sufficiently low-speed trajectories that the bodies had become temporarily bound around Jupiter (Hamilton and Burns 1991). Such temporary capture orbits would loop around Jupiter multiple times before departing the planet’s vicinity. Since we only record the closest approach within 0.36 AU, recorded distances for temporary captures would be substantially lower than for a single pass, thus artificially overpopulating the smaller-distance bins on the histogram. We tested this idea by decreasing our threshold close approach distance so that it would catch the close approaches for every pass of any temporarily bound objects. We reran the simulation with a number of close approach thresholds ranging from 0.01 AU to 0.50 AU and found that any approach that appeared in the record for a threshold smaller than 0.50 AU also appeared in the 0.50 AU record. As 0.50 AU is larger than Jupiter’s Hill radius, none of the approaching bodies had more than one pass by the planet, and we found no examples of temporarily bound orbits.

Another possibility we tested was that an inclination of 0.1° is low enough to be approximating a two-dimensional situation. The bottom-left panel of Fig. 3.4 shows the same distribution for a simulation with initial Trojan inclinations of 1° . Indeed, here the number per bin decreases linearly from one Hill radius to very close approach distances, with a much steeper slope than before and no inner peak.

We conclude, then, that the sharp peak is due to the small inclinations of the Trojans causing the simulation to be effectively two-dimensional. As we examine more inclination choices (Fig. 3.4), we see a clear progression from sharply peaked (0.1°) to flat (0.65°) to linear (1° and 10°). This supports our assertion.

We can also derive these trends analytically, in both the three-dimensional and two-dimensional limits. We consider straight-line trajectories approaching Jupiter with some range of impact parameter, b , and some resulting pericenter distance, r ,

determined by Jupiter's gravitational focusing. Figure 3.5 displays this geometry. For a three-dimensional problem, the range of impact parameters is described by a circle of radius b , and we wish to determine how this relates to the target area A around Jupiter. Using conservation of energy and angular momentum, we derive

$$A = \pi b^2 = \pi r^2 \left(1 + \frac{2GM_J}{v_\infty^2 r} \right), \quad (3.1)$$

where G is the gravitational constant, M_J is the mass of Jupiter, and v_∞ is the asteroids' speed far from Jupiter. Since v_∞ is a two-body construct and these simulations include three bodies, v_∞ can only be used in an approximate sense. Differentiating to find the change in area dA (effectively, the number of approaches) in rings of distance r from Jupiter and infinitesimal thickness dr ,

$$\frac{dA}{dr} = 2\pi r + \frac{2\pi GM_J}{v_\infty^2}. \quad (3.2)$$

If there were no gravitational focusing, one would expect a linear decrease towards zero close approaches at zero distance from Jupiter. However, Jupiter's focusing causes the second term in Eq. 3.2 and produces a non-zero intercept. Figure 3.4 shows the effects of both of these terms.

In the two-dimensional limit, the bodies approach in a single plane. Here, the range of impact parameters is projected from a circle to a line of width $2b$. Again, we use conservation laws to relate this to the range of the resulting close approaches:

$$l = 2b = 2\sqrt{r^2 + \frac{2GM_J r}{v_\infty^2}}. \quad (3.3)$$

Differentiating to get the change in area with close approach distance,

$$\frac{dl}{dr} = \frac{2r + \frac{2GM_J}{v_\infty^2}}{\sqrt{r^2 + \frac{2GM_J r}{v_\infty^2}}}. \quad (3.4)$$

Approach Geometry

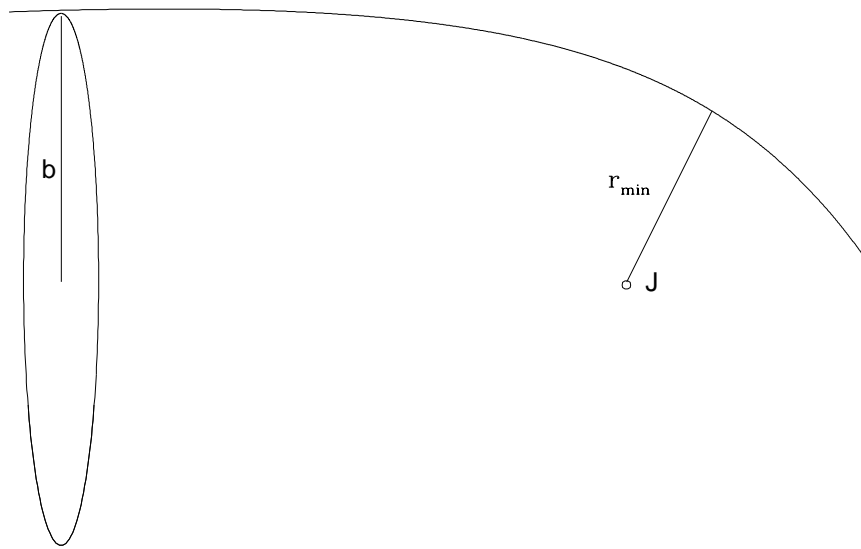


Figure 3.5 Schematic showing the geometry of approaching asteroids. The trajectories begin on a straight path (with impact parameter b) and are deflected by Jupiter's gravity as they approach the planet. For a three-dimensional simulation (as shown), the physical range of impact parameters is represented by a circle of radius b (seen from the side), and the actual approaches are distributed within a radius r_{min} circle around the planet ('J' = Jupiter).

For $r \ll \frac{2GM_J}{v_\infty^2}$, this expression reduces to

$$\frac{dl}{dr} \sim \sqrt{\frac{2GM_J}{v_\infty^2} \frac{1}{r}} \quad (3.5)$$

and explains the sharp inner peak that we see in the 0.1° approach distance distribution (Fig. 3.4). These derivations are only illustrative, as our distributions represent not a constant v_∞ but a range of values, and even the low-inclination scenarios are not truly two-dimensional. Equation 3.4 predicts that the number of approaches from a flattened Trojan distribution should decrease for increasing r , and instead we see it increase slightly (Fig. 3.4). This may be due to a superposition of two-dimensional and three-dimensional effects.

We find, then, that to avoid artifacts from flat distributions, future simulations must be performed with integrations set at 1° or higher.

3.4 Trojans with a non-eccentric Jupiter

We now discuss similar simulations of 10,000 Trojans except with Jupiter on a circular orbit, allowing for calculation of the Jacobi constant for the escaped Trojans. Here, we set all initial Trojan inclinations to 1° and varied the combination of initial e_p and L values. We followed the bodies for 40,000 years so that almost all of the asteroids escaped.

Figure 3.6 shows the distribution of C_J values of the first approach of each escaped Trojan (9974 of 10,000 escaped). In this simulation, the initial conditions are evenly spread over a range of e_p : 0.04-0.08 and L : 150° - 159° . The resulting Jacobi constants are dictated by the initial conditions and tightly confined between $C_J \approx 2.984$ and $C_J \approx 2.993$.

Comparing with capture statistics from Chapter 2, these Trojans' C_J values

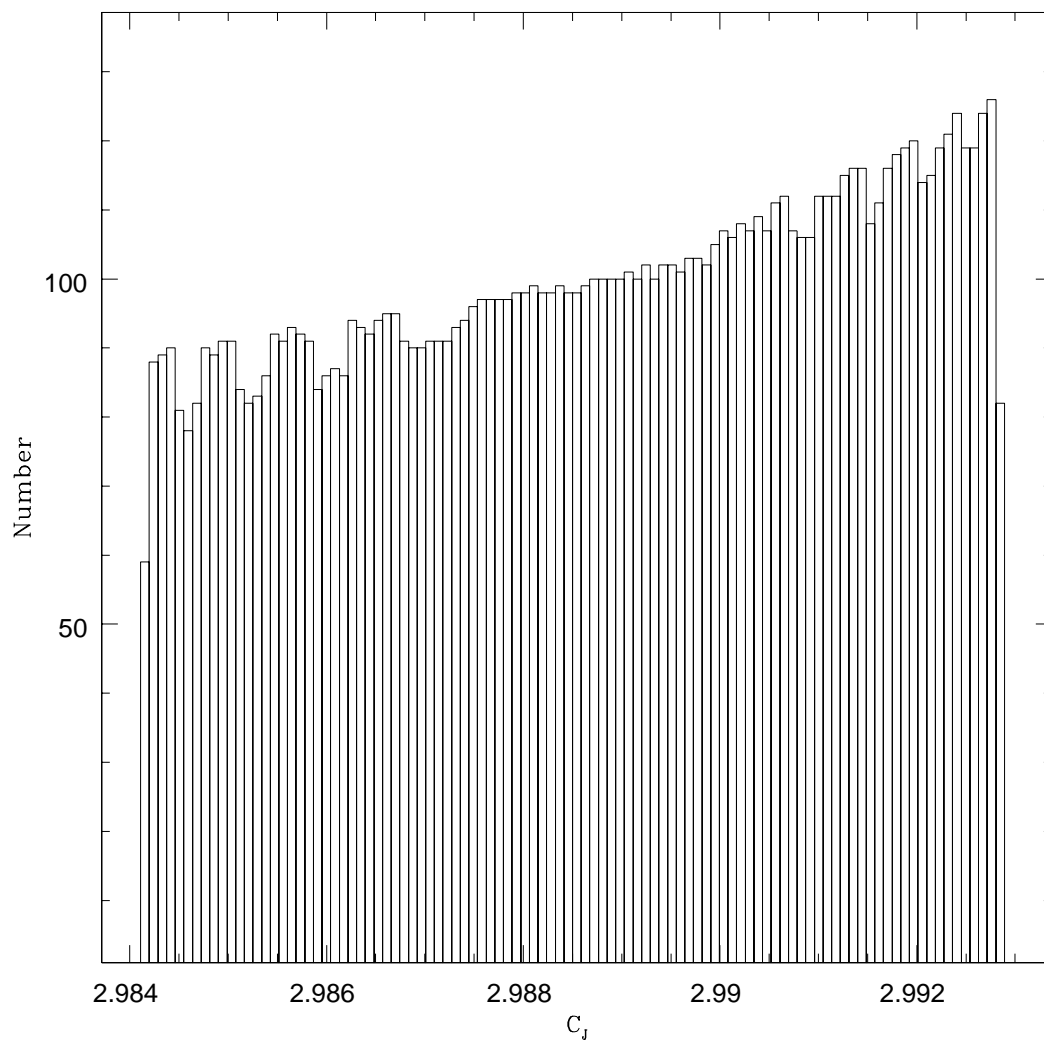


Figure 3.6 Jacobi constants for the first close approach of each escaped Trojan to Jupiter. Initial e_p ranged from 0.04-0.08 and L from 150° - 159° . Almost all of the Trojans escaped.

Table 3.2. Jacobi constants of escaped Trojan asteroids

Initial e_p	Initial L	C_J
0.0	160°-169°	2.99830 - 2.99838
0.04-0.08	150°-159°	2.98411 - 2.99289
0.20-0.24	140°-149°	2.91576 - 2.93820
0.26-0.30	60°-70°	2.87418 - 2.90197

Note. — Resulting ranges of C_J for escaped Trojan asteroids with the given initial e_p and L values. Trojans in each simulation diffused on approximately the same timescale ($\sim 10^4$ years) and in all four simulations, over 97% of the Trojans escaped by 4×10^4 years. Approach speeds (v_{L_1}) range from 2.6 km/s for the highest C_J (2.99838) to 5.3 km/s for the lowest C_J (2.87418).

would result in near-zero capture probability (see, e.g., Section 2.6) if approaching the planet as a single body or part of a ~ 100 -km binary. Larger masses would increase the capture rate, but we are interested in assessing capture probabilities for the more-numerous small bodies. The chief reason for the low capture probability is that the bodies' encounter speeds ($v_{L_1} = \sqrt{C_{J,crit} - C_J} \approx 2.9$ km/s) are too fast. To be permanently captured, the asteroids would need to approach with $v \sim 0.5$ km/s.

We examined other initial conditions with about the same Trojan diffusion timescales ($\sim 10^4$ years) and achieved similar results. Summarizing, the ranges of C_J values for four choices of e_p and L are given in Table 3.2.

Thus we conclude that escaping Trojan asteroids are not a viable source of captured satellites at Jupiter. Neither long-lived temporary captures nor permanent captures from binary disruption are likely to have resulted from the Trojan population. Finally, we note that if any captures did occur, they would have produced

retrograde satellites (Fig. 2.5).

3.5 Escape from the outer asteroid belt

We now consider the outer asteroid belt, including the Hilda and Thule asteroids, as a source region for irregular satellites. Hildas are located between 3.8-4.1 AU, with eccentricities up to 0.35 and inclinations up to 20° (Brož and Vokrouhlický 2008). They orbit in the 3:2 mean-motion resonance with Jupiter, avoiding conjunctions with the planet (see Fig 3.1). There are almost 1200 known Hilda asteroids, and they are the closest large asteroid grouping to Jupiter besides the co-orbital Trojans (Brož and Vokrouhlický 2008). Thule asteroids are rarer with just three known objects. They orbit in Jupiter’s 4:3 resonance near 4.28 AU (Brož and Vokrouhlický 2008).

To simulate the escape of Hildas and other asteroids in the outer main belt, we modeled Jupiter’s inward migration due to the formation of the Oort cloud, which is predicted by most Solar System evolution models (e.g., Tsiganis *et al.* 2005). These integrations include the Sun, Jupiter and 10,000 massless asteroids with a ranging from 3.8–4.8 AU, e from 0–0.1, and $i=1^\circ$. Jupiter is modeled on a circular orbit with a drag force applied against its velocity, moving the planet from 5.5 to 5.2 AU in 10^5 years. This timescale is fast compared to the secular interactions between Jupiter and Saturn (which cause oscillation in the planets’ e and i) as well as the precession of asteroid orbits due to Jupiter, both of which happen with timescales of $10^4 - 10^5$ years. However, the overall results should change only slightly with slower migration rates.

To distinguish intrinsically unstable orbits from those driven to instability by Jupiter’s migration, we also ran an identical simulation with no migration, placing

Jupiter in orbit at 5.5 AU. In the simulation with migration, 3023 of 10,000 bodies escaped the asteroid belt over 10^5 years. For the no-migration run, 1882 of 10,000 bodies escaped, and, as expected, almost all (98%) of these same bodies also escaped in the migration case.

We first examine the semi-major axes from which these bodies escape. Figure 3.7 shows the initial semi-major axes of escapees in both the migration and no-migration scenarios. In both plots, we see two distinct populations with a gap in between. We label the two escaping populations the Inner and Outer asteroid groups for comparison with later plots. With 100 bodies initially populating each bin, we see that almost all asteroids escape for both Outer groups (at ~ 4.65 -4.8 AU). This indicates that regardless of migration, the outer regions of our semi-major axis range are unstable. The gap in the middle of the two populations is the location of the 4:3 resonance with Jupiter, where the three known Thule asteroids currently reside (Brož and Vokrouhlický 2008). Note that in the no-migration case, these bodies are stable, but with migration, some of these bodies escape. We examined the orbital elements for several asteroids near 4.6 AU and saw that, in fact, Jupiter’s migration in the resonance is slowly driving up their eccentricities, rendering them unstable. For the migration case, Jupiter’s inward motion causes almost all Inner bodies with a between 4.33 and 4.48 to escape. Interior to 4.33 AU, the bodies do not escape because they have not experienced the destabilizing effects of Jupiter for sufficiently long times. In the no-migration simulation, the escape rate increases monotonically from $a=4.34$ to $a=4.45$ as the closer bodies feel Jupiter’s gravity more strongly.

We now consider the contribution of the Inner and Outer populations to the Jacobi constant distributions for both simulations. The top panels of Fig. 3.8 show the Jacobi constants for each body’s first approach within Jupiter’s Hill sphere. For the simulation with migration, the Jacobi constant was calculated using Jupiter’s

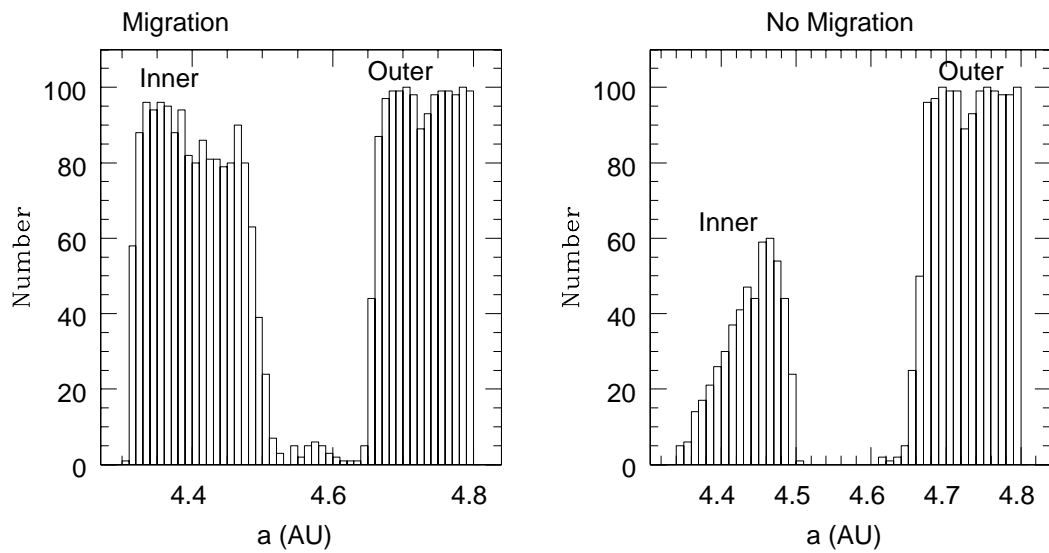


Figure 3.7 Distribution of initial semi-major axes of the escaped outer-main belt asteroids. The left panel shows results of a simulation with Jupiter migrating inward from 5.5-5.2 AU. The right panel shows results of an otherwise identical simulation with no migration and Jupiter orbiting at 5.5 AU. For both simulations, the asteroids' initial a was between 3.8-4.8 AU, with e ranging from 0-0.1 and $i = 1^\circ$. In the migration case, there were a few (unplotted) escapees with a near 4.05 AU. Almost all of the escaping bodies for the no-migration simulation also escaped in the run including migration. The labels Inner and Outer allow for comparison with Fig. 3.8.

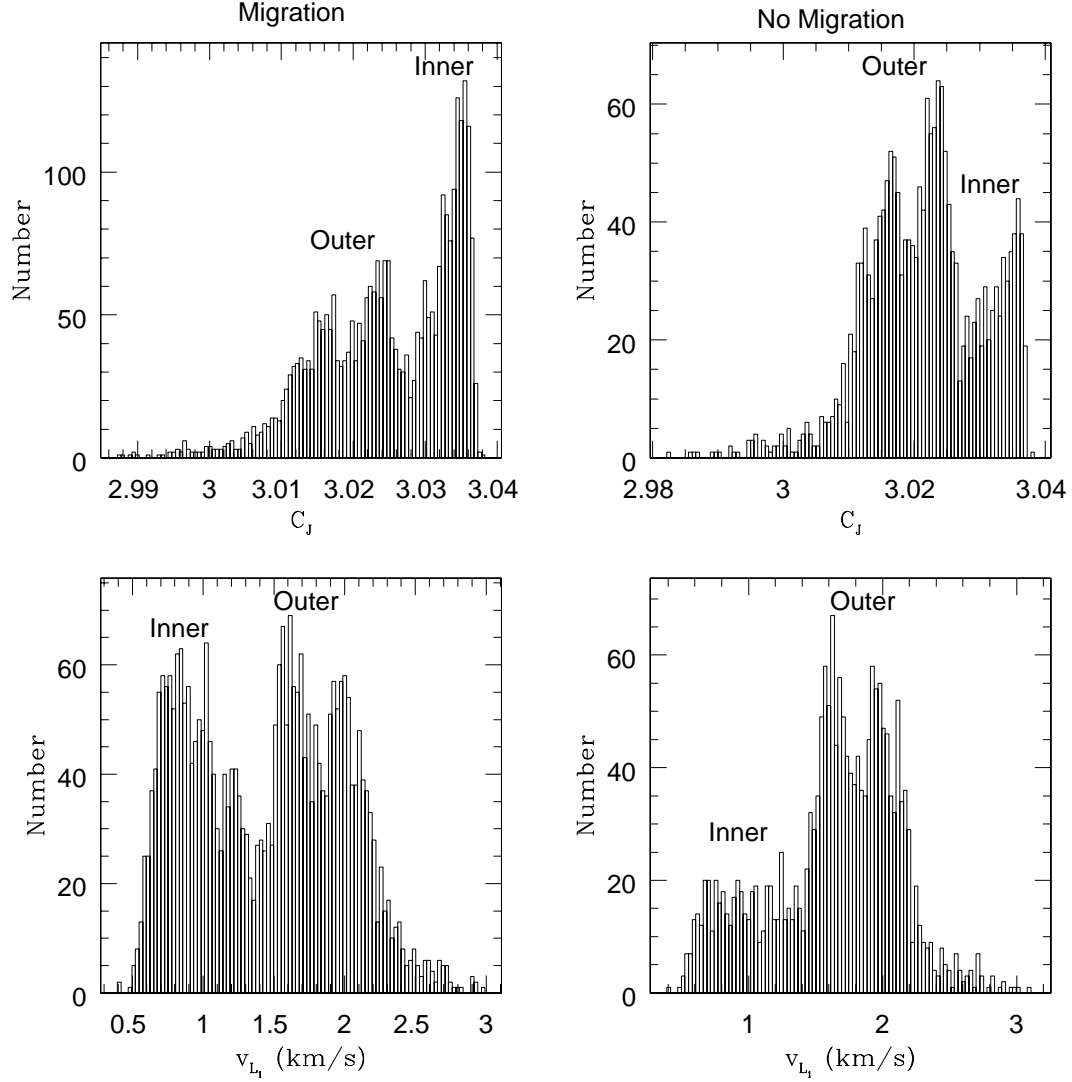


Figure 3.8 Jacobi constants and corresponding speeds at L_1 for the first close approach of each escaped asteroid in the migration case (left two panels) and no-migration case (right two panels). The two cases are detailed in Fig. 3.7. Each panel is divided into 100 bins.

instantaneous orbit at the time of close approach. Since the migration causes a small eccentricity for Jupiter (~ 0.0002), there are small errors in the calculated C_J values for this simulation. The bottom panels show the corresponding v_{L_1} distribution for each of the two integrations.

From Fig. 3.8, we see again the two distinct populations. By examining the

bodies' initial a , we have determined that in both simulations, the unstable Outer asteroid groups have systematically lower Jacobi constants (and faster approach speeds) than the Inner groups. For the Inner group, the resulting Jacobi constants are quite high in both cases, centered near $C_J = 3.033$. Recall from Chapter 2 that $C_{J,crit} \approx 3.0387$. In addition, we determined in Chapter 2 that these high Jacobi constants correspond to high capture probabilities for binaries with the right initial conditions. For example, pairs of bodies crossing into the Hill sphere, each with radius 125 km and separated by ~ 1200 km, lead to capture at a rate of $\sim 4\%$ for $C_J = 3.033$ (Fig. 2.7). These captures are primarily to prograde orbits. The Outer asteroid groups, on the other hand, have wide ranges of Jacobi constants centered near 3.02, which corresponds with a capture percentage near 1% for the same binary characteristics. However, $C_J = 3.02$ also corresponds to inclinations near 90° (Fig. 2.5) and loss due to the Kozai mechanism. Thus most captures from the Outer asteroid group would not survive. Those that survive could result in either prograde or retrograde orbits.

We conclude that asteroids escaping because of orbital instability in the early Solar System or because of Jupiter's later inward migration are both likely to have captured at Jupiter, especially if they originated interior to the 4:3 resonance. Both simulations suggest that the main asteroid belt is a far better source for Jovian satellites than the Trojan region. The main difference in the distributions for the two cases (migration or no-migration) is that a significantly higher fraction of Inner asteroids escape when Jupiter migrates (Figs. 3.7 and 3.8). However, the actual numbers escaping during these periods in Solar System history is unknown. In addition, other mechanisms can cause destabilization; e.g., Yarkovsky drag can move small, km-sized asteroids. One caveat, discussed in Chapter 2, is that binary capture results in highly extended orbits requiring orbital dissipation, and thus captures

must have occurred while some circumplanetary gas existed in order to be viable.

Finally, we examined the distribution of close-approach distances, shown for the migration scenario in Fig. 3.9 (with a similar distribution for the no-migration case). With their high C_J values, these bodies' zero-velocity curves are almost closed around the planet (see Fig. 2.2). For such low-speed approaches, the asteroids fall in very close to the planet. In addition, we performed the same test described in Section 3.3 to search for temporary captures and found that many of these asteroids stay near the planet for multiple orbits. Such orbits are characteristic of high Jacobi constants (e.g., see Fig. 2.4). Since only the closest of these approaches is recorded, temporary-capture orbits strongly enhance the peak near Jupiter.

3.6 Conclusions

The first portion of this chapter was focused on understanding the orbit parameters of escaped Trojan asteroids. We confirmed that for a sufficiently three-dimensional simulation, the number of close approaches at a given distance decreases linearly from the edge of the Hill sphere towards the planet, and is non-zero at zero distance from Jupiter. This result guided our inclination choice in later integrations. In Section 3.4, we saw that Jacobi constants for escaped Trojans were below 3.0, corresponding with near-zero capture probabilities. Thus the Trojans are not a likely source of captured satellites at Jupiter. If capture did occur from the Trojans, it would deliver the asteroids to retrograde orbits.

In Section 3.5, we explored capture from escaping outer main belt asteroids. We found that, for asteroids interior to the 4:3 resonance, Jacobi constants are ~ 3.033 , corresponding to some of the highest capture rates we saw in Chapter 2. This means that binaries from this population with the right characteristics could

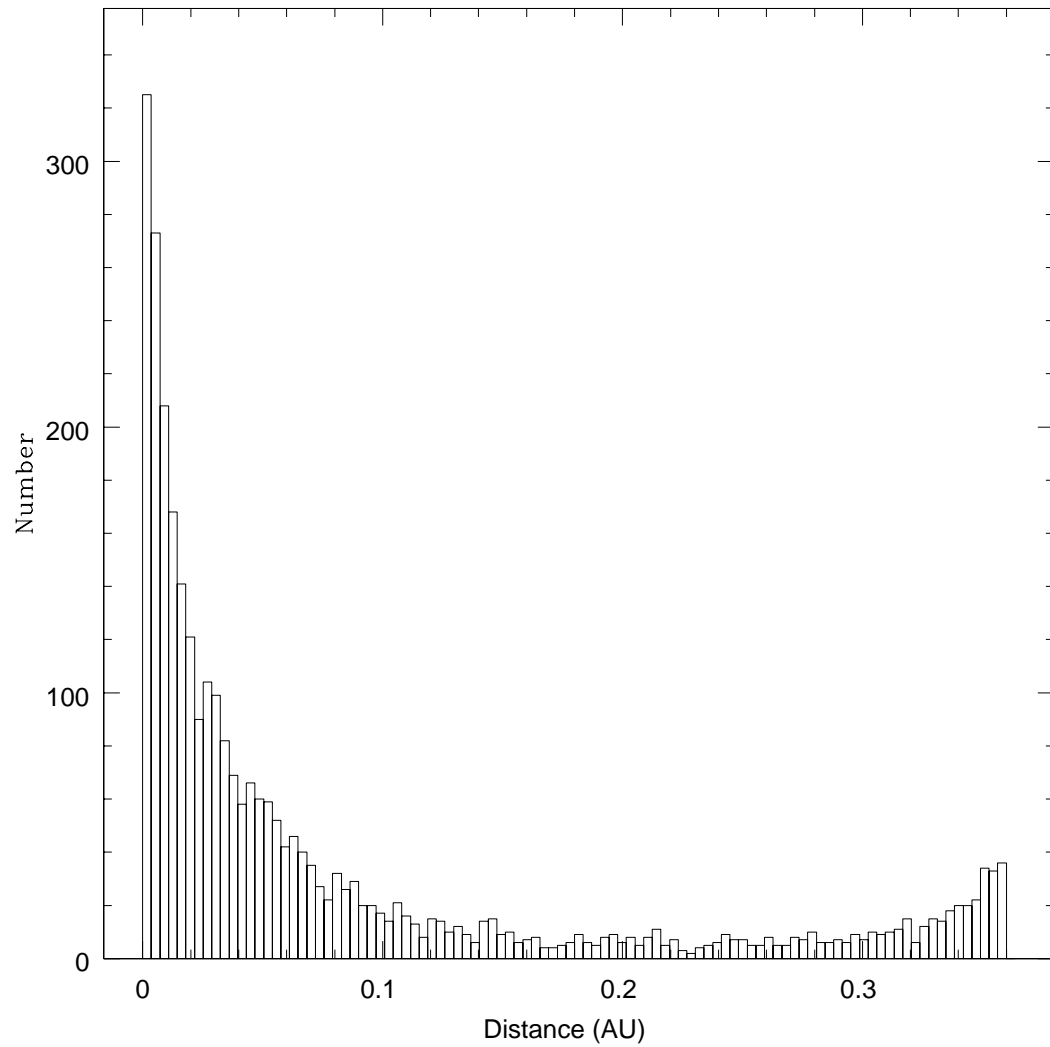


Figure 3.9 Close-approach distribution for first close approaches of outer main belt asteroids, plotted for the migration case (but similar for no migration). Close approaches are defined as crossing into the Hill sphere.

capture to primarily prograde orbits as often as a few percent of the time. Bodies originating exterior to the 4:3 resonance have C_J centered near 3.02 and would capture more efficiently than Trojans, to either prograde or retrograde orbits. However, the average inclination for these asteroids is high, so most captures from this group would not survive.

The main belt has been significantly thinned out over time (by a factor of hundreds or thousands in mass; e.g., Weidenschilling (1977); Wetherill (1989)), and almost all of the escaping asteroids likely approached Jupiter. We conclude that asteroids from the main belt, especially those interior to Jupiter's 4:3 resonance, are promising sources for the binary capture mechanism detailed in Chapter 2.

Chapter 4

Galilean Satellites: Background

4.1 Physical properties

Jupiter's four largest satellites have been objects of fascination since their discovery by Galileo Galilei in 1610. Shortly after his discovery, Galileo realized that the four point sources hovering near Jupiter were in fact moons orbiting the planet. This added support for the Copernican Sun-centered view of the Solar System: if moons orbited Jupiter, then the Earth was not the center of motion for all Solar System bodies.

The Galilean satellites have been at the center of several milestones in science. In 1676, Ole Romer used observations of these bodies to measure the speed of light. He did this by studying eclipses of the moons by Jupiter's shadow and noticing a difference in the observed and predicted eclipse times. He correctly assumed this difference existed because it takes time for light to travel, and he used the data to calculate an approximate value of the speed of light.

The timing of the Galilean satellites' eclipses was also used to determine longitude on Earth. Observers in two locations could note the moment a moon was eclipsed and calculate the difference in local (solar) times, enabling the calculation

Table 4.1. Galilean satellites: physical data

Satellite	M (10^{22} kg)	R (km)	ρ (g/cm ³)
Io	8.93	1821	3.5
Europa	4.80	1560	3.0
Ganymede	14.8	2631	1.9
Callisto	10.8	2410	1.8

Note. — Physical characteristics of the Galilean satellites: mass (M), mean radius (R), and density (ρ). Mass data is from Beatty *et al.* (1999) and radius and density are from JPL’s Solar System Dynamics website, http://ssd.jpl.nasa.gov/?sat_phys_par.

of longitude.

Since discovery, our knowledge of the Galilean satellites has evolved greatly, and the increase in understanding has accelerated in the past 35 years with the advent of flyby and later orbiting spacecraft, including Pioneer 10 and 11, Voyager 1 and 2, Galileo, Cassini, and New Horizons. Ground-based and Earth-orbit telescopes have also made significant contributions.

Table 4.1 gives the mass, radius, and density of each satellite, and Fig. 4.1 shows Galileo spacecraft images of the satellites in order of their distance from Jupiter. The least-massive Galilean satellite, Europa, is slightly smaller than Earth’s Moon, and the largest, Ganymede, is the biggest moon in the Solar System. Although it is slightly larger than Mercury, Ganymede is less than half as massive as that iron-dominated planet.

The innermost satellite, Io, is the most volcanic body in the Solar System. The existence of current volcanism was predicted by Peale *et al.* (1979) just one week before Voyager 1’s cameras spotted an active plume along Io’s limb (Johnson 1999). Io’s surface is covered with volcanic pits, calderas, and lava flows, activated by its



Figure 4.1 A composite view of the four Galilean satellites of Jupiter, as imaged by the Galileo spacecraft. The satellites are shown to scale, in order of their orbital distance from Jupiter; from closest to farthest (left to right): Io, Europa, Ganymede, and Callisto. Credit: NASA/JPL/DLR.

constant tidal flexing from Jupiter. The volcanoes are powered by high-temperature liquid silicates (> 1500 K; Johnson (2004)), emit mainly sulfur dioxide, and resurface Io at a swift rate of 1–10 cm/yr (de Pater and Lissauer 2001). Not surprisingly, no impact craters have been found on the moon (de Pater and Lissauer 2001). Galileo's gravity-field data indicated that Io is highly differentiated, with an iron-rich core out to about half the satellite's radius topped by a partially molten silicate mantle and a thin silicate crust (Johnson 2004).

The outer three Galilean satellites consist of both rock and ice. Europa's very bright surface is made of nearly pure water ice. The satellite is also extremely flat with no topological features higher than 300 m (de Pater and Lissauer 2001) and very few craters. Europa is covered with ice cracks and ridges as well as features resembling ice flows, all of which hint at a subsurface liquid ocean. It is believed that the ridges form either from compression of two ice plates or expansion, in which liquid water rises up through the resulting crack to make the ridge. The existence of one form of tectonism, of course, implies that the other is also active elsewhere on the moon. The outer ice/water layer on Europa is thought to be 75–150 km

thick, with a solid silicate mantle below and a dense iron/rock core (Johnson 2004). Galileo's magnetometer also found that perturbations in Jupiter's magnetic field near Europa (as well as near Ganymede and Callisto) are consistent with a salty, conductive ocean. The presence of a liquid ocean at Europa is widely accepted, but the thickness of the overlaying ice (a key parameter for any drilling-based Europa space mission) is debated and estimated to be anywhere from less than a kilometer (Greenberg *et al.* 2002) to greater than 20 km (Pappalardo *et al.* 1999).

Perhaps Ganymede's most impressive attribute is its intrinsic magnetic field, detected by the Galileo spacecraft. An explanation for its origin, however, is still elusive. Earth's magnetic field requires a conductive, convective molten fluid, which Ganymede may have in its core, but models indicate that maintaining core convection in Ganymede to the present day would have been difficult (Johnson 2004). The surface of Ganymede consists of large stretches of both bright and dark material. The heavily cratered dark regions appear to be the oldest areas, while the light terrain consists of parallel grooves formed by tectonic activity. Ganymede is highly differentiated, and models of the interior structure suggest a molten core, a silicate mantle, and a thick outer ice shell, with a possible liquid water layer.

Callisto's surface is uniformly dark except for bright marks from its numerous craters. The Galileo spacecraft's high-resolution images of the satellite showed a surprising lack of small craters. This may be due to surface degradation produced by sublimation of volatile materials (de Pater and Lissauer 2001). In contrast to the other three Galilean satellites, Callisto's interior is only partially differentiated, with no well-defined large mantle or core. This indicates a lack of significant heating for Callisto. Recently, Barr and Canup (2010) proposed that the difference in heating between Ganymede and Callisto is due to different impact frequencies during the late heavy bombardment. A simpler explanation for an undifferentiated Callisto

may be that Ganymede’s heating comes from its resonance with Io and Europa (Malhotra 1991; Showman and Malhotra 1997; Showman *et al.* 1997).

4.2 Orbital properties and resonances

The focus of the following chapter is the origin of the Galilean satellites’ Laplace resonance. In this section, we describe some of the basics of resonance theory, as well as the effects of oblateness and tides, with emphasis on results relevant to later sections.

An orbit is fully defined by six orbital elements. One commonly used set of elements includes semi-major axis (a), eccentricity (e), inclination (i), longitude of the ascending node (Ω), argument of pericenter (w), and mean anomaly (M). The semi-major axis, a , can be rewritten as orbital mean motion, n , which is the average angular speed of the satellite:

$$n = \sqrt{\frac{G(M_P + M_s)}{a^3}}, \quad (4.1)$$

where M_P is the planet’s mass, M_s is the satellite’s mass, and G is the gravitational constant. The orbital period P , then, is simply $2\pi/n$. Table 4.2 gives all of these values for the present-day Galilean satellites.

The mean longitude, $\lambda = \Omega + (\omega + M)$, can be used as a substitute for the mean anomaly, M , and it is customary to do so in a discussion of resonances. Mean longitude is a bent angle measured in two planes: it equals the angle from the reference direction to the node measured in the reference plane (Ω) plus the angle from the node to the satellite’s average location measured in the orbital plane ($\omega + M$), calculated as if the planet moved at a constant angular rate. The mean longitude increases linearly in time and $d\lambda/dt \approx n$. In addition, the longitude of

Table 4.2. Galilean satellites: orbital data

Satellite	a (R_J)	e	i (deg)	Ω (deg)	w (deg)	M (deg)	n (deg/day)	P (days)
Io	5.89716	0.0041	0.036	43.977	84.129	342.021	203.4889583	1.769
Europa	9.38427	0.0094	0.466	219.106	88.970	171.016	101.3747242	3.551
Ganymede	14.96671	0.0013	0.177	63.552	192.417	317.540	50.3176072	7.155
Callisto	26.33861	0.0074	0.192	298.848	52.643	181.408	21.5710728	16.69

Note. — Mean orbital elements of the present-day Galilean satellites as measured from the local Laplace plane: semi-major axis (a), eccentricity (e), inclination (i), longitude of the ascending node (Ω), argument of pericenter (w), mean anomaly (M), mean motion (n), and orbital period (P). Mean anomaly is given for the epoch of January 16, 1997, 0.0 hours Terrestrial Time. Data are from JPL’s Solar System Dynamics webpage, http://ssd.jpl.nasa.gov/?sat_elem, and were produced by R. A. Jacobson.

pericenter $\tilde{\omega} = \Omega + \omega$ can be used instead of ω . Longitude of pericenter is also a bent angle, measured both in the reference and orbital planes.

A mean-motion resonance occurs when the ratio of the orbital periods of two bodies is rational, causing the effects of mutual perturbations to build up over time. Gravitational perturbations on a body, including resonances, can be described with the disturbing function, which can be written with orbital elements as a series of cosine terms:

$$\mathcal{R} = \sum_{(j_k)} R_{(j_k)} \cos(j_1 \lambda_1 + j_2 \lambda_2 + j_3 \tilde{\omega}_1 + j_4 \tilde{\omega}_2 + j_5 \Omega_1 + j_6 \Omega_2), \quad (4.2)$$

where $R_{(j_k)}$ are the strengths of each term (depending on a , e , and i) and the coefficients j_k are integers that satisfy the d’Alembert conditions:

$$j_1 + j_2 + j_3 + j_4 + j_5 + j_6 = 0 \quad (4.3)$$

and

$$j_5 + j_6 = \text{even}. \quad (4.4)$$

Hamilton (1994) provides an explanation for the d'Alembert rules based on spatial symmetry. The argument of Eq. 4.2 (called the resonant argument or resonant angle) can be rewritten in the following form commonly used for mean-motion resonances:

$$\phi = (p + q)\lambda_2 - p\lambda_1 + j_3\tilde{\omega}_1 + j_4\tilde{\omega}_2 + j_5\Omega_1 + j_6\Omega_2, \quad (4.5)$$

where $-p = j_1$ and $p + q = j_2$. The sum $|j_3| + |j_4| + |j_5| + |j_6|$ gives the number of e and $\sin(i)$ terms that appear in the resonant strength $R_{(jk)}$ (from Eq. 4.2) and hence the order of the resonance. The angle ϕ librates through a small range of values when the bodies are close to or in resonance, and it circulates through 360° when they are far from resonance. If there is no precession of the pericenter or ascending node, the bodies' longitude of conjunction $(p + q)\lambda_2 - p\lambda_1$ remains constant and Eq. 4.5 can be differentiated to give

$$(p + q)n_2 - pn_1 = 0, \quad (4.6)$$

describing an exact mean-motion resonance.

Io and Europa are in a 2:1 mean motion resonance, as are Europa and Ganymede. For Io and Europa's resonance, the longitude of conjunction librates about Io's pericenter and Europa's apocenter, having resonant angles

$$2\lambda_2 - \lambda_1 - \tilde{\omega}_1 = 0^\circ \quad (4.7)$$

and

$$2\lambda_2 - \lambda_1 - \tilde{\omega}_2 = 180^\circ, \quad (4.8)$$

with subscripts 1 for Io, 2 for Europa, and 3 for Ganymede

Europa and Ganymede's conjunction librates about Europa's pericenter but involves neither the pericenter nor the apocenter of Ganymede. This means that

Ganymede can be at any radial location in its orbit during conjunction with Europa. These properties are described by the resonant arguments

$$2\lambda_3 - \lambda_2 - \tilde{\omega}_2 = 180^\circ \quad (4.9)$$

and

$$2\lambda_3 - \lambda_2 - \tilde{\omega}_3, \text{ which circulates through } 360^\circ. \quad (4.10)$$

Considering all three satellites together, we subtract Eqs. 4.9 and 4.8 to get:

$$\phi = \lambda_1 - 3\lambda_2 + 2\lambda_3 = 180^\circ, \quad (4.11)$$

and differentiating,

$$n_1 - 2n_2 = n_2 - 2n_3. \quad (4.12)$$

Equation 4.12 describes the special kind of mean-motion resonance called the Laplace resonance. It means that Ganymede circles Jupiter once for every two Europa orbits and four Io orbits. The resonance stipulates that there can never be a triple conjunction, and when any two satellites are in conjunction, the third is at least 60° away (Murray and Dermott 1999). The two sides of Eq. 4.12 are the mean conjunction drift rates for the two satellite pairs, which are presently about $0.7395^\circ/\text{day}$ (Greenberg 1982). These drift rates are much smaller than the mean motions (see Table 4.2) and the pairs are very close to exact 2:1 commensurability.

So we see that in reality, resonances are not at exact ratios of integers, because of precession. Planetary oblateness, resulting from the spin of non-rigid bodies, is one source of precession. Perturbations from oblateness are quantified by another disturbing function, involving coefficients J_k , where k is an integer. If there is north-south symmetry (which is the case for the giant planets), the odd terms are all zero.

As a result, the extent of a planet’s rotational deformation is commonly denoted by J_2 , the highest-order non-zero coefficient. Jupiter’s J_2 is 0.014736, much higher than that of the terrestrial planets and second only to Saturn in the Solar System. The gaseous planets are more oblate than the other planets because of their fast spins.

While oblateness does not change e or i , it does cause precessions of the pericenter and ascending node of an orbit. For all prograde satellites (including the Galilean moons), oblateness causes precession of the pericenter and regression of the ascending node; for retrograde satellites, both the pericenter and the ascending node precess. Precession from J_2 accounts for 97% of Io’s total precession and 80% of Europa’s, but it only accounts for $\sim 40\%$ of Callisto’s precession (Hamilton, 2005, personal communication). For Callisto, Ganymede and the Sun are also significant sources of orbital precession.

Orbital precession causes mean-motion resonances to split into multiple resonances involving inclination and eccentricity that occur at slightly separated locations. The two first-order resonances for the Io-Europa and Europa-Ganymede pairs are written in Eqs. 4.7, 4.8, 4.9, and 4.10. Labeling the resonant arguments ϕ_{1-6} in order of distance from the planet, the entire set of six first- (2:1) and second-order (4:2) resonances are:

$$\phi_1 = 4\lambda_2 - 2\lambda_1 - 2\Omega_1 \tag{4.13}$$

$$\phi_2 = 4\lambda_2 - 2\lambda_1 - \Omega_1 - \Omega_2 \tag{4.14}$$

$$\phi_3 = 4\lambda_2 - 2\lambda_1 - 2\Omega_2 \tag{4.15}$$

$$\phi_4 = 2\lambda_2 - \lambda_1 - \tilde{\omega}_1 \quad (4.16)$$

$$\phi_5 = 4\lambda_2 - 2\lambda_1 - \tilde{\omega}_1 - \tilde{\omega}_2 \quad (4.17)$$

$$\phi_6 = 2\lambda_2 - \lambda_1 - \tilde{\omega}_2. \quad (4.18)$$

The locations of the multiple resonances are all close to each other and may even overlap; they typically become more tightly spaced at greater distances from the planet. Zhang and Hamilton (2008) developed a resonant overlap criterion for the two first-order eccentricity resonances. These six first- and second-order terms are illustrated in Fig. 4.2. In Fig. 4.2, the resonances are labeled by the orbital elements affected by each resonance (with $\tilde{\omega}$ affecting e and Ω affecting i) instead of the entire resonant argument; we will continue to use this notation throughout this dissertation. For example, the resonance in Eq. 4.13 involves only Ω_1 and is second-order, so it is labeled i_1^2 .

Tides also have important effects on planet-satellite systems. As the force of gravity depends on distance, a satellite pulls strongest on the part of the planet closest to it, less strongly on the center of the planet, and least strongly on the side farthest away. This has the effect of raising two bulges on the planet, one on the area closest to the satellite and one on the far side. However, planets also spin, and tides take time to form, so the bulge is usually not perfectly in line with the satellite. In fact, the only case when the bulge aligns with the planet-satellite line is when the satellite orbits at exactly the same rate as the spin of the planet. This happens when the satellite orbits at the synchronous radius r_{syn} :

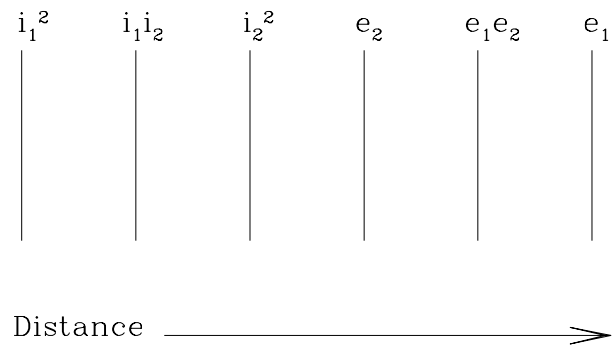


Figure 4.2 A schematic showing the six first- (2:1) and second-order (4:2) interior resonances, in order of their distance from the planet (with Jupiter to the left). Resonances are marked with the orbital elements they affect.

$$r_{syn} = \left(\frac{GM_P}{\Omega_P^2} \right)^{1/3}, \quad (4.19)$$

where Ω_P is the planet's spin rate. The Galilean satellites are all outside of $r_{syn} = 2.24 R_J$, and their orbital rates n (see Table 4.2) are much slower than Jupiter's spin rate, which is about $870^\circ/\text{day}$. Because of this, the bulge on Jupiter from any one of the satellites gets ahead of the planet-satellite line. This exerts a torque on the system. As a result, rotational energy from Jupiter's spin is transferred into orbital energy for the satellite, both slowing Jupiter's spin and increasing the sizes of the satellites' orbits. The satellites' outward migration is slow, however: only about $1\text{--}2 R_J$ over the age of the Solar System (Hamilton *et al.* 2001; Proctor *et al.* 2002). Planetary tides also generally increase satellite eccentricities (Jeffreys 1961).

Tides on the satellite from the planet work in the same way. They push in the opposite direction, opposing the semi-major axis increase from planetary tides. In addition, they have the effect of slowing the satellite's spin until the same face is locked toward the planet at all times. This happens very quickly; all of the Galilean satellites are currently spin-synchronized (Peale 1977). Satellite tides also circularize eccentric orbits very effectively. This can be understood because tides on the satellite are stronger at pericenter and weaker at apocenter. Since the tidal force is nearly radial, orbital angular momentum is conserved, but orbital energy decreases and eccentricity is forced to decrease as well. This effect usually dominates the increase in eccentricity from planetary tides (Goldreich 1963), and thus the overall result is eccentricity damping. The orbits of the Galilean satellites are not completely circular (see Table 4.2), however, because of their resonant interactions.

Tides also damp inclinations, but this happens much more slowly, at nearly the satellite tidal migration rate (Kaula 1964). Over the age of the Solar System, this corresponds to a damping of less than a tenth of current tilts, for most satellites

(Zhang 2007). As there are usually no other effective ways of damping inclination, and we can assume that satellite formation in a protoplanetary disk produces zero initial tilts, any current inclinations must be a result of orbital interactions. We apply this assumption in our numerical study described in Section 5.3.

Tidal flexing and the Laplace resonance have rather impressive effects on the Galilean system: powering Io's volcanoes (Peale *et al.* 1979), maintaining a layer of liquid water under Europa's surface (Cassen *et al.* 1980, 1979), and possibly resurfacing Ganymede (Malhotra 1991; Showman and Malhotra 1997). Understanding the origin and history of this resonance is of great interest, but it is a complex problem. In the next chapter, we study a piece of the larger picture: entrance into the Io-Europa resonance. In Section 5.1, we describe various evolution models for the Galilean satellites. In Sections 5.2 and 5.3, we detail our numerical study, and in Section 5.4, we discuss our overall conclusions and give some future directions.

Chapter 5

Resonant History of the Galilean Satellites

5.1 Orbital evolution models

There are two predominant models for explaining the origin of the Laplace resonance. The first is resonant capture caused by orbital expansion from tides raised in Jupiter, especially by Io. As we have discussed in the previous chapter, planetary tides cause the orbits of satellites to grow with time. Goldreich (1965) suggested that resonances may have developed because of tidal expansion, and several groups have investigated this mechanism as the origin of the Galilean satellites' Laplace resonance (e.g., Greenberg 1981b; Malhotra 1991; Showman and Malhotra 1997; Showman *et al.* 1997; Yoder 1979; Yoder and Peale 1981). Since tides are strongest close to the planet, Io's orbit expands fastest and locks with Europa into the 2:1 resonance. The orbits of the pair continue to expand outward until Europa captures Ganymede into their 2:1 resonance. It is also possible that Europa and Ganymede formed sufficiently close to each other that their resonance was entered first, with Io joining

later.

Greenberg (1982, 1987) proposed that the three satellites may have originated in resonance at formation (here we define formation to mean the time at which the circumplanetary gas disk has dissipated and satellite accretion has ended). He suggested that the satellites formed in deeper resonance than at present (i.e., with lower conjunction drift rates (Eq. 4.12)), and that they have been subsequently moving out of resonance.

A problem with Greenberg's theory was that the lack of a sufficient mechanism other than chance to place the satellites in resonance upon formation. In 2002, Canup and Ward detailed a model for formation of the Galilean satellites in a low-density gas disk and noted that the satellites likely migrated inward during the formation period. If this occurred, Ganymede's high mass means that it would have migrated faster than the other satellites. Peale and Lee (2002) and Peale and Lee (2003) proposed that Ganymede could have captured Europa into resonance during this inward motion, followed by Europa's inward migration to meet Io. Variations of this model have also been proposed (e.g., Peale and Lee 2003). For example, it is possible that Io's inward motion was fast enough to avoid resonance with Europa during formation, while post-formation tidal expansion joined Io with Europa and Ganymede at a later time.

Differentiating between these scenarios (i.e., resonant lock due to tidal expansion or formation in resonance) would allow us to constrain the satellites' formation distances and better understand the processes that have shaped the Galilean satellites into their current states. In this chapter, we study the tidal expansion origin theory and focus on Io's resonance with Europa.

5.2 Numerical model

We studied this problem with simulations using the symplectic integrator of *HNBody* (Rauch and Hamilton 2002), the *N*-body package also used in other chapters of this thesis. Our simulations include Jupiter, the Sun, and Io and Europa. The Sun is not very important for the orbits of Io and Europa, but it must be included when Ganymede is added to the system, as will eventually be necessary for a full investigation. We were careful to set the stepsize of the integrator to resolve at least 20 steps per orbit of Io. We also included Jupiter’s J_2 , J_4 , and J_6 oblateness terms.

In addition, we use *HNDrag* to simulate planetary and satellite tides with artificial drag forces. We first modeled only planetary tides (the tides raised in the planet by the satellite) with a simple force in the direction of the satellite’s velocity ($\mathbf{F} \propto v\hat{\mathbf{v}}$). The planetary tidal force causes the semi-major axis of the satellite’s orbit to expand.

Over the age of the Solar System, Io has migrated outward by at most 1–2 R_J (Hamilton *et al.* 2001; Proctor *et al.* 2002, constrained by considering Io’s effect on the inclinations of small, inner Jovian satellites). This rate, $2\text{--}4 \times 10^{-10} R_J/\text{yr}$, is very slow and computationally expensive to simulate directly. To circumvent this problem, we take two approaches: 1) simulate only the time interval in which the resonance is important, and/or 2) speed up the drag rate by one or two orders of magnitude. A faster drag rate is valid as long as the orbital expansion is slow enough that the resonance of interest is traversed in the adiabatic limit.

HNBody can give output either in Cartesian positions and velocities or in osculating orbital elements, which are calculated as if there are no perturbations. Since the perturbations from oblateness and the satellites themselves are large, osculating orbital elements are not a good representation of the actual orbits. Instead, follow-

ing Greenberg (1981a), we output positions and velocities and then convert these to geometric orbital elements, which describe the physical shape of the orbit. To do this, we use the conversion program *cj2*, which corrects for the effects of the planet’s J_2 value.

5.3 Simulations of Io and Europa

The goal of this work is to understand the Galilean system’s past evolution, using their current orbits as constraints. Recall (Section 4.2) that tidal damping of orbital inclinations happens very slowly and is almost negligible over the lifetime of the Solar System. In addition, we expect that formation in the protoplanetary gas disk left the satellites with very flat, zero-inclination orbits. Because of these two factors, we can use the satellites’ current inclinations as constraints for their past histories. From Table 4.2, we see that Europa’s inclination is almost a half degree, Ganymede and Callisto have tilts of a few tenths of a degree, and Io’s inclination is only a few hundredths of a degree. In order for an orbital evolution scenario to be valid, we begin by assuming that none of the satellites’ inclinations can rise higher than their current values. (We revise this assumption slightly later in this section.) In addition, of course, the true scenarios must produce the current tilts, with Europa’s relatively large value being especially diagnostic.

Io and Europa’s resonance involves libration of the angles associated with eccentricity: ϕ_4 , ϕ_5 , and ϕ_6 (Eqs. 4.16- 4.18). From Fig. 4.2, we see that the eccentricity resonances are located further from the planet than the pair’s second-order inclination resonances. If Io evolved outward to capture Europa into the e -resonances, the satellites must have encountered the 4:2 inclination resonances before reaching the eccentricity resonances. In addition, Io must pass these resonances without acquir-

ing a large orbital tilt. This requirement has proven to be the central challenge of our work.

Before discussing the results of our simulations, we give an example plot of orbital elements and discuss some common features seen during resonant crossing. For bodies with converging orbits, as we simulate, resonant capture can occur; Fig. 5.1 shows trapping into the i_2^2 resonance. When captured, the affected element rises with a square-root-shaped curve (Hamilton and Burns 1993). In Fig. 5.1, i_2 rises from 0° to $\sim 0.56^\circ$ by the end of the simulation.

Note, though, that i_1 also rises along a similar square-root curve, but only to a much smaller value ($\sim 0.009^\circ$). This type of feature, ubiquitous in our simulations, is not indicative of capture into a resonance involving i_1 . Instead, it is a secular effect due to the slowly changing Laplace plane. A body's Laplace plane is defined as the plane in which its node precesses and its inclination remains constant. Close to the planet, the Laplace plane coincides with the planet's equatorial plane, while near a massive satellite, the Laplace plane is the satellite's orbital plane. Zhang and Hamilton (2007) calculate the instantaneous tilt of the Laplace plane for small satellites at Neptune perturbed by Triton.

At the beginning of this simulation (Fig. 5.1), Io's Laplace plane is close to the Jupiter's equatorial plane. As Europa's inclination rises, Io's Laplace plane tilts slightly in response. This is Io's forced inclination. Io's free inclination is actually still 0° if measured from the Laplace plane. Since the plotted inclinations are measured from the equatorial plane, we are seeing the changing tilt of the Laplace plane. In other simulations, the same type of response appears in i_2 for capture into the i_1^2 resonance. We can easily distinguish this response feature from the dual-inclination $i_1 i_2$ resonance because the bodies' inclinations rise by comparable amounts when captured into the $i_1 i_2$ resonance.

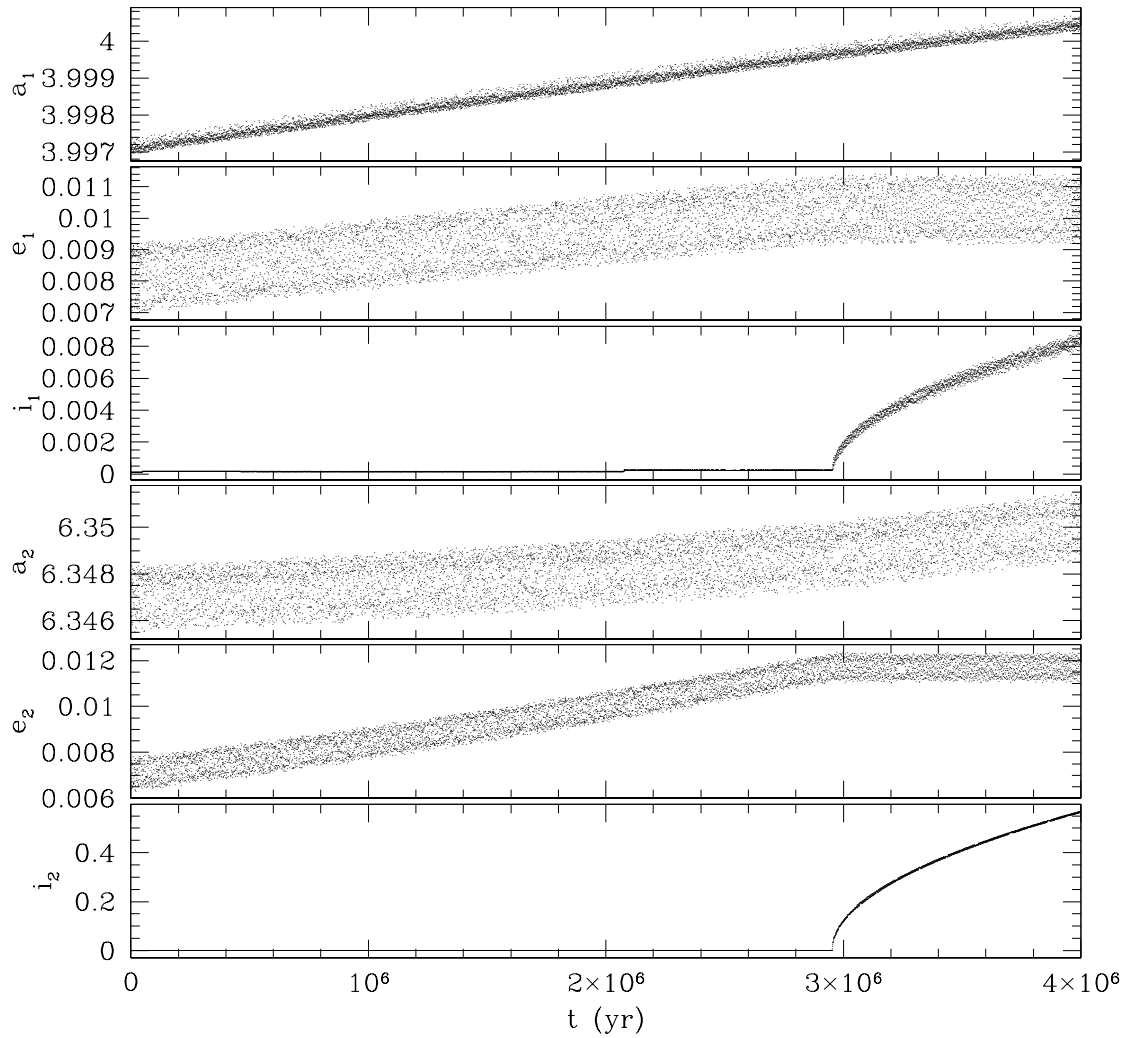


Figure 5.1 Capture into the i_2^2 resonance, with a weak response visible in i_1 . This simulation was run with a drag rate of $10^{-9} R_J/\text{yr}$ and both inclinations initially set to 0° .

Another feature to notice in Fig. 5.1 is a rise in the bodies' eccentricity that halts when the inclination capture occurs. Though the inclination resonances occur first, the eccentricity resonances are much stronger, and thus eccentricity is forced to even larger values as the bodies approach the more-distant e -resonances. However, the eccentricity rise is halted when the satellites capture into i_2^2 because the e -resonance is no longer being approached.

Finally, note the large-amplitude oscillations in the semi-major axes and eccentricities in Fig. 5.1. The reason for these oscillations is the mutual perturbations between the satellites. Recall that we print out positions and velocities and use the program *cj2* to convert the data files to orbital elements. This technique allows for inclusion of the planet's J_2 oblateness parameter, giving more accurate orbital elements than by simply using the osculating elements. We also input the planet's mass to *cj2*, in the form of GM_P . However, it is more complicated to take into account perturbations from the satellite masses. The conversion from *cj2* neglects the masses of the satellites, and thus the orbital elements are fuzzy as a result. The fuzziness is due to the differences between true geometric orbital elements and the approximate elements that we use. Inclinations are less affected because the perturbations between satellites are primarily in-plane. The strong resonant features are still discernible even with the orbital element oscillations, but weaker features may require modeling of the mutual satellite perturbations to obtain more-sharply defined elements.

We now discuss the results of our suite of integrations. In our initial simulations, we started Io and Europa on orbits with $i \approx 0^\circ$, setting Io's initial $a \approx 4R_J$ and placing Europa so that the bodies would cross their 2:1 resonance within several million years. We simulated only Io's semi-major axis growth with planetary tides ($\mathbf{F} \propto \mathbf{v}\hat{\mathbf{v}}$) and included no satellite tides. We found that for reasonable drag rates,

Io and Europa inevitably captured into one or more of their second-order inclination resonances. This was true for all drag rates slower than about $10^{-7} R_J/\text{yr}$, which is ~ 200 times faster than the nominal rate. In addition, we found that in these simulations, capture into the any one of the inclination resonances caused the satellites' tilts to rise higher than their current values. Figure 5.2 shows an example of one such case.

If Io's orbit expanded to capture Europa in this way, some other mechanism either a) altered their orbits, allowing them to pass by the inclination resonances without being trapped, or b) broke them out of inclination resonance before their tilts rose to values higher than at present. We now consider the first option.

One possible means of altering orbits is by encounters with prior resonances. Prior to the troublesome second-order inclination resonances, Io would have encountered a suite of weaker third-order resonances. The 2:1 third-order resonances labeled in Fig. 5.3 appear just before the 4:2 inclination resonances and, as can be seen in the figure, do impart kicks to the bodies' inclinations. However, for initial $i_1 \approx 0$, $i_2 \approx 0$ these resonances do not trap Io and Europa, for all of our tested migration rates. The imparted kicks are too small to prevent Io and Europa from capturing into the 4:2 inclination resonances.

While kicks from these earlier third-order resonances are small, they do indicate the possibility that Io and Europa had non-zero inclinations prior to encountering the 4:2 resonance. Accordingly, we tested to see if still-larger initial inclinations would have been enough to prevent trapping into the 4:2 inclination resonances. To do this, we tilted Io and Europa by various amounts not exceeding their current values, integrated them through the second-order inclination resonances, and noted the outcome. Table 5.1 gives the results of 20 such simulations. Each was integrated with a planetary tidal drag rate of $10^{-9} R_J/\text{yr}$, only a few times faster than the actual

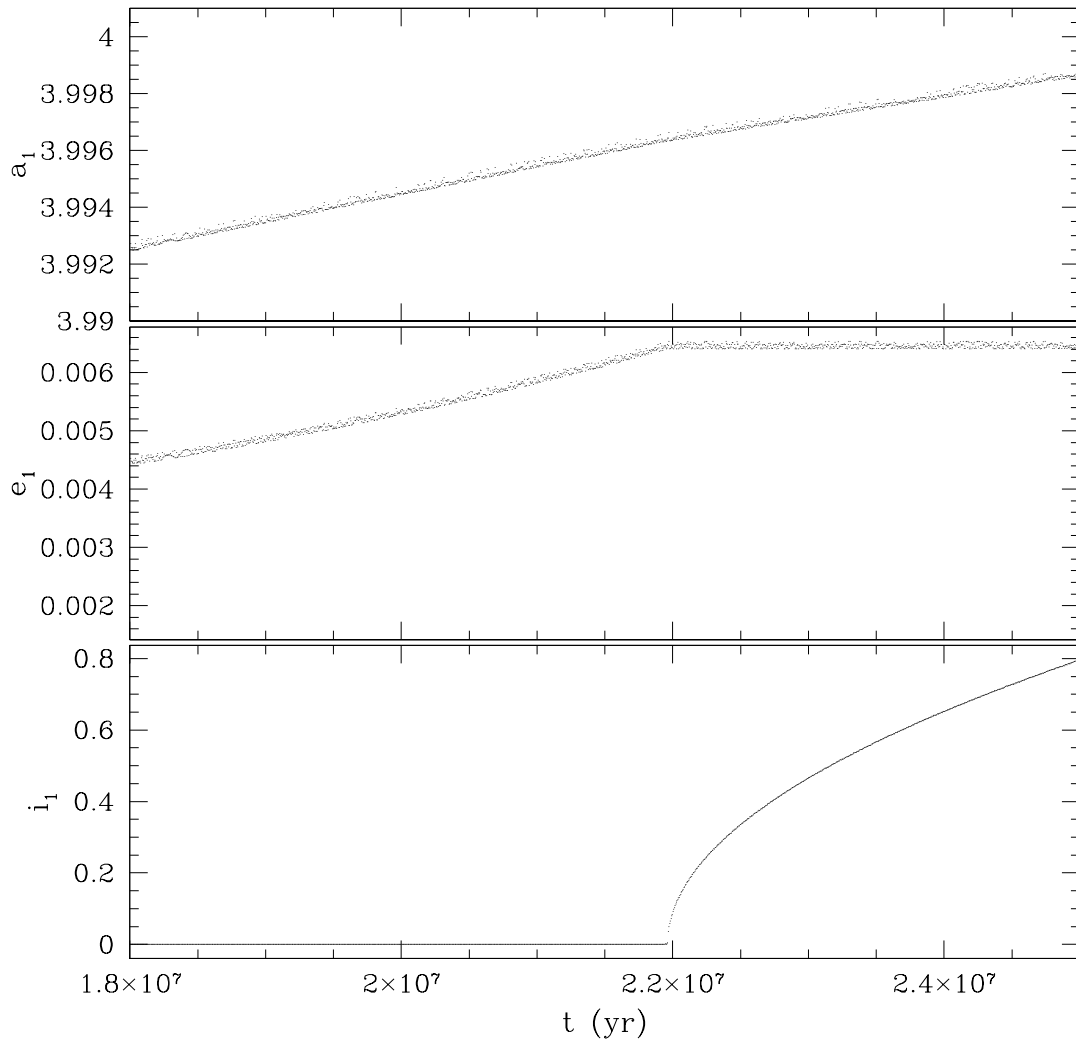


Figure 5.2 Io's semi-major axis, eccentricity, and inclination as it captures into the i_1^2 resonance with Europa just before $t = 2.2 \times 10^7$ yr (with a drag rate of $10^{-9} R_J/\text{yr}$). Io's current inclination is only a few hundredths of a degree, so this evolution could not have happened.

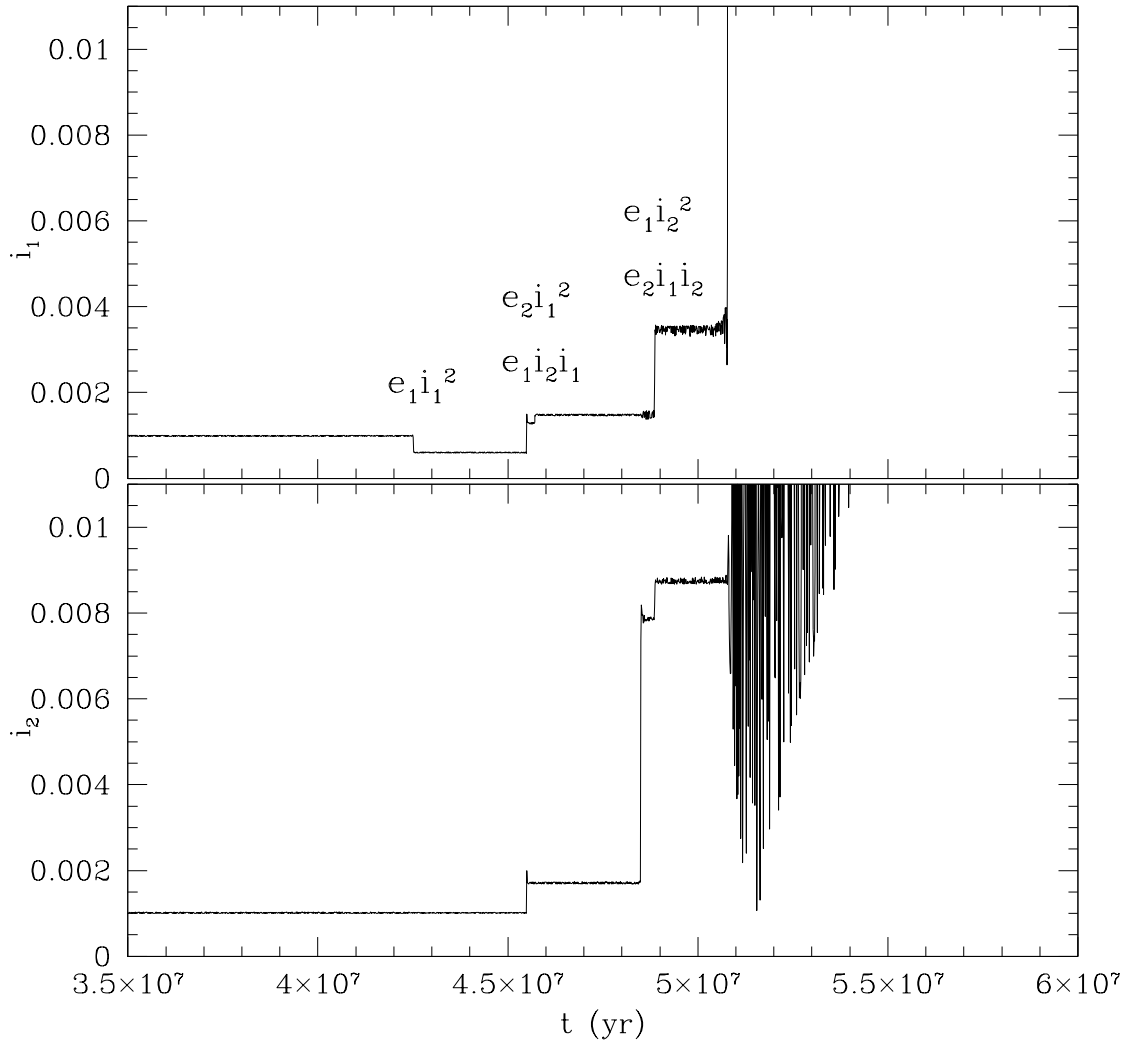


Figure 5.3 Inclination kicks to Io's inclination (i_1) and Europa's inclination (i_2) from third-order 2:1 resonances prior to the second-order 4:2 inclination resonances, with a drag rate of $10^{-9} R_J/\text{yr}$. At $t \approx 5.1 \times 10^7$ yr, both bodies' inclinations rise to large values as they capture into the i_1^2 resonance.

Table 5.1. Integrations of Io and Europa’s 2:1 resonance passage: non-zero initial inclinations

	$i_1 = 0^\circ$	$i_1 = 0.01^\circ$	$i_1 = 0.03^\circ$	$i_1 = 0.05^\circ$
$i_2 = 0^\circ$	i_2^2	$i_1 i_2$	$i_1 i_2$	i_1^2 , then $i_1 i_2$
$i_2 = 0.02^\circ$	$i_1 i_2$	i_2^2	$i_1 i_2$	$i_1 i_2$
$i_2 = 0.05^\circ$	$i_1 i_2$	$i_1 i_2$	$i_1 i_2$	$i_1 i_2$
$i_2 = 0.10^\circ$	$i_1 i_2$	i_1^2 , then $i_1 i_2$	i_1^2 , then $i_1 i_2$	$e_2 i_1 i_2$, then $i_1 i_2$
$i_2 = 0.20^\circ$	$e_2 i_1 i_2$, then $i_1 i_2$	$e_2 i_1 i_2$, then $i_1 i_2$	$i_1 i_2$	i_1^2 , then $i_1 i_2$

Note. — Capture into Io and Europa’s 4:2 i_1^2 , $i_1 i_2$, and i_2^2 resonances. Some captures into the 2:1 $e_2 i_1 i_2$ resonance are also seen, all of which have the resonant argument given in Eq. 5.1. The satellites’ initial inclinations are given in the top row (Io) and left column (Europa). Entries of more than one resonance (e.g., “ i_1^2 , then $i_1 i_2$,” mean that the satellites capture into the first resonance, break out, and then capture into the second resonance. The boldfaced simulation is shown in Fig. 5.4.

rate. In all of the simulations, the satellites still captured into inclination resonances, raising their tilts beyond their current values.

One interesting feature in these simulations is the reappearance of the third-order 2:1 resonances discussed above. Figure 5.4 shows an example of capture into the $e_2 i_1 i_2$ resonance, with resonant argument

$$\phi = 2\lambda_2 - \lambda_1 - \tilde{\omega}_2 - \Omega_1 + \Omega_2. \quad (5.1)$$

Recalling the d’Alembert rules: 1) all coefficients of the resonant argument must add to zero and 2) nodal terms must appear in pairs, it is easy to see that all third-order 2:1 resonances must include one positive precession term. While the more-typical negative coefficients in resonant arguments lead to increases in the corresponding elements, positive coefficients in a resonant argument correspond to decreases in the corresponding elements (Zhang and Hamilton 2008). For zero inclinations, trapping into the above third-order 2:1 resonances cannot occur, as inclination cannot be decreased below 0° . However, in simulations with non-zero initial inclinations, Io

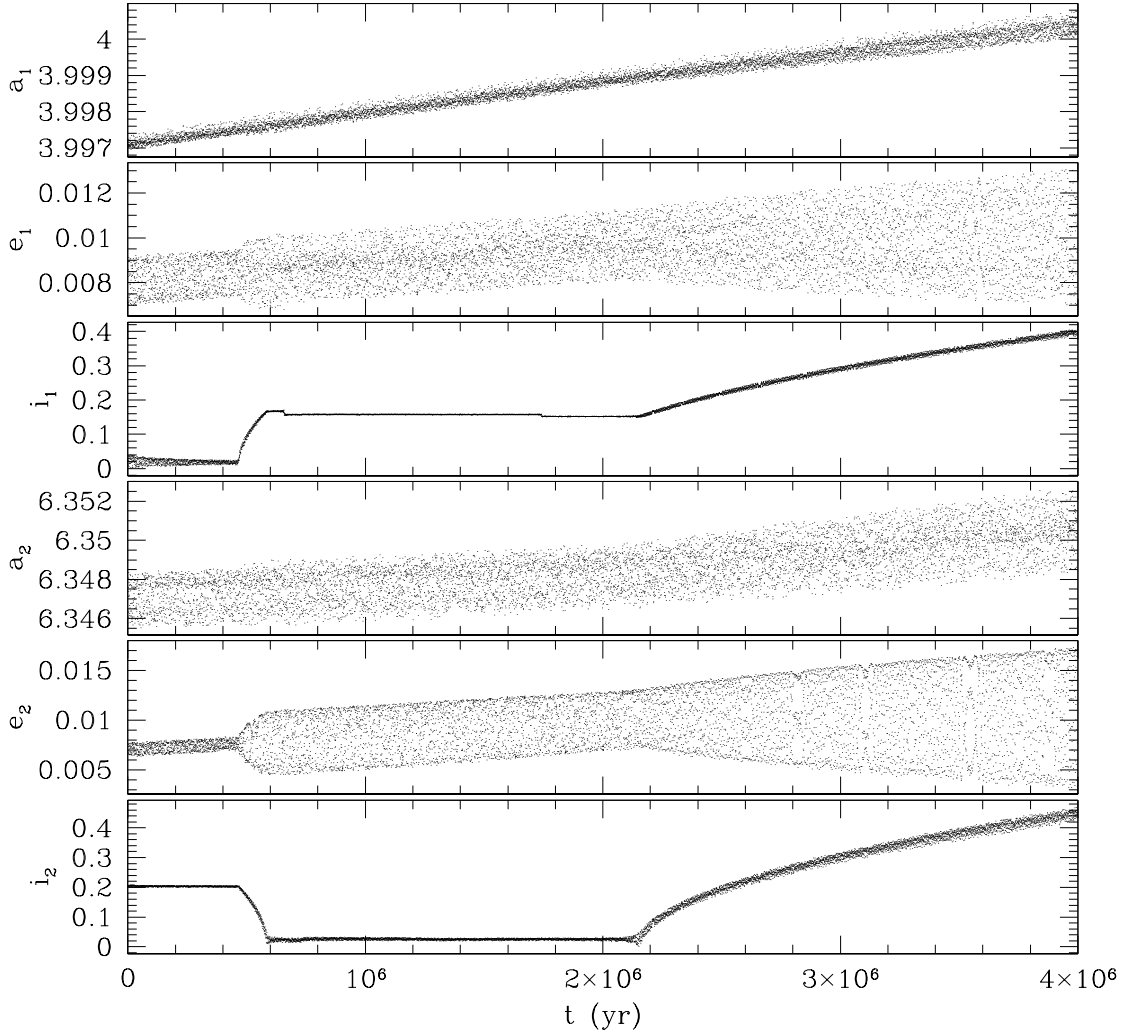


Figure 5.4 Capture into the third-order $e_2 i_2 i_1$ resonance (at $\sim 5 \times 10^5$ yr) with resonant argument given by Eq. 5.1 followed by capture into the $i_1 i_2$ resonance (at $\sim 2.2 \times 10^6$ yr). This simulation was run with a drag rate of $10^{-9} R_J/\text{yr}$, with Io and Europa's initial inclinations set to 0° and 0.20° , respectively. Europa loses its initially small inclination, while Io's orbit becomes tilted. Although harder to see, Europa's eccentricity also grows due to the $e_2 i_2 i_1$ resonance: the thickening of the e_2 trace at $\sim 5 \times 10^5$ yr is due to the increase of free eccentricity superimposed on the slowly-rising forced eccentricity from the nearby e_2 resonance.

and Europa can temporarily trap into these resonances, as seen in Fig. 5.4. In this figure, capture into the $e_2 i_1 i_2$ resonance increases i_1 by roughly the same amount by which i_2 is decreased. As i_2 approaches 0° , the bodies exit the third-order resonance, later capturing into the $i_1 i_2$ resonance. In our simulations, temporary capture into these third-order 2:1 resonances was always followed by permanent capture into one of the second-order 4:2 inclination resonances.

Note that these third-order resonances offer a means of decreasing inclination, something we previously assumed was unlikely. More accurately, the 2:1 third-order resonances can decrease one inclination, but only if another inclination increases, unlike their second-order counterparts. It is possible that Io and Europa exchanged tilts through a third-order 2:1 resonance, but this would leave the origin of Io's initially-high tilt unexplained. Nevertheless, this broadens the types of scenarios that should be considered.

There appear to be several patterns in the suite of simulations starting with non-zero inclinations (Table 5.1). First, temporary capture into a third-order resonance occurs only for sufficiently large initial inclinations of Europa ($\geq 0.10^\circ$). This is reasonable, as the strength of the resonance increases for larger i_2 , and the inclination must be non-zero in order to decrease when captured. Second, capture into $i_1 i_2$ happens more frequently than capture into any other resonance. This is partially because the $i_1 i_2$ resonance is twice as strong as the other second-order inclination resonances. Third, captures into i_1^2 and i_2^2 do happen, but they are infrequent and there does not appear to be a clear pattern establishing when they occur. Fourth, all captures into i_1^2 break out and subsequently trap into $i_1 i_2$. Overall, the $i_1 i_2$ resonance wins out over the other resonances in nearly all cases.

While we see many complicated features in simulations with non-zero inclinations, all of the simulations still resulted in final inclinations greater than the satel-

lites' current values. Thus non-zero initial inclinations cannot, by themselves, explain Io and Europa's evolution into eccentricity resonances. There appears to be no way to get past the inclination resonances and to the eccentricity resonances beyond.

The simulations above neglect the effects of tides on the satellite, which damp the satellites' eccentricities. We now discuss several simulations testing the effects of satellite tides ($\mathbf{F} \propto M_s r_s^{-6} v_r \hat{\mathbf{r}}$) as well as a more-realistic planetary tidal force ($\mathbf{F} \propto M_s r_s^{-6} \hat{\mathbf{v}}$), where M_s is the satellite's mass, r_s is its distance from the planet, and v_r is its radial speed. The r^{-6} dependence means that these forces are strongest near the planet and drop off quickly with distance. We try various strengths for both forces, which depend on the bodies' unknown tidal dissipation quality factors Q . While the planetary tidal force causes expansion of the orbital semi-major axes, the satellite tidal force both damps eccentricity and opposes the semi-major axis expansion. These effects can be seen with the following equations describing the evolution of semi-major axis and eccentricity under the influence of the 2:1 resonance and tidal forces (adapted from Hamilton and Burns (1993)):

$$\frac{da}{dt} = aen\beta \sin \phi + C_{PT}an + 2C_{ST}ae^2n \quad (5.2)$$

and

$$\frac{de}{dt} = -n\beta \sin \phi + C_{ST}en, \quad (5.3)$$

where β is the dimensionless, positive strength of the resonance, ϕ is the resonant argument, and C_{PT} and C_{ST} are the strengths of the planetary and satellite tidal forces, respectively, with C_{PT} positive outside the synchronous radius R_{syn} (and negative inside R_{syn}) and C_{ST} always negative. Both C_{PT} and C_{ST} are dimensionless functions of a , but we treat them as constants here because we are interested only

in evolution through a small range of a . Note that for zero eccentricity, da/dt for satellite tides goes to zero. This is because the satellites are spin-locked to Jupiter. The tidal bulges on the satellites are aligned with the planet and have no side-to-side motion. If the satellites orbited on circles, then, there would be no source of energy dissipation from satellite tides and no corresponding change in a . The real satellites' non-zero eccentricities, however, do impart a negative da/dt .

In our simulations, the tidal drag rates are input to *HNDrag* as the magnitude of their contribution to da/dt and hence are equal to $C_{PT}an$ for planetary tides and $2C_{ST}ae^2n$ for satellite tides (from Eq. 5.2). We see that the semi-major axis evolution can be determined by the struggle between planetary tides moving the orbits out and satellite tides pushing them in toward the planet. This competition between planetary and satellite tides leads to important effects. Figure 5.5 shows a simulation with planetary tides ($C_{PT}an = 10^{-8} R_J/\text{yr}$) applied to Io and no satellite tides. We see that Io and Europa capture into the i_1^2 resonance, and i_1 rises to 4° by the end of the simulation. Unlike the simulations discussed in Table 5.1, the satellites do not break out of i_1^2 . This may be because here they start with zero tilts, and the strengths of the inclination resonances increase with increasing inclinations. Note the appearance of the common features we discussed earlier in this section: the Laplace plane inclination response in i_2 , the halted eccentricity rise for both bodies, and small oscillations in eccentricity.

Compare Fig. 5.5 with Fig. 5.6, which shows the same simulation except for the addition of satellite tides applied to Io, here integrated with $2C_{ST}ae^2n = -1.5 \times 10^{-11} R_J/\text{yr}$. The results are similar, also showing capture into the i_1^2 resonance. We see that e_1 becomes less fuzzy, as satellite tides damp its oscillations in the first million years. However, the presence of satellite tides also opposes the semi-major axis expansion, and the satellites have slightly smaller a values at the end of the

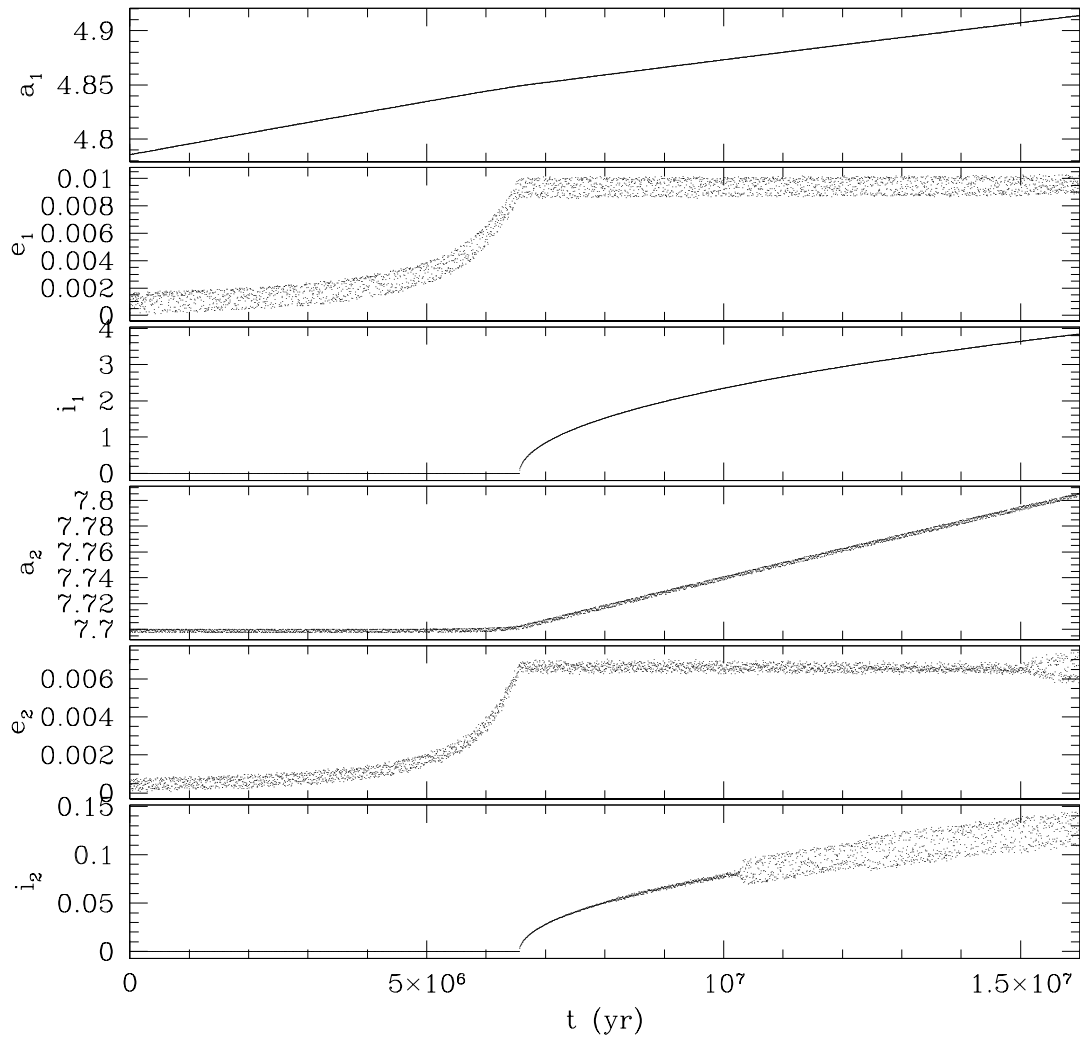


Figure 5.5 Orbital elements of Io and Europa integrated with planetary tides at $C_{PTan} = 10^{-8} R_J/\text{yr}$ and no satellite tides. The bodies capture into the i_1^2 resonance, with thickenings in the e_2 and i_2 traces corresponding to non-zero values of Europa's free eccentricity and free inclination.

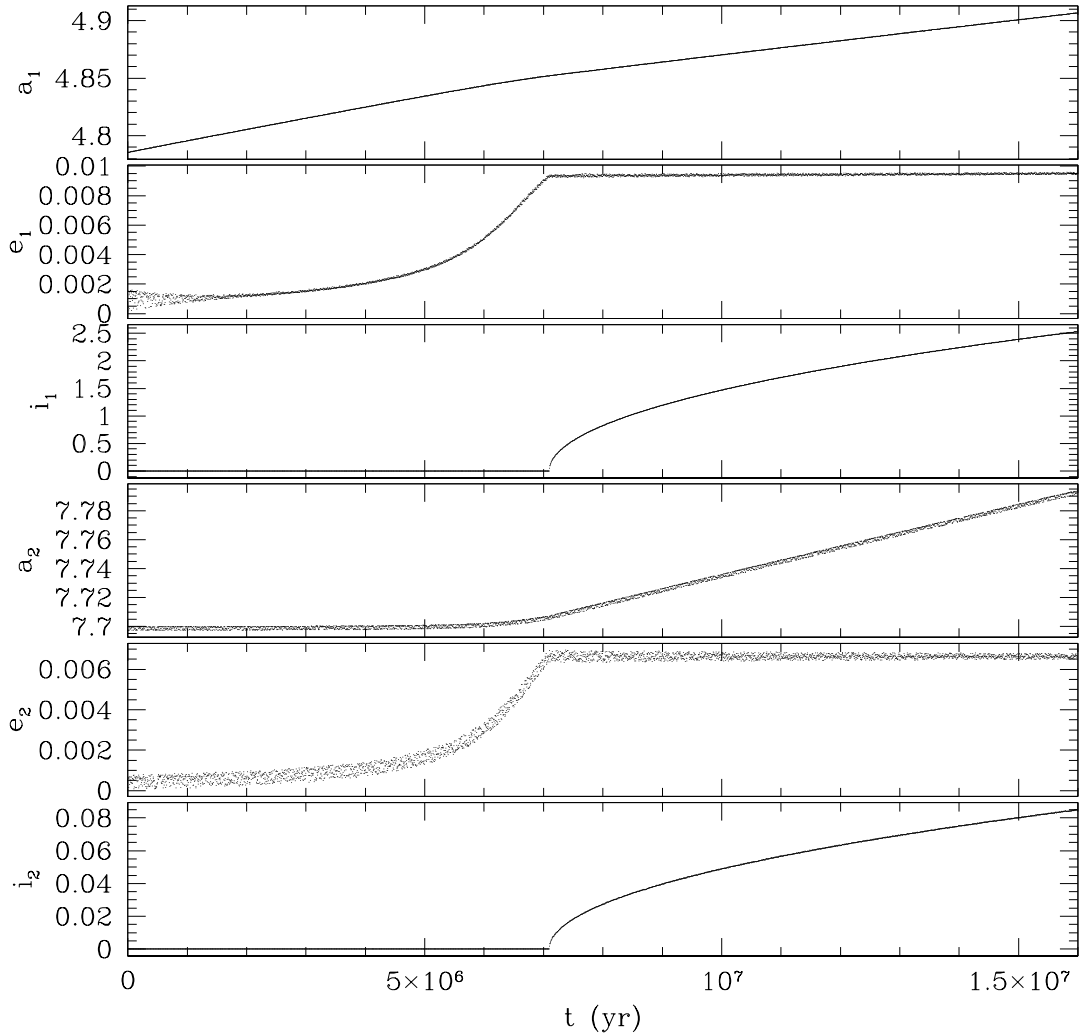


Figure 5.6 The same as Fig. 5.5 (planetary tides at $C_{PTan} = 10^{-8} R_J/\text{yr}$) with the addition of satellite tides at $2C_{ST}ae^2n = -1.5 \times 10^{-11} R_J/\text{yr}$.

simulation. In addition, in Fig. 5.6, i_1 captures slightly later in time (at $t = 7 \times 10^6$ yr instead of 6.5×10^6 yr) and grows less, to only 2.5° . The smaller final i_1 in Fig. 5.6 is not simply due to delayed capture; without satellite tides (Fig. 5.5), i_1 grows to 2.5° long before the end of the simulation, by $t = 10^7$ yr. We see that in this simulation (Fig. 5.6), satellite tides delay resonant capture and lead to reduced inclination growth, because the satellites are converging less rapidly.

Figure 5.7 shows another similar integration, here with satellite tides on Io at $2C_{ST}ae^2n = -1.5 \times 10^{-10} R_J/\text{yr}$, 10 times stronger than in Fig. 5.6. The evolution changes dramatically with stronger satellite tides. Both bodies' eccentricities still rise as they approach the eccentricity resonances (and e_1 's small oscillations damp even faster than in Fig. 5.6), but they are halted at smaller values than in the previous simulations. Here the eccentricities cease growing not because of resonant capture (as in Figs. 5.5 and 5.6) but because of eccentricity damping due to the satellite tides. The eccentricity at which Io tops off is entirely determined by the ratio of the strengths of the planetary and satellite tidal forces (e.g., lower final e for stronger satellite tides), and Europa's final e follows as a natural result. Most importantly, however, while the semi-major axes are moving out together, there is no resonant capture. The satellite tides are strong enough to have damped the resonant angles of both bodies to equilibrium points (ϕ_4 (Eq. 4.16) librates around 0° and ϕ_6 (Eq. 4.18) around 180° , as seen in Fig. 5.8) before the bodies reached the inclination resonance. We confirm this conclusion by examining the ratio of mean motions: in Figs. 5.5 and 5.6, capture into the i_1^2 resonance happens at $n_1/n_2 = 2.0015$, while here (Figure 5.7), the satellites reach equilibrium earlier and at a greater separation, with $n_1/n_2 = 2.0073$. In addition, other simulations show that capture into e_2 occurs at still later $n_1/n_2 = 1.9992$.

What, then, is the ratio of mean motions for Io and Europa today? From Table 4.2, we see that it is precisely 2.0073. This means that Io and Europa's actual state matches well with the integration shown in Fig. 5.7, and the satellites never captured into resonance. To accurately describe their current state, we must carefully define what we mean by "resonance" and by "capture." Here we consider resonance to mean having one or more resonant angles (e.g., Eqs. 4.13- 4.18) librating about an equilibrium value. With that definition, Io and Europa are in resonance.

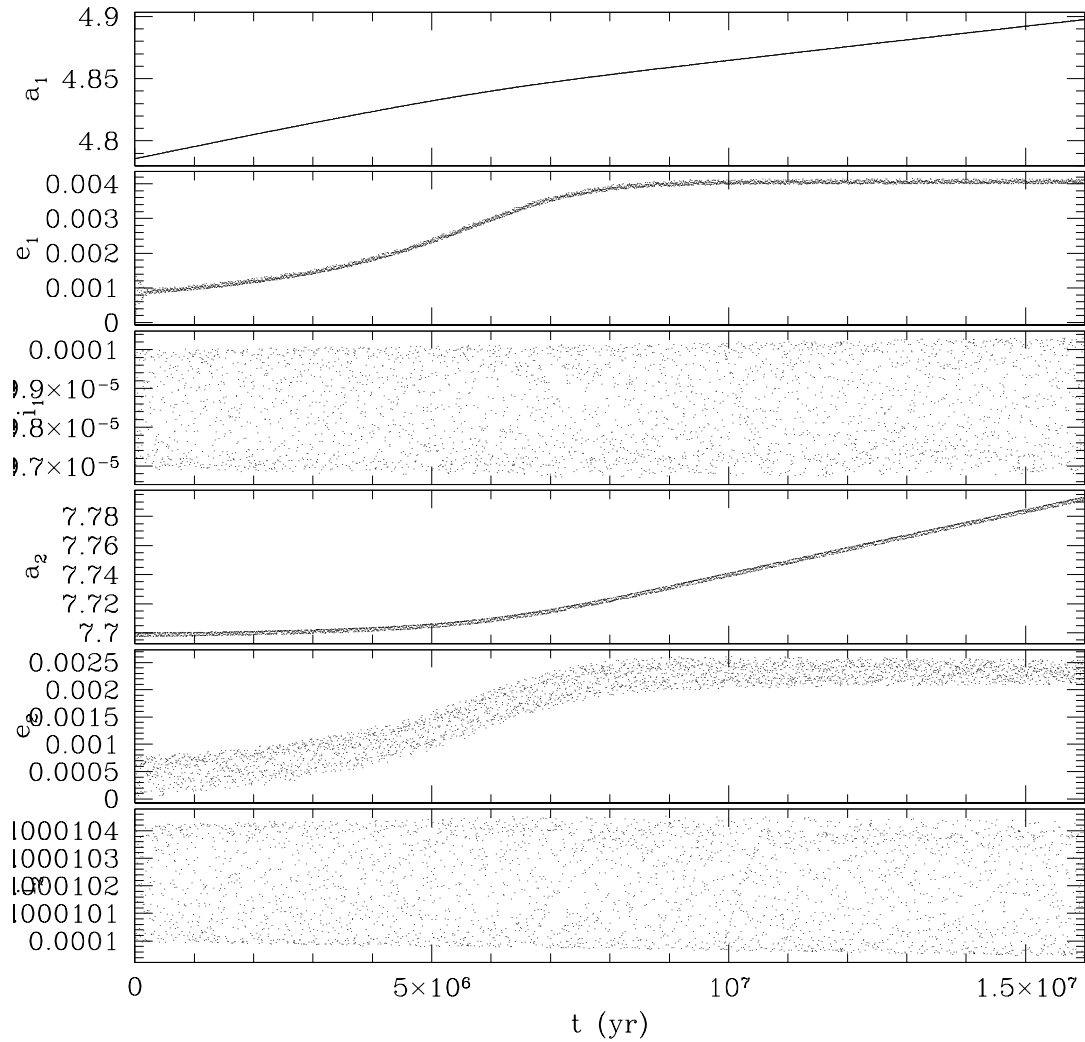


Figure 5.7 The same as Fig. 5.6 (planetary tides at $C_{PT}an = 10^{-8} R_J/\text{yr}$) except with a $10\times$ stronger satellite tides, at $2C_{STA}e^2n = -1.5 \times 10^{-10} R_J/\text{yr}$. The mean-motion ratio n_1/n_2 at which the bodies reach equilibrium is 2.0073, equal to Io and Europa's current n -ratio.

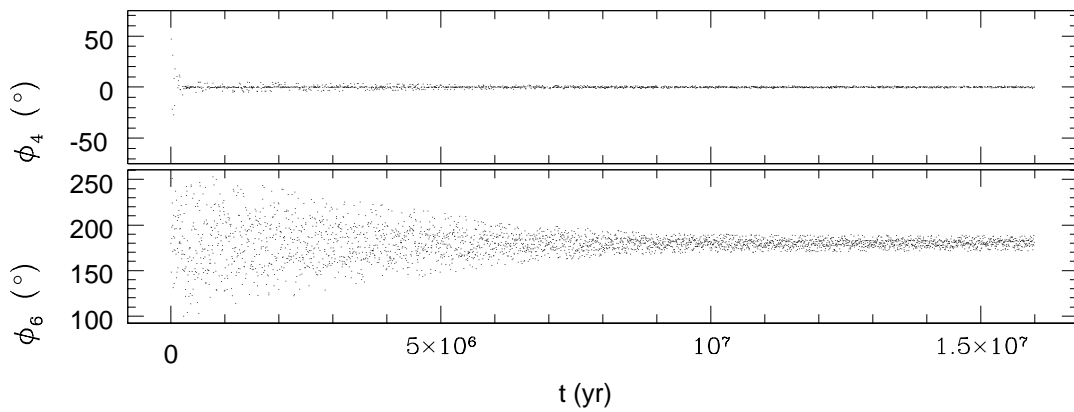


Figure 5.8 Resonant angles ϕ_4 and ϕ_6 (Eqs. 4.16, 4.18), for the evolution in Fig. 5.7. Tides quickly damp ϕ_4 to a very small libration amplitude, corresponding to the fast damping of Io's free eccentricity seen in Fig. 5.7. As satellite tides are not applied directly to Europa, ϕ_6 , which involves Europa's eccentricity, does not decrease quickly.

However, there are two types of resonant libration, bounded by a critical orbit called the separatrix; crossing the separatrix is what is normally defined as resonant capture. It is possible, though, to have not crossed the separatrix and still librate—this is what Io and Europa are doing. Their proximity to the separatrix causes their eccentricities to be forced above zero, but satellite tides cause a strong-enough back reaction (Eq. 5.2) that the orbits cease converging. This halts the evolution at a tidally determined equilibrium, and no resonant capture occurs.

So, the solution to the problem of bypassing inclination resonances to capture into eccentricity resonances is that the satellites have not captured into resonance after all. Tides on the satellites have damped their resonant angles so efficiently that they librate stably without the satellites ever having crossed the separatrix into resonant capture. This result is not clearly stated in the literature, possibly because others have not considered the inclination resonances in tandem with the eccentricity resonances.

We find, also, that the ratio of the strengths of planetary and satellite tides in this simulation leads to a final e_1 of 0.004, matching Io’s current value while simultaneously matching n_1/n_2 . This suggests that Io’s eccentricity was determined by interactions primarily with Europa without strong contribution from Ganymede, which is a reasonable conclusion. The final e_2 in this simulation is 0.0025, smaller than Europa’s current eccentricity of 0.0094, but interactions with Ganymede still need to be considered, and the Europa-Ganymede resonance probably accounts for the major portion of Europa’s e .

Finally, we still do not have an explanation for the satellites’ inclinations. However, Io’s inclination is small, and Europa’s larger tilt may have originated in its resonance with Ganymede, which also has a significantly non-zero inclination.

5.4 Findings and future directions

In our simulations of Io and Europa, we have found that for 0° initial inclinations and realistic planetary tidal drag rates (but neglecting satellite tides), the satellites inevitably capture into the 4:2 inclination resonances and their inclinations rise above their current values.

We examined several possible ways to avoid the inclination resonances. First, we determined that kicks imparted by earlier third-order 2:1 resonances to zero-inclination orbits are too weak to significantly alter the orbits.

Secondly, we found that when Io and Europa's initial inclinations are higher than zero, the bodies can capture into the third-order 2:1 resonances, resulting in an inclination increase for one body with a corresponding decrease for the other body. Regardless, all simulations with non-zero initial inclinations resulted in eventual capture into one of the 4:2 inclination resonances and final tilts higher than at present.

Finally, we investigated the effects of satellite tides, exploring their suppression of resonant capture. We found that strong satellite tides can cause the satellites' resonant angles to damp onto stable equilibria prior to encountering the 2:1 suite of resonances. For Io and Europa, this occurs when the moons reach a mean-motion ratio $n_1/n_2 = 2.0073$, equal to that measured today. Thus Io and Europa never captured into the 2:1 resonances and their resonant angles librate because of damping from satellite tides. This result also naturally accounts for Io's current eccentricity.

Simulating all three satellites is a natural extension of this project. We believe interactions with Ganymede almost certainly played a major role in determining the final state of the system.

Chapter 6

Conclusions

Our work was aimed at investigating two main questions: 1) how were the giant planets' irregular satellites captured? and 2) how did the Galilean satellites evolve into the Laplace resonance?

6.1 Irregular satellites

In Chapter 2, we developed and evaluated a new mechanism for capturing the irregular satellites. In the model, binary asteroids are tidally disrupted during close approaches with a planet, resulting in a speed change that leaves one of the pair bound as a satellite. This kind of capture produces highly extended and inclined orbits that require dissipation to resemble current orbits. Because of this, our model stipulates that capture must occur when circumplanetary gas is still present in the system. However, as tidal disruption provides the energy loss for capture, only tenuous gas is needed for orbital evolution.

In testing our satellite capture model, we found that capture depends heavily on the binary's mass, separation, and the simulated starting distance from the planet. We compared capture of binaries to long-lived temporary capture of single bodies

and found that for $C_J < 3.015$ (corresponding to approach speeds of $v_{L_1} \sim 2.01$ km/s), binaries capture with similar rates as single objects. For higher C_J (lower v_{L_1}), though, the effects of binaries are easily seen, as the capture efficiency of binaries rises to about an order of magnitude higher than that of singles. In addition, we developed a procedure to scale our equal-mass binary results to binaries with unequal masses. Finally, we discussed the problem of survivability for these captures and suggested solutions including 1) capture of binaries with larger-than-optimal separations that lead to orbits fully outside Callisto's and 2) evolution of the capture orbits by the surrounding gas disk.

In Chapter 3, we examined possible sources for binary capture, focusing on Trojan asteroids and asteroids from the outer main belt. To assess each population, we simulated the asteroids leaking out of their orbits and calculated the bodies' Jacobi constants at each approach within Jupiter's Hill sphere. We found that all Trojan asteroids flew by the planet with fast speeds, corresponding to effectively-zero binary capture probabilities. Asteroids near the outer edge of the main belt (especially those interior to Jupiter's 4:3 resonance), on the other hand, had Jacobi constants close to those with maximum capture probabilities. This result applied equally for bodies that escaped on initially unstable orbits or those escaping because of Jupiter's inward migration. From this study, we conclude that the outer asteroid belt is a promising source of irregular satellites captured from binaries. In the future, we hope to assess the capture probability of Kuiper belt objects in a similar way.

6.2 Galilean satellites

In Chapter 5, we studied the origin of Io and Europa's resonance and showed that their evolution ceased prior to encountering the separatrix for capture into the 2:1 resonances. Instead, their resonant arguments librate solely because the satellites' free eccentricities have been damped below their forced eccentricities. In leading to this conclusion, we modeled capture into resonance by simulating tidal expansion pushing Io out to meet Europa. We found that the satellites' second-order inclination resonances acted as gatekeepers for the first-order eccentricity resonances. In our simulations, the inclination resonances inevitably raised the satellites' tilts to values well-above those they have today. We examined several possible routes past these troublesome inclination resonances and found that none of them were viable.

However, when including satellite tides, which oppose the bodies' semi-major expansion and suppress their eccentricities, we saw that the resonant angles ϕ_4 and ϕ_6 damped to equilibria before the 2:1 resonances were encountered. We found that Io and Europa are currently in this configuration, having never captured into the 2:1 eccentricity resonances. In addition, the satellites never reached the 4:2 inclination resonances and experienced no inclination excitation from them. This conclusion accounts for the origin of Io's eccentricity. Finally, it is likely that interactions with Ganymede led to the moons' current inclinations, and future work will elucidate its role in establishing the Laplace resonance.

Bibliography

- Agnor, C., and D. P. Hamilton 2006a. Satellite capture via binary-planet gravitational encounters. *BAAS* **38**, 674.
- Agnor, C. B., and D. P. Hamilton 2006b. Neptune's capture of its moon Triton in a binary-planet gravitational encounter. *Nature* **441**, 192–194.
- Astakhov, S. A., A. D. Burbanks, S. Wiggins, and D. Farrelly 2003. Chaos-assisted capture of irregular moons. *Nature* **423**, 264–267.
- Astakhov, S. A., and D. Farrelly 2004. Capture and escape in the elliptic restricted three-body problem. *MNRAS* **354**, 971–979.
- Barr, A. C., and R. M. Canup 2010. Origin of the Ganymede-Callisto dichotomy by impacts during the late heavy bombardment. *Nature Geoscience* **3**, 164–167.
- Bate, M. R., S. H. Lubow, G. I. Ogilvie, and K. A. Miller 2003. Three-dimensional calculations of high- and low-mass planets embedded in protoplanetary discs. *MNRAS* **341**, 213–229.
- Beatty, J. K., C. Collins Petersen, and A. Chaikin 1999. *The New Solar System*. Sky Publishing Corporation.
- Beaugé, C., and D. Nesvorný 2007. Proper elements and secular resonances for irregular satellites. *AJ* **133**, 2537–2558.
- Brož, M., and D. Vokrouhlický 2008. Asteroid families in the first-order resonances with Jupiter. *MNRAS* **390**, 715–732.

- Burns, J. A. 1986a. Some background about satellites. In M. S. Burns, J. A. & Matthews (Ed.), *Satellites*, pp. 1–38. Univ. of Arizona Press.
- Burns, J. A. 1986b. The evolution of satellite orbits. In M. S. Burns, J. A. & Matthews (Ed.), *Satellites*, pp. 117–158. Univ. of Arizona Press.
- Canup, R. M., and W. R. Ward 2002. Formation of the Galilean satellites: Conditions of accretion. *AJ* **124**, 3404–3423.
- Cassen, P., S. J. Peale, and R. T. Reynolds 1980. Tidal dissipation in Europa - A correction. *Geophys. Res. Lett.* **7**, 987–988.
- Cassen, P., R. T. Reynolds, and S. J. Peale 1979. Is there liquid water on Europa. *Geophys. Res. Lett.* **6**, 731–734.
- Cieza, L., D. L. Padgett, K. R. Stapelfeldt, J. Augereau, P. Harvey, N. J. Evans, II, B. Merín, D. Koerner, A. Sargent, E. F. van Dishoeck, L. Allen, G. Blake, T. Brooke, N. Chapman, T. Huard, S. Lai, L. Mundy, P. C. Myers, W. Spiesman, and Z. Wahhaj 2007. The Spitzer c2d survey of weak-line T Tauri stars. II. New constraints on the timescale for planet building. *ApJ* **667**, 308–328.
- Colombo, G., and F. A. Franklin 1971. On the formation of the outer satellite groups of Jupiter. *Icarus* **15**, 186–189.
- Cruikshank, D. P. 1977. Radii and albedos of four Trojan asteroids and Jovian satellites 6 and 7. *Icarus* **30**, 224–230.
- Ćuk, M. 2005. *Dynamics and origin of the irregular satellites of the giant planets*. Ph. D. thesis, Cornell University, Ithaca, NY.
- Ćuk, M., and J. A. Burns 2004a. Gas-drag-assisted capture of Himalia’s family. *Icarus* **167**, 369–381.
- Ćuk, M., and J. A. Burns 2004b. On the secular behavior of irregular satellites. *AJ* **128**, 2518–2541.
- Ćuk, M., J. A. Burns, V. Carruba, P. D. Nicholson, and R. A. Jacobson 2002. New

- secular resonances involving the irregular satellites of Saturn. In *BAAS*, Volume 34, pp. 943.
- Cuzzi, J. N., R. C. Hogan, and K. Shariff 2008. Toward planetesimals: Dense chondrule clumps in the protoplanetary nebula. *ApJ* **687**, 1432–1447.
- D’Angelo, G., T. Henning, and W. Kley 2003. Thermohydrodynamics of circumstellar disks with high-mass planets. *ApJ* **599**, 548–576.
- de Pater, I., and J. J. Lissauer 2001. *Planetary Sciences*. Cambridge University Press.
- Degewij, J., B. Zellner, and L. E. Andersson 1980. Photometric properties of outer planetary satellites. *Icarus* **44**, 520–540.
- Fernández, Y. R., S. S. Sheppard, and D. C. Jewitt 2003. The albedo distribution of Jovian Trojan asteroids. *AJ* **126**, 1563–1574.
- Fornasier, S., E. Dotto, F. Marzari, M. A. Barucci, H. Boehnhardt, O. Hainaut, and C. de Bergh 2004. Visible spectroscopic and photometric survey of L5 Trojans: investigation of dynamical families. *Icarus* **172**, 221–232.
- Gaspar, H. S., O. C. Winter, and E. Vieira Neto 2010. Irregular satellites of Jupiter: Capture configurations of binary-asteroids. *arXiv:1002.2392v1*.
- Gladman, B., J. Kavelaars, M. Holman, J. Petit, H. Scholl, P. Nicholson, and J. A. Burns 2000. NOTE: The discovery of Uranus XIX, XX, and XXI. *Icarus* **147**, 320–324.
- Gladman, B., J. J. Kavelaars, M. Holman, P. D. Nicholson, J. A. Burns, C. W. Hergenrother, J. Petit, B. G. Marsden, R. Jacobson, W. Gray, and T. Grav 2001. Discovery of 12 satellites of Saturn exhibiting orbital clustering. *Nature* **412**, 163–166.
- Gladman, B. J., P. D. Nicholson, J. A. Burns, J. Kavelaars, B. G. Marsden, G. V. Williams, and W. B. Offutt 1998. Discovery of two distant irregular moons of

- Uranus. *Nature* **392**, 897–899.
- Goldreich, P. 1963. On the eccentricity of satellite orbits in the Solar System. *MNRAS* **126**, 257–268.
- Goldreich, P. 1965. An explanation of the frequent occurrence of commensurable mean motions in the solar system. *MNRAS* **130**, 159.
- Grav, T., and J. Bauer 2007. A deeper look at the colors of the Saturnian irregular satellites. *Icarus* **191**, 267–285.
- Grav, T., M. J. Holman, and W. C. Fraser 2004. Photometry of irregular satellites of Uranus and Neptune. *ApJ* **613**, L77–L80.
- Grav, T., M. J. Holman, B. J. Gladman, and K. Aksnes 2003. Photometric survey of the irregular satellites. *Icarus* **166**, 33–45.
- Greenberg, R. 1981a. Apsidal precession of orbits about an oblate planet. *AJ* **86**, 912–914.
- Greenberg, R. 1981b. Tidal evolution of the Galilean satellites - A linearized theory. *Icarus* **46**, 415–423.
- Greenberg, R. 1982. Orbital evolution of the Galilean satellites. In D. Morrison (Ed.), *Satellites of Jupiter*, pp. 65–92.
- Greenberg, R. 1987. Galilean satellites - Evolutionary paths in deep resonance. *Icarus* **70**, 334–347.
- Greenberg, R., P. Geissler, G. Hoppa, and B. R. Tufts 2002. Tidal-tectonic processes and their implications for the character of Europa’s icy crust. *Reviews of Geophysics* **40**.
- Hamilton, D. P. 1994. A comparison of Lorentz, planetary gravitational, and satellite gravitational resonances. *Icarus* **109**, 221–240.
- Hamilton, D. P., and J. A. Burns 1991. Orbital stability zones about asteroids. *Icarus* **92**, 118–131.

- Hamilton, D. P., and J. A. Burns 1993. Lorentz and gravitational resonances on circumplanetary particles. *Advances in Space Research* **13**, 241–248.
- Hamilton, D. P., and A. V. Krivov 1997. Dynamics of distant moons of asteroids. *Icarus* **128**, 241–249.
- Hamilton, D. P., A. L. Proctor, and K. P. Rauch 2001. An explanation for the high inclinations of Thebe and Amalthea. *BAAS* **33**, 1085.
- Hénon, M. 1969. Numerical exploration of the restricted problem, V. *A&A* **1**, 223–238.
- Heppenheimer, T. A., and C. Porco 1977. New contributions to the problem of capture. *Icarus* **30**, 385–401.
- Holman, M. J., J. J. Kavelaars, T. Grav, B. J. Gladman, W. C. Fraser, D. Milisavljevic, P. D. Nicholson, J. A. Burns, V. Carruba, J. Petit, P. Rousselot, O. Mousis, B. G. Marsden, and R. A. Jacobson 2004. Discovery of five irregular moons of Neptune. *Nature* **430**, 865–867.
- Jeffreys, H. 1961. The effect of tidal friction on eccentricity and inclination. *MNRAS* **122**, 339–343.
- Jewitt, D. 2005. A first look at the Damocloids. *AJ* **129**, 530–538.
- Jewitt, D., and N. Haghighipour 2007. Irregular satellites of the planets: Products of capture in the early Solar System. *ARA&A* **45**, 261–295.
- Jewitt, D., and S. Sheppard 2005. Irregular satellites in the context of planet formation. *Space Science Reviews* **116**, 441–455.
- Jewitt, D. C. 2002. From Kuiper belt object to cometary nucleus: The missing ultrared matter. *AJ* **123**, 1039–1049.
- Johansen, A., J. S. Oishi, M. Low, H. Klahr, T. Henning, and A. Youdin 2007. Rapid planetesimal formation in turbulent circumstellar disks. *Nature* **448**, 1022–1025.
- Johnson, T. V. 1999. Io. In Beatty, J. K., Collins Petersen, C., & Chaikin, A. (Ed.),

- The New Solar System*. Sky Publishing Corporation.
- Johnson, T. V. 2004. A look at the Galilean satellites after the Galileo mission. *Physics Today* **57**(4), 77–83.
- Kaula, W. M. 1964. Tidal dissipation by solid friction and the resulting orbital evolution. *Reviews of Geophysics and Space Physics* **2**, 661–685.
- Kavelaars, J. J., M. J. Holman, T. Grav, D. Milisavljevic, W. Fraser, B. J. Gladman, J. Petit, P. Rousselot, O. Mousis, and P. D. Nicholson 2004. The discovery of faint irregular satellites of Uranus. *Icarus* **169**, 474–481.
- Levison, H. F., E. M. Shoemaker, and C. S. Shoemaker 1997. Dynamical evolution of Jupiter’s Trojan asteroids. *Nature* **385**, 42–44.
- Lubow, S. H., M. Seibert, and P. Artymowicz 1999. Disk accretion onto high-mass planets. *ApJ* **526**, 1001–1012.
- Luu, J. 1991. CCD photometry and spectroscopy of the outer Jovian satellites. *AJ* **102**, 1213–1225.
- Malhotra, R. 1991. Tidal origin of the Laplace resonance and the resurfacing of Ganymede. *Icarus* **94**, 399–412.
- Mann, R. K., D. Jewitt, and P. Lacerda 2007. Fraction of contact binary Trojan asteroids. *AJ* **134**, 1133–1144.
- Marchis, F., P. Descamps, J. Berthier, D. Hestroffer, I. de Pater, A. Conrad, D. Le Mignant, F. Chaffee, and D. Gavel 2003. Searching and studying binary asteroids with AO systems. *BAAS* **35**, 959.
- Marchis, F., M. H. Wong, J. Berthier, P. Descamps, D. Hestroffer, F. Vachier, D. Le Mignant, and I. de Pater 2006. S/2006 (624) 1. *IAU Circ.* **8732**, 1.
- Maris, M., G. Carraro, G. Cremonese, and M. Fulle 2001. Multicolor photometry of the Uranus irregular satellites Sycorax and Caliban. *AJ* **121**, 2800–2803.
- Marzari, F., and H. Scholl 2002. On the instability of Jupiter’s Trojans. *Icarus* **159**,

328–338.

- Merline, W. J., L. M. Close, N. Siegler, D. Potter, C. R. Chapman, C. Dumas, F. Menard, D. C. Slater, A. C. Baker, M. G. Edmunds, G. Mathlin, O. Guyon, and K. Roth 2001. S/2001 (617) 1. *IAU Circ.* **7741**, 2.
- Merline, W. J., P. M. Tamblyn, C. Dumas, L. M. Close, C. R. Chapman, D. D. Durda, H. F. Levison, D. P. Hamilton, D. Nesvorný, A. Storrs, B. Enke, and F. Menard 2007. The search for Trojan binaries. *BAAS* **38**, 538.
- Milani, A. 1993. The Trojan asteroid belt: Proper elements, stability, chaos and families. *Celest. Mech.* **57**, 59–94.
- Morbidelli, A., W. F. Bottke, D. Nesvorný, and H. F. Levison 2009. Asteroids were born big. *Icarus* **204**, 558–573.
- Mosqueira, I., and P. R. Estrada 2003. Formation of the regular satellites of giant planets in an extended gaseous nebula I: Subnebula model and accretion of satellites. *Icarus* **163**, 198–231.
- Murray, C. D., and S. F. Dermott 1999. *Solar System Dynamics*. Cambridge University Press.
- Nesvorný, D. 2008. Formation of Kuiper belt binaries. *BAAS* **40**, 464.
- Nesvorný, D., J. L. A. Alvarelos, L. Dones, and H. F. Levison 2003. Orbital and collisional evolution of the irregular satellites. *AJ* **126**, 398–429.
- Nesvorný, D., D. Vokrouhlický, and A. Morbidelli 2007. Capture of irregular satellites during planetary encounters. *AJ* **133**, 1962–1976.
- Nicholson, P. D., M. Čuk, S. S. Sheppard, D. Nesvorný, and T. V. Johnson 2008. Irregular Satellites of the Giant Planets. In Barucci, M. A., Boehnhardt, H., Cruikshank, D. P., & Morbidelli, A. (Ed.), *The Solar System Beyond Neptune*, pp. 411–424. Univ. of Arizona Press.
- Noll, K. S., W. M. Grundy, D. C. Stephens, H. F. Levison, and S. D. Kern 2008.

- Evidence for two populations of classical transneptunian objects: The strong inclination dependence of classical binaries. *Icarus* **194**, 758–768.
- Papaloizou, J. C. B., R. P. Nelson, W. Kley, F. S. Masset, and P. Artymowicz 2007. Disk-planet interactions during planet formation. *Protostars and Planets V*, 655–668.
- Pappalardo, R. T., M. J. S. Belton, H. H. Breneman, M. H. Carr, C. R. Chapman, G. C. Collins, T. Denk, S. Fagents, P. E. Geissler, B. Giese, R. Greeley, R. Greenberg, J. W. Head, P. Helfenstein, G. Hoppa, S. D. Kadel, K. P. Klaasen, J. E. Klemaszewski, K. Magee, A. S. McEwen, J. M. Moore, W. B. Moore, G. Neukum, C. B. Phillips, L. M. Prockter, G. Schubert, D. A. Senske, R. J. Sullivan, B. R. Tufts, E. P. Turtle, R. Wagner, and K. K. Williams 1999. Does Europa have a subsurface ocean? Evaluation of the geological evidence. *J. Geophys. Res.* **104**, 24015–24056.
- Peale, S. J. 1977. *Rotation histories of the natural satellites*, pp. 87–111.
- Peale, S. J., P. Cassen, and R. T. Reynolds 1979. Melting of Io by tidal dissipation. *Science* **203**, 892–894.
- Peale, S. J., and M. H. Lee 2002. A primordial origin of the Laplace relation among the Galilean satellites. *Science* **298**, 593–597.
- Peale, S. J., and M. H. Lee 2003. On the origin of the Laplace relation among the Galilean satellites. *BAAS* **35**, 1047.
- Pollack, J. B., J. A. Burns, and M. E. Tauber 1979. Gas drag in primordial circumplanetary envelopes - A mechanism for satellite capture. *Icarus* **37**, 587–611.
- Pollack, J. B., O. Hubickyj, P. Bodenheimer, J. J. Lissauer, M. Podolak, and Y. Greenzweig 1996. Formation of the giant planets by concurrent accretion of solids and gas. *Icarus* **124**, 62–85.
- Proctor, A., D. Hamilton, and K. Rauch 2002. An explanation for the high inclina-

- tions of Amalthea and Thebe. *APS Meeting Abstracts*, 17077.
- Rauch, K. P., and D. P. Hamilton 2002. The HNBody package for symplectic integration of nearly-Keplerian systems. *BAAS* **34**, 938.
- Rettig, T. W., K. Walsh, and G. Consolmagno 2001. Implied evolutionary differences of the Jovian irregular satellites from a BVR color survey. *Icarus* **154**, 313–320.
- Saha, P., and S. Tremaine 1993. The orbits of the retrograde Jovian satellites. *Icarus* **106**, 549–562.
- Scotti, J. V., T. B. Spahr, R. S. McMillan, J. A. Larsen, J. Montani, A. E. Gleason, T. Gehrels, B. G. Marsden, and G. V. Williams 2000. S/1999 J 1. *IAU Circ.* **7460**, 1.
- Sheppard, S. S., D. Jewitt, and J. Kleyna 2005. An ultradeep survey for irregular satellites of Uranus: Limits to completeness. *AJ* **129**, 518–525.
- Sheppard, S. S., D. Jewitt, and J. Kleyna 2006. A survey for “normal” irregular satellites around Neptune: Limits to completeness. *AJ* **132**, 171–176.
- Sheppard, S. S., and D. C. Jewitt 2003. An abundant population of small irregular satellites around Jupiter. *Nature* **423**, 261–263.
- Sheppard, S. S., D. C. Jewitt, J. Kleyna, and B. G. Marsden 2007. S/2007 S 1, S/2007 S 2, and S/2007 S 3. *IAU Circ.* **8836**, 1.
- Sheppard, S. S., and C. A. Trujillo 2006. A thick cloud of Neptune Trojans and their colors. *Science* **313**, 511–514.
- Showman, A. P., and R. Malhotra 1997. Tidal evolution into the Laplace resonance and the resurfacing of Ganymede. *Icarus* **127**, 93–111.
- Showman, A. P., D. J. Stevenson, and R. Malhotra 1997. Coupled orbital and thermal evolution of Ganymede. *Icarus* **129**, 367–383.
- Silverstone, M. D., M. R. Meyer, E. E. Mamajek, D. C. Hines, L. A. Hillenbrand, J. Najita, I. Pascucci, J. Bouwman, J. S. Kim, J. M. Carpenter, J. R. Stauffer,

- D. E. Backman, A. Moro-Martin, T. Henning, S. Wolf, T. Y. Brooke, and D. L. Padgett 2006. Formation and Evolution of Planetary Systems (FEPS): Primordial warm dust evolution from 3 to 30 Myr around Sun-like stars. *ApJ* **639**, 1138–1146.
- Skrutskie, M. F., D. Dutkevitch, S. E. Strom, S. Edwards, K. M. Strom, and M. A. Shure 1990. A sensitive 10-micron search for emission arising from circumstellar dust associated with solar-type pre-main-sequence stars. *AJ* **99**, 1187–1195.
- Tegler, S. C., and W. Romanishin 2000. Extremely red Kuiper-belt objects in near-circular orbits beyond 40 AU. *Nature* **407**, 979–981.
- Tholen, D. J., and B. Zellner 1984. Multicolor photometry of outer Jovian satellites. *Icarus* **58**, 246–253.
- Trujillo, C. A., and M. E. Brown 2002. A correlation between inclination and color in the classical Kuiper belt. *ApJ* **566**, L125–L128.
- Tsiganis, K., R. Gomes, A. Morbidelli, and H. F. Levison 2005. Origin of the orbital architecture of the giant planets of the Solar System. *Nature* **435**, 459–461.
- Vieira Neto, E., O. C. Winter, and T. Yokoyama 2004. The effect of Jupiter’s mass growth on satellite capture. Retrograde case. *A&A* **414**, 727–734.
- Vokrouhlický, D., D. Nesvorný, and H. F. Levison 2008. Irregular satellite capture by exchange reactions. *AJ* **136**, 1463–1476.
- Weidenschilling, S. J. 1977. The distribution of mass in the planetary system and solar nebula. *Ap&SS* **51**, 153–158.
- Wetherill, G. W. 1989. Origin of the asteroid belt. In R. P. Binzel, T. Gehrels, & M. S. Matthews (Ed.), *Asteroids II*, pp. 661–680.
- Whipple, A. L., and P. J. Shelus 1993. A secular resonance between Jupiter and its eighth satellite? *Icarus* **101**, 265–271.
- Yoder, C. F. 1979. How tidal heating in Io drives the Galilean orbital resonance locks. *Nature* **279**, 767–770.

- Yoder, C. F., and S. J. Peale 1981. The tides of Io. *Icarus* **47**, 1–35.
- Yoshida, F., and T. Nakamura 2005. Size distribution of faint Jovian L4 Trojan asteroids. *AJ* **130**, 2900–2911.
- Zhang, K. 2007. *Resonant and secular orbital interactions*. Ph. D. thesis, University of Maryland, College Park, MD.
- Zhang, K., and D. P. Hamilton 2007. Orbital resonances in the inner neptunian system. I. The 2:1 Proteus Larissa mean-motion resonance. *Icarus* **188**, 386–399.
- Zhang, K., and D. P. Hamilton 2008. Orbital resonances in the inner neptunian system. II. Resonant history of Proteus, Larissa, Galatea, and Despina. *Icarus* **193**, 267–282.